TURBULENCE MODELING FOR COMPRESSIBLE SHEAR FLOWS

A Dissertation

by

CARLOS ARTURO GOMEZ ELIZONDO

Submitted to the Office of Graduate Studies of
Texas A&M University
in partial fulfillment of the requirements for the degree of

DOCTOR OF PHILOSOPHY

Approved by:

Co-Chairs of Committee,	Andrew Duggleby
	Sharath Girimaji
Committee Members,	Kalyan Annamalai
	Je-Chin Han
Department Head,	Jerald Caton

December 2012

Major Subject: Mechanical Engineering

ABSTRACT

Compressibility profoundly affects many aspects of turbulence in high-speed flows – most notably stability characteristics, anisotropy, kinetic-potential energy interchange and spectral cascade rate. Many of the features observed in compressible flows are due to the changing nature of pressure. Whereas for incompressible flows pressure merely serves to enforce incompressibility, in compressible flows pressure becomes a thermodynamic variable that introduces a strong coupling between energy, state, and momentum equations. Closure models that attempt to address compressibility effects must begin their development from sound first-principles related to the changing nature of pressure as a flow goes from incompressible to compressible regime. In this thesis, a unified framework is developed for modeling pressure-related compressibility effects by characterizing the role and action of pressure at different speed regimes. Rapid distortion theory is used to examine the physical connection between the various compressibility effects leading to model form suggestions for the pressure-strain correlation, pressure-dilatation and dissipation evolution equation. The pressure-strain correlation closure coefficients are established using fixed point analysis by requiring consistency between model and direct numerical simulation asymptotic behavior in compressible homogeneous shear flow. The closure models are employed to compute high-speed mixing-layers and boundary layers in a differential Reynolds stress modeling solver. The self-similar mixing-layer profile, increased Reynolds stress anisotropy and diminished mixing-layer growth rates with increasing relative Mach number are all well captured. High-speed boundary layer results are also adequately replicated even without the use of advanced thermal-flux models or

low Reynolds number corrections.

To reduce the computational burden required for differential Reynolds stress calculations, the present compressible pressure-strain correlation model is incorporated into the algebraic modeling framework. The resulting closure is fully explicit, physically realizable, and is a function of mean flow strain rate, rotation rate, turbulent kinetic energy, dissipation rate, and gradient Mach number. The new algebraic model is validated with direct numerical simulations of homogeneous shear flow and experimental data of high-speed mixing-layers. Homogeneous shear flow calculations show that the model captures the asymptotic behavior of direct numerical simulations quite well. Calculations of plane supersonic mixing-layers are performed and comparison with experimental data shows good agreement. Therefore the algebraic model may serve as a surrogate for the more computationally expensive differential Reynolds stress model for flows that permit the weak-equilibrium simplification.

DEDICATION

Para mi Alma gemela y compañera eterna.

ACKNOWLEDGEMENTS

I would like to thank my co-advisors, Dr. Sharath Girimaji and Dr. Andrew Duggleby, for their seemingly infinite patience, encouragement, and support. I am also indebted to my committee members, Dr. Kalyan Annamalai and Dr. Je-Chin Han, for their kind suggestions and constructive criticism. Dr. Stefan Wallin of the Swedish Defence Research Agency (FOI) provided invaluable and generous guidance in the use of the EDGE solver.

My deepest gratitude goes toward friends and family who selflessly gave much needed assistance throughout this lengthy process. A very special thank you goes to Alma, whose emotional support has been phenomenal: you are a real life saint. Mom and Dad were also always there for me no matter what. I am extremely lucky to have such wonderful parents. Hicham: thanks for giving me your bike after mine was "misplaced", I love that old school Hardrock! Ashraf: thanks for letting me crash on your couch during my final commutes to Aggieland! Gaurav and Zhimin: it was great to have you guys as my office mates, you certainly made the office a fun place to work and learn. Too many other people to list here, but a big BIG thanks to you all!

And finally my Ph.D. would not have been possible without all the fantastic administrative staff at Texas A&M. Karen Knabe, Colleen Leatherman, and Wanda Hamilton were always extraordinarily patient and helpful: without you three ladies the department would surely grind to a halt. Two gentlemen that every day go way above and beyond the call of duty are Todd Pollard and James Munnerlyn: you guys are great, keep up the top-notch work!

Some of this work was funded by the National Aeronautics and Space Administration under contract number NASA-NRA NNX08AB44A with Dr. Dennis Yoder as Program Monitor. Computational resources were provided by the Texas A&M Supercomputing Facility http://sc.tamu.edu/. I gratefully acknowledge financial support from CONACyT, Consejo Nacional de Ciencia y Tecnología http://www.conacyt.gob.mx/.

TABLE OF CONTENTS

LIST OF FIGURES

LIST OF TABLES

1. INTRODUCTION

1.1 Motivation

One of the most surprising effects of compressibility in high-speed fluid flows is its stabilizing influence on mixing [71]. In a propulsion device reduced turbulence levels can be highly detrimental as they reduce the rate at which fuel and oxidizer mix. For over the past two decades, turbulence researchers have sought closure models that can accurately capture the reduced mixing behavior along with the underlying flow physics [3, 20, 57, 72, 77]. The focus of this thesis is on comprehensive physics-based closure model development for compressible shear dominated flows.

Two commonly used tools in the development of turbulence models are direct numerical simulation (DNS) and rapid distortion theory (RDT). Direct numerical simulation solves for all length and time scales and can therefore be thought of as an *exact* solution to the flow equations. On the other hand, rapid distortion theory exclusively takes into account the *linearized* flow equations and is strictly valid only when linear effects dominate. Both tools provide valuable insight into the flow physics and have long served as guiding beacons for turbulence researchers.

The DNS study of Sarkar [71] on compressible homogeneous shear suggests that the gradient Mach number, $M_g \equiv S\ell/a$, is the most important parameter to characterize compressibility effects. Further DNS studies performed by Pantano & Sarkar [57], and Freund & Lele [20] have conclusively shown that the reduced mixing in high-speed shear layers is due to the effect of the pressure-strain correlation. RDT studies of compressible homogeneous shear performed in our research group have identified three regimes of flow-thermodynamics interactions, see Tucker [44], Bertsch [5], and Lavin et al. [45]. Additional RDT and DNS studies that have confirmed both the

relevance of gradient Mach number as well as the compressibility effect of reduced mixing are those performed by Durbin & Zeman [17], Cambon et al. [8], and Simone et al. [77]. Based on the insight gained from the DNS and RDT studies mentioned above, it is reasonable to propose a new compressible pressure-strain correlation model that displays a three-stage behavior (as observed in RDT) and is parameterized with gradient Mach number (as observed in both RDT and DNS).

1.2 Research description and contributions

1.2.1 Pressure-strain correlation modeling for compressible shear flows

The first work in this thesis develops a compressible pressure-strain correlation model and validates it in the context of second-moment closure modeling. The pressure-strain correlation is derived using a consistent and unified modeling paradigm that is able to capture the three key features of compressible shear dominated flows: (i) Reduced mixing-layer spreading rates [10,11,33,35,42,58,69]; (ii) Increase in turbulence anisotropy [20,33,57,71]; and (iii) Reduction of shear Reynolds stress [20,33,57,71]. The model is validated with the supersonic mixing-layer experiments of Goebel & Dutton [33]. Comparison with experimental data shows that the present model is superior to existing compressible and incompressible pressure-strain correlation closures.

The significant contributions of the first work are:

1. Apply a novel three stage modeling paradigm to provide a closure expression for the pressure-strain correlation that is consistent with DNS and RDT results [5, 44, 45, 71].

2. Use fixed point analysis of compressible homogeneous shear DNS [71] to determine the coefficients of a new pressure-strain correlation model as a function

of gradient Mach number.

3. Test a new dissipation rate equation for compressible flows that includes the effect of pressure-dilatation transferring energy from kinetic to internal mode.

4. Verify if the integral lengthscale, $\ell = k^{3/2}/\varepsilon$, can be employed in the definition of gradient Mach number to yield a compressibility parameter in terms of second-moment closure variables.

5. Validate the new pressure-strain correlation model in homogeneous shear flow and inhomogeneous supersonic mixing-layers.

1.2.2 Algebraic Reynolds stress model (ARSM) for compressible shear flows

The second work incorporates the new compressible pressure-strain correlation in the algebraic modeling framework. Algebraic Reynolds stress models are useful for flows that permit the weak-equilibrium assumption. The key advantage of using an algebraic model is that it includes the high-fidelity physics present in second-moment closure modeling at a fraction of the computational cost [22, 23, 25, 76, 89].

The significant contributions of the second work are:

1. Apply a novel three stage modeling paradigm to the pressure-strain correlation and hence the ARSM approach, based on results observed from DNS and RDT [5, 44, 45, 71].

2. Develop a fully explicit algebraic Reynolds stress model for compressible flows by accounting for the changing nature of pressure at different gradient Mach number regimes.

3. Demonstrate that the resulting constitutive relation is physically realizable.

4. Validate the new algebraic model for use in practical engineering applications.

The algebraic model is validated with supersonic mixing-layers. Comparison with experimental data shows that the present model is superior to standard two-equation models, both with and without compressibility corrections.

1.2.3 Second-moment computations of supersonic boundary layers

The final work in this thesis studies modifications to the new compressible pressure-strain correlation model for adequate near-wall behavior.

The significant contributions of the third work are:

1. Test the new compressible pressure-strain correlation model developed in chapter 2 with the Hellsten [36] ω equation in a state of the art research solver (EDGE) [18, 19].

2. Propose simple modifications to both the ω equation and lengthscale definition, that are able to replicate correct high-speed boundary layer behavior observed in experiments [56] and DNS [14].

Computations are performed with both super and hypersonic boundary layers. Comparisons are made with the experimental data of Owen & Horstman [56] and direct numerical simulation results of Duan et al. [14] It is shown that with simple modifications, the new pressure-strain correlation model is able to adequately capture the behavior of high-speed boundary layers.

1.3 Dissertation outline

This dissertation is organized as follows. Chapter 2 develops and validates the compressible pressure-strain correlation model. Chapter 3 incorporates the new pressure-strain correlation into the algebraic modeling framework to obtain a fully explicit and realizable algebraic Reynolds stress model. Extensive validation is performed by comparing against experimental supersonic mixing-layers. Chapter 4 stud-

ies near-wall modifications to the pressure-strain correlation model for applicability in high-speed boundary layers. Conclusions are made in chapter 5 with a brief summary of the findings.

2. PRESSURE-STRAIN CORRELATION MODELING FOR COMPRESSIBLE SHEAR FLOWS

2.1 Introduction

In high-speed flows the complex phenomenon of turbulence is further exacerbated by compressibility effects engendered by the changing nature of pressure at different speed regimes. At low speeds, the role of pressure is to simply uphold the divergence-free state of the velocity field. Consequently, at low Mach number flows pressure is merely a Lagrange multiplier governed by the Poisson equation. As the flow progresses to higher speeds, the nature of pressure changes drastically. Pressure becomes a *bona fide* thermodynamic variable that is governed collectively by the energy equation, equation of state and calorific equation of state (see figure 2.1). At these high speeds, pressure assumes wave-like characteristics leading to intricate interactions with the velocity field resulting in a profound modification to the nature of turbulence.

The objective of the current work is to develop practical high fidelity closure models for high-speed compressible shear flows. Much of our current understanding of turbulence flow physics and resulting closure model development is in the context of incompressible velocity and Poisson pressure fields. Attempts at modeling compressibility effects as straightforward extensions of incompressible models have only been marginally successful. The lack of closure modeling success can be attributed to the inability to account for the change in the pressure paradigm at higher speeds. Compressible flow closure modeling must necessarily involve three distinct steps: (i) Identification of the critical compressibility physics absent at lower speeds; (ii) Development of a unified closure framework in which various compress-

ibility features can be incorporated into the model in a self-consistent manner; and (iii) Establishment of the cause-effect relationship between closure coefficients and resulting model behavior leading to a clear validation road map.

2.1.1 Relevant compressible physics

High-speed and compressibility effects profoundly alter archetypal turbulence which is the subject of multitude of studies in literature. Most importantly, the flow develops a dilatational component of velocity field that can lead to shocks, density variations and other effects. Variations in transport coefficients as a function of temperature can also be significant for compressible flows. Despite the evident complexity, the turbulence phenomenon is still governed by the Navier–Stokes equations with additional effects manifesting through density, pressure and transport coefficients. For a given equation of state, any distinction between incompressible and compressible turbulence must manifest only through pressure and transport coefficients. In recent years, many of the consequences of compressibility on turbulence have been examined [6, 8, 45, 46, 49, 57, 71].

Comprehensive modeling of compressible turbulence must address: (i) pressure effects; (ii) transport coefficient effects; and (iii) near-wall phenomena. This represents a big challenge that is best addressed in stages. Each of the three categories represents a distinctly different physical process and can be modeled independently. Pressure effects are expected to be dominant in free shear flows and the other two can be significant in wall-bounded flows. Modeling all three effects simultaneously represents a big challenge and it is best to approach each category separately. In this work the focus is on pressure-related effects.

Four important pressure-related aspects of compressible turbulence are now identified that are most relevant for engineering applications and hence must be among

the first to be incorporated into practical closure models. (i) First and foremost closure models must capture the change in flow stability characteristics. It is now well established that compressible shear flows are more stable than their incompressible counterparts. (ii) Compressible turbulence exhibits a much higher degree of velocity fluctuation anisotropy than incompressible turbulence under similar conditions. The degree of anisotropy increases with Mach number. (iii) The flow field is coupled with thermodynamic variables leading to strong interactions between conservation of mass, momentum and energy equations. The flow-thermodynamics interactions lead to interchange between kinetic and potential (pressure field) energies. (iv) The classical Kolmogorov energy cascade picture may not be valid in compressible turbulence due to the above kinetic-potential energy exchanges. It is vital that all these interconnected phenomena be incorporated into closure models in a self-consistent manner.

Compressibility effects pertaining to the energy equation, transport coefficients, and near-wall effects are not considered in this study. The constituent phenomena of these effects are distinct from pressure effects and their model development can proceed independently.

2.1.2 Second-moment closure framework

Second-moment closure (SMC) [64] represents the lowest turbulence description level at which various compressible unclosed phenomena such as pressure-strain correlation and pressure-dilatation can be isolated and modeled with some degree of fidelity to the underlying physics. Despite the recent advances in direct numerical simulations (DNS) and large-eddy simulations (LES), Reynolds-averaged Navier–Stokes (RANS) methods such as SMC continue to be used extensively for practical applications. Lower order RANS models can be systematically derived from SMC

using the weak equilibrium assumption [22, 23, 25, 26, 61, 67, 89] rendering any advances in SMC invaluable to the entire hierarchy of RANS methods. In recent times, variable-resolution (VR) approaches that optimally combine the advantages of LES and RANS are gaining prominence for engineering computations. The use of VR methods is expected to increase and this approach may indeed emerge as the most viable computational design tool of the future. Many VR closures [9, 30, 32] can be derived formally from a parent RANS closure employing the averaging invariance principle [24, 84]. Any improvements in SMC models can be incorporated to VR methods. Furthermore, SMC can also serve as the basis of Langevin and probability density function (PDF) methods [16, 62]. Thus, SMC developments continue to be important for both near-term RANS and long-term VR turbulence computations. In the SMC approach, flow stabilization and anisotropization manifest through the pressure-strain correlation [57, 71], flow-thermodynamics interaction and kinetic-potential energy exchange is brought about by pressure-dilatation, and the change in the spectral cascade rate affects the dissipation rate equation. Therefore, the focus in this study is restricted to the closure modeling of pressure-strain correlation, pressure-dilatation, and dissipation.

Pressure-strain correlation modeling is commonly considered the biggest challenge to accurately computing complex turbulent flows. Although much progress has been made for incompressible flows [27, 38, 43, 66, 78, 83], finding an adequate compressible pressure-strain correlation has proven to be an elusive task. Some of the earliest work towards the development of a compressible pressure-strain correlation closure is that done by Cambon et al. [8] and Adumitroaie et al. [1] Cambon et al. [8] propose an exponential decay of the rapid pressure-strain correlation as a function of gradient Mach number. Their model is found to agree well with DNS of axially compressed turbulence. Adumitroaie et al. [1] incorporate the effects of

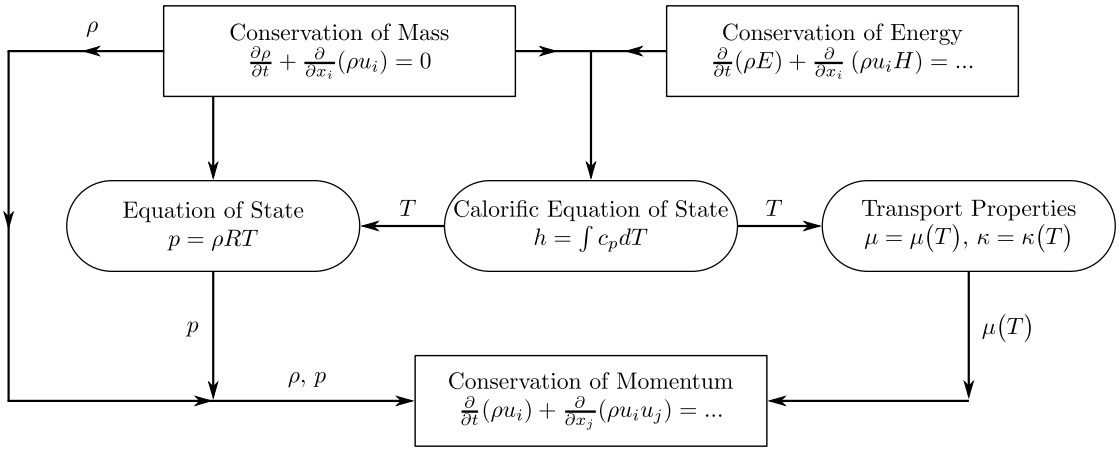

Figure 2.1: Dynamics of compressible flows.

pressure-dilatation, compressible dissipation, and mass-flux in Favre averaged SMC simulations of two dimensional high-speed mixing-layers. Although they are able to obtain good agreement with mixing-layer growth rates, their compressibility corrections decrease the streamwise Reynolds stress of high-speed shear layers, contrary to the results observed in experiments [33] and DNS [20, 57]. In a series of studies, Sarkar and co-workers [57, 71, 72] demonstrate that many of the compressibility effects in shear turbulence are due to changes in the character of the pressure-strain correlation. Pantano & Sarkar [57] propose that for mixing-layers the ratio of compressible to incompressible pressure-strain correlation components depend on the relative Mach number: $M_r \equiv \Delta U/\overline{a} = 2(U_1 - U_2)/[(a_1 + a_2)]$, where the subscripts 1 and 2 denote the high and low speed inlets respectively, U is the mean velocity, and a is the speed of sound. Other researchers have attempted to address compressibility effects by modifying incompressible models with a blending function based on turbulent Mach number [21, 37, 40, 41, 53, 59], $M_t \equiv \sqrt{2k}/a$, where k is the turbulent kinetic energy. All authors report reduced spreading rates for compressible mixing-layers and overall better agreement with experimental data when compared to standard incompressible models.

Examples of dissipation (or equivalently lengthscale) equation modeling in compressible flows include the early work of Sarkar [72] and more recently Aupoix [3]. While these models have yielded some plausible results such as reduction in mixing layer thickness, concomitant effects pertaining to increase in anisotropy or the exchange of energy between kinetic and potential (thermodynamic) forms are not explained. It is now widely recognized that the dominant compressibility effect manifests via the pressure-strain correlation [71].

2.1.3 Present work

The main features of this work are now introduced.

2.1.3.1 Closure modeling framework

In this work a unified framework for the development of physics-based closure models is presented for the various manifestations of compressibility effects – pressure-strain correlation (stabilization and anisotropy), pressure-dilatation (kinetic-potential energy transfer) and corrections to the dissipation equation (spectral cascade modification). The framework is based on the recognition of the changing behavior of pressure at different Mach number regimes and identification of the consequent effects on turbulence. Specifically, the interaction/coupling between pressure and inertial physics is examined as pressure goes from a thermodynamic variable in high-speed flows to a Lagrange multiplier whose only role is to impose the dilatation-free constraint on the velocity field at low speeds. The framework proposal draws heavily from many DNS results [20, 46, 57, 77] and RDT analyses [5, 6, 45] to characterize the behavior of pressure at various speed regimes. At very high Mach numbers, pressure effects are insignificant in comparison with inertial effects. At very low Mach numbers, it can be argued that pressure acts rapidly to prevent any change in the divergence of the velocity field. At intermediate Mach numbers, pressure evolves

according to a wave-equation. In this regime, flow-thermodynamics interactions can be complex and the pressure-strain correlation needs to be modeled appropriately. Thus, a physics-based SMC model must necessarily account for the changing character of the pressure-strain correlation, pressure-dilatation and consequent changes in the spectral cascade rate at the various regimes. Practical considerations require that the starting point be from a standard incompressible pressure-strain correlation closure form and add dilatational terms suggested by RDT and DNS findings. Once the pressure-strain correlation model is established, the pressure-dilatation model is obtained by taking the trace. The modification to the dissipation equation comes from the consideration of what constitutes spectral cascade in compressible turbulence. The model proposal is based on the argument that any kinetic energy converted to internal energy by the action of pressure-dilatation will not contribute to the cascade. Thus, the models of the various compressibility effects are derived in a self-consistent manner using a unified closure framework.

2.1.3.2 Fixed point analysis

An important step in the development process is to establish the closure model coefficients for the broadest range of applicability. Compressible homogeneous shear flow is a quintessential member of the shear flow family that contains the gist of the dominant physics resident in other members [71]. Fixed point analysis [27] can be used to establish the causal relationship between model coefficients and the asymptotic model behavior in homogeneous flows. While such analysis has been widely used in incompressible flows [27, 81–83], it has not been extended to compressible flows. In this study, fixed point analysis is extended to compressible shear turbulence. This causal relationship is employed to determine the model coefficients as functions of gradient Mach number, $M_g \equiv S\ell/a$. The coefficients are determined by

seeking consistency between the model fixed point behavior and the self-similar DNS asymptotic state anisotropy in compressible homogeneous shear flow.

2.1.3.3 Closure model validation

The model is used to compute transient homogeneous shear flow behavior and high-speed mixing and boundary layers. The model results are validated against DNS and experimental data in the above three flows. Remarkably, the pressure-strain correlation coefficients require no modification from the compressible homogeneous shear DNS calibrations to accurately capture the supersonic mixing-layer spreading rates and therefore the Langley curve [42]. Its performance in high-speed boundary layers is also quite adequate even without accounting for near-wall effects, this feature is shown in chapter 4.

2.1.3.4 Chapter outline

The outline of this chapter is as follows. Section 2.2 presents the SMC equations for compressible turbulence and identifies the terms that require closure modeling. The underlying physics of each closure term is discussed in § 2.3. In § 2.4, the closure models are developed and the coefficients are determined by comparing model fixed points with long time behavior of compressible homogeneous shear DNS. Validation of the model in supersonic compressible mixing-layer computations is presented in § 2.5. Conclusions are made in § 2.6 with a short summary.

2.2 Second-moment closure modeling

For compressible flows it is common practice to apply Favre averaging to the Navier–Stokes equations. The Favre average of a variable ϕ is defined as

$$\tilde{\phi} = \frac{\overline{\rho\phi}}{\overline{\rho}}, \tag{2.1}$$

where ρ is the fluid density, $\overline{(\cdot)}$ denotes a Reynolds average, and $\tilde{(\cdot)}$ a Favre average. In the following ϕ' and ϕ'' denote Reynolds and Favre fluctuations respectively. The Reynolds stress tensor is given by

$$R_{ij} = \frac{\overline{\rho u_i'' u_j''}}{\overline{\rho}}. \tag{2.2}$$

Using these definitions the Favre averaged conservation of mass, momentum and total energy equations become

$$\frac{\partial \overline{\rho}}{\partial t} + \frac{\partial}{\partial x_i}(\overline{\rho}\tilde{u}_i) = 0, \tag{2.3}$$

$$\frac{\partial}{\partial t}(\overline{\rho}\tilde{u}_i) + \frac{\partial}{\partial x_j}(\overline{\rho}\tilde{u}_i\tilde{u}_j) = -\frac{\partial \overline{p}}{\partial x_i} + \frac{\partial}{\partial x_k}\left(\overline{\sigma}_{ik} - \overline{\rho}R_{ik}\right), \tag{2.4}$$

$$\begin{aligned}\frac{\partial}{\partial t}(\overline{\rho}E) + \frac{\partial}{\partial x_i}\left(\overline{\rho}\tilde{u}_i H\right) =& \frac{\partial}{\partial x_j}\Bigg[-q_{L_j} - \overline{\rho u_j'' h''} + \overline{\sigma_{ij} u_i''} - \frac{1}{2}\overline{\rho u_i'' u_i'' u_j''} \\ &+ \tilde{u}_i\left(\overline{\sigma}_{ij} - \overline{\rho}R_{ij}\right)\Bigg],\end{aligned} \tag{2.5}$$

where $\overline{p}$ is the average pressure, $\tilde{e}$ specific internal energy, E total energy, $\tilde{h}$ specific enthalpy, H total enthalpy, $\overline{\sigma}_{ij}$ the viscous stress tensor, and q_{L_j} the molecular heat flux vector. The total energy and enthalpy are given by

$$E = \tilde{e} + \frac{\tilde{u}_i\tilde{u}_i}{2} + k, \quad H = \tilde{h} + \frac{\tilde{u}_i\tilde{u}_i}{2} + k, \tag{2.6}$$

where $k = R_{ii}/2$ is the turbulent kinetic energy. For a Newtonian fluid, the viscous stress tensor is

$$\sigma_{ij} = \mu\left(\frac{\partial u_i}{\partial x_j} + \frac{\partial u_j}{\partial x_i}\right) - \frac{2}{3}\mu\frac{\partial u_k}{\partial x_k}\delta_{ij}, \quad \delta_{ij} = \begin{cases} 1 & \text{if } i = j, \\ 0 & \text{otherwise,} \end{cases} \tag{2.7}$$

where μ is the molecular viscosity, and δ_{ij} the Kronecker delta tensor. The molecular heat flux vector is

$$q_{L_j} = -\kappa\frac{\partial \tilde{T}}{\partial x_j}, \tag{2.8}$$

where κ is the thermal conductivity, and $\tilde{T}$ temperature. The focus of this work is on modeling pressure effects in the Reynolds stress equation. For the sake of completeness, models for the other unclosed terms are first briefly discussed.

2.2.1 Energy equation closures

As indicated in the introduction, this work focuses only on pressure-related phenomena. Here the simplest energy equation closures in literature are merely indicated. The correlation between fluctuating velocity and fluctuating specific enthalpy is the turbulent heat transfer and is usually modeled as

$$q_{T_j} = \overline{\rho u_j'' h''} = -\frac{c_p \mu_t}{Pr_t}\frac{\partial \tilde{T}}{\partial x_j}, \tag{2.9}$$

where Pr_t is the turbulent Prandtl number, μ_t is the turbulent viscosity, and c_p is the specific heat at constant pressure. The turbulent viscosity is computed using

$$\mu_t = \frac{\overline{\rho} C_\mu k^2}{\varepsilon}, \quad k = \frac{1}{2}R_{ii}, \quad \varepsilon = \frac{1}{2}\varepsilon_{ii}, \tag{2.10}$$

where k is the turbulent kinetic energy, and ε the dissipation rate. The modeling constants used are

$$C_\mu = 0.09, \quad Pr_t = 0.85. \tag{2.11}$$

An algebraic closure model for the turbulent heat flux in high-speed shear flows has been developed by Bowersox [7], and used to predict velocity and temperature profiles of supersonic and hypersonic boundary layers with high accuracy. Bowersox [7] shows that large improvements in near-wall predictions can be made by using a sophisticated turbulent heat flux model and accounting for variable Pr_t effects.

The two terms $\overline{\sigma_{ij}u_i''}$ and $\frac{1}{2}\overline{\rho u_i'' u_i'' u_j''}$ on the right hand side of equation (2.5) are the molecular diffusion and turbulent transport of turbulence kinetic energy. If $\overline{\rho}k \ll \overline{p}$, these terms can be neglected, [94]. However, for hypersonic flows these terms may be important, and the following approximation has been suggested

$$\overline{\sigma_{ij}u_i''} - \frac{1}{2}\overline{\rho u_i'' u_i'' u_j''} = \left(\mu + \frac{\mu_t}{\sigma_k}\right)\frac{\partial k}{\partial x_j}, \quad \sigma_k = 0.82. \tag{2.12}$$

Introducing equations (2.9) and (2.12) in equation (2.5) yields the modeled total energy equation

$$\frac{\partial}{\partial t}(\overline{\rho}E) + \frac{\partial}{\partial x_i}\left(\overline{\rho}\tilde{u}_i H\right) = \frac{\partial}{\partial x_j}\left[\left(\kappa + \frac{c_p\mu_t}{Pr_t}\right)\frac{\partial \tilde{T}}{\partial x_j} + \left(\mu + \frac{\mu_t}{\sigma_k}\right)\frac{\partial k}{\partial x_j} + \tilde{u}_i\left(\overline{\sigma}_{ij} - \overline{\rho}R_{ij}\right)\right]. \tag{2.13}$$

2.2.2 Reynolds stress closures

The Favre averaged Reynolds stress equation takes the following form

$$\frac{\partial(\overline{\rho}R_{ij})}{\partial t} + \frac{\partial(\overline{\rho}\tilde{u}_k R_{ij})}{\partial x_k} = \overline{\rho}\left(P_{ij} - \varepsilon_{ij}\right) - \frac{\partial T_{ijk}}{\partial x_k} + \Pi_{ij} + \Sigma_{ij}, \tag{2.14}$$

where P_{ij} is the production tensor, ε_{ij} the dissipation tensor, T_{ijk} the turbulent transport tensor, Π_{ij} the pressure-strain correlation, and Σ_{ij} the mass flux coupling tensor. Of the five terms on the right hand side of equation (2.14), the production tensor is the only one in closed form

$$P_{ij} = -R_{ik}\frac{\partial \tilde{u}_j}{\partial x_k} - R_{jk}\frac{\partial \tilde{u}_i}{\partial x_k}. \tag{2.15}$$

The remaining four phenomena require closure modeling

$$\varepsilon_{ij} = \frac{1}{\overline{\rho}}\left(\overline{\sigma'_{jk}\frac{\partial u''_i}{\partial x_k} + \sigma'_{ik}\frac{\partial u''_j}{\partial x_k}}\right), \tag{2.16}$$

$$T_{ijk} = \overline{\rho u''_i u''_j u''_k} + \overline{p' u''_i}\delta_{jk} + \overline{p' u''_j}\delta_{ik} - \overline{\sigma'_{jk} u''_i} - \overline{\sigma'_{ik} u''_j}, \tag{2.17}$$

$$\Pi_{ij} = \overline{p'\left(\frac{\partial u''_i}{\partial x_j} + \frac{\partial u''_j}{\partial x_i}\right)}, \tag{2.18}$$

and

$$\Sigma_{ij} = \overline{u''_i}\left(\frac{\partial \overline{\sigma}_{jk}}{\partial x_k} - \frac{\partial \overline{p}}{\partial x_j}\right) + \overline{u''_j}\left(\frac{\partial \overline{\sigma}_{ik}}{\partial x_k} - \frac{\partial \overline{p}}{\partial x_i}\right). \tag{2.19}$$

2.2.2.1 Turbulent transport

The gradient diffusion model for turbulent transport is assumed to be reasonable even in the presence of compressibility effects. The fundamental arguments that lead to the gradient transport model in incompressible flows continue to be valid in compressible flows as well. With this in mind, as a first step, the transport tensor is modeled using the traditional scalar turbulent diffusivity approach [48]

$$-\frac{\partial T_{ijk}}{\partial x_k} = \frac{\partial}{\partial x_k}\left[\left(\mu + \frac{\mu_t}{\sigma_k}\right)\frac{\partial R_{ij}}{\partial x_k}\right]. \tag{2.20}$$

It is important that this closure be consistent with the energy flux model in equation (2.12). It is quite possible that μ_t may be a function of the Reynolds number. However, there is no clear experimental evidence at this time. Therefore, the investigation of this phenomenon is relegated to the future when appropriate evidence is available.

2.2.2.2 Dissipation tensor

It is suggested in literature that the smallest scales of motion are likely to be isotropic even at reasonably large Mach numbers. This is due to the fact that Mach number effects are less significant at small scales as the characteristic velocity diminishes with scale. Consequently, the Mach number characterizing the smallest scales of motion is small in many flows of interest. Thus, the isotropic model is assumed to remain valid for the dissipation tensor

$$\varepsilon_{ij} = \frac{2}{3}\varepsilon\delta_{ij}. \tag{2.21}$$

As in incompressible turbulence, a model evolution equation must be solved to find the turbulent dissipation rate ε. In all closure models to date, the dissipation rate is taken to be the spectral cascade rate. The spectral cascade rate equation must be enhanced to include the effect of compressibility. Furthermore, the influence of variation in transport coefficient μ on dissipation must be understood and modeled. These issues are addressed in detail in the next section.

2.2.2.3 Turbulent mass flux

DNS of supersonic shear layers [57] has shown the mass flux coupling term Σ_{ij} to be negligible in the Reynolds stress budgets. Since the intention is to propose a model that can capture the compressibility effects associated with high-speed boundary

and mixing-layers, it is reasonable to neglect this term. However, for flows driven by density gradients, this term is of paramount importance [51, 52]. For such flows, Ristorcelli [65] presents an algebraic turbulent mass flux model.

2.2.2.4 Pressure-effects closures

The fluctuating pressure equation for compressible flows has been analyzed by Thacker et al. [88],

$$\left[\frac{1}{a^2}\left(\frac{\partial}{\partial t}+\tilde{u}_j\frac{\partial}{\partial x_j}\right)^2-\frac{\partial^2}{\partial x_j\partial x_j}\right]p'=\left\{\frac{\partial^2}{\partial x_i\partial x_j}\left(\rho u_i''u_j''-\overline{\rho}R_{ij}\right)\right\}$$
$$+\left\{2\frac{\partial\tilde{u}_i}{\partial x_j}\frac{\partial\left(\rho u_j''\right)}{\partial x_i}+\rho'\frac{\partial\tilde{u}_i}{\partial x_j}\frac{\partial\tilde{u}_j}{\partial x_i}+\left(\frac{\partial}{\partial t}+\tilde{u}_j\frac{\partial}{\partial x_j}\right)\tilde{u}_i\frac{\partial p'}{\partial x_i}\right\}. \tag{2.22}$$

The first set of terms within curly braces on the right hand side is called the “slow" pressure, which is non-linear in the fluctuating velocity. Its response to changes in the mean velocity field is slow due to modifications of the fluctuating velocity field occurring over longer time periods compared to mean velocity field modifications. The second set of terms within curly braces on the right hand side of equation (2.22) is called “rapid" pressure and is linear in the fluctuating velocity field. The adjective rapid, comes from the fact that this portion of the pressure field reacts rapidly upon a change in the mean flow. The linear part captures the interaction between mean and fluctuating fields while the non-linear part accounts for interactions among fluctuating fields. Thacker et al. [88] provide a detailed discussion of the fluctuating pressure equation in the context of supersonic mixing and boundary layers.

Classical pressure-strain correlation modeling methodology [83] commences from the following form

$$\Pi_{ij}=\overline{\rho}\varepsilon\mathcal{A}_{ij}\left(\mathbf{b}\right)+\overline{\rho}k\mathcal{M}_{ijkl}\left(\mathbf{b}\right)\frac{\partial\tilde{u}_k}{\partial x_l}, \tag{2.23}$$

where

$$b_{ij} \equiv \frac{R_{ij}}{2k} - \frac{1}{3}\delta_{ij}, \tag{2.24}$$

is the anisotropy tensor. Corresponding to slow and rapid pressure, the pressure-strain correlation is also decomposed into its slow and rapid parts

$$\Pi_{ij} = \Pi_{ij}^{(s)} + \Pi_{ij}^{(r)}, \quad \Pi_{ij}^{(s)} = \overline{\rho}\varepsilon\mathcal{A}_{ij}\left(\mathbf{b}\right), \quad \Pi_{ij}^{(r)} = \overline{\rho}k\mathcal{M}_{ijkl}\left(\mathbf{b}\right)\frac{\partial\tilde{u}_k}{\partial x_l}. \tag{2.25}$$

Dimensional analysis and representation theory [60, 79] of tensor-valued isotropic functions allows the pressure-strain correlation to be written as

$$\Pi_{ij} = \overline{\rho}\varepsilon f_{ij}\left(\mathbf{b}, \tau\mathbf{S}, \tau\mathbf{W}\right) = \overline{\rho}\varepsilon\sum_k C_k T_{ij}^k, \quad \tau = \frac{k}{\varepsilon}, \tag{2.26}$$

where

$$S_{ij} = \frac{1}{2}\left(\frac{\partial\tilde{u}_i}{\partial x_j} + \frac{\partial\tilde{u}_j}{\partial x_i}\right) - \frac{1}{3}\frac{\partial\tilde{u}_k}{\partial x_k}\delta_{ij}, \quad W_{ij} = \frac{1}{2}\left(\frac{\partial\tilde{u}_i}{\partial x_j} - \frac{\partial\tilde{u}_j}{\partial x_i}\right), \tag{2.27}$$

are the modified rate of strain and rotation rate tensors respectively. The C_k coefficients in equation (2.26) are in general scalar functions of the independent tensor invariants of T_{ij}^k, although many popular models use constant values for some or all of these coefficients [39, 43, 83]. The final compressibility effect that requires special consideration is pressure-dilatation. This effect is absent in incompressible flows but plays the vital role of transferring energy between internal and dilatational kinetic energies in compressible flows. Closure models for the pressure-strain correlation, pressure-dilatation, and dissipation rate are the focus of the next section.

2.3 Compressible shear turbulence: physics and closure modeling

The fundamental physics of flow-thermodynamic interactions that leads to stabilization of turbulence has been carefully investigated and reported in three preceding

works from our research group – Lavin et al. [45], Lee & Girimaji [46], and Bertsch et al. [6] The linear aspects of flow stabilization that is generic to compressible shear flows has been examined thoroughly in Lavin et al. [45] using RDT. Pressure-strain correlation model implications are then investigated meticulously in Bertsch et al. [6] The non-linear aspects of the pressure-strain correlation are studied in Lee & Girimaji [46] wherein the slow pressure physics are established. All of these findings form the basis of the model development in this study. Thus, the present work represents the culmination of a series of studies directed towards understanding fundamental compressible shear flow physics and incorporating into closure models using sound first principles.

In this section the known physics of compressible shear turbulence are presented and closure models are proposed. Following the incompressible turbulence precedent, linear and non-linear physics effects are separated as they represent distinctly different aspects of turbulence dynamics. The focus is on the pressure-strain correlation term and its consequences on pressure-dilatation and spectral cascade rate.

The dimensionless parameters of relevance are the gradient Mach number (M_g) and turbulent Mach number (M_t) defined as:

$$M_g \equiv \frac{S\ell}{a}, \quad M_t \equiv \frac{\sqrt{2k}}{a}. \tag{2.28}$$

The gradient Mach number is the ratio of shear to acoustic timescale, whereas the turbulent Mach number characterizes the magnitude of velocity fluctuations relative to speed of sound. The relative magnitudes of the mean flow distortion timescale ($\tau_d = 1/S$), and acoustic timescale ($\tau_a = \ell/a$) determine the magnitude of the gradient Mach number ($M_g = \tau_a/\tau_d$). In hypersonic flows of aerospace engineering interest, gradient Mach numbers can be much larger than unity. However, turbulent

Mach numbers are typically smaller than unity. In the model development phase, we restrict ourselves to a parameter range of practical utility in hypersonic flight vehicles: gradient Mach numbers up to 10 and turbulence Mach numbers less than 0.6.

2.3.1 Linear pressure-strain correlation

As mentioned in the previous section, linear or rapid pressure corresponds to the fluctuating pressure field that arises due to the presence of the mean velocity gradient. In the rapid distortion limit, this is the only pressure fluctuation of relevance. It stands to reason that the parameterization of linear pressure-strain correlation involve the mean-flow parameters. Compressible rapid distortion theory studies have shown that the linear pressure-strain correlation is profoundly affected by compressibility [5, 8, 45, 50, 77]. The study by Simone et al. [77] suggests that the rapid or linear pressure is chiefly responsible for the reduction of turbulent kinetic energy growth rates in compressible homogeneous shear at high gradient Mach number. The implication for modeling is that critical changes to the incompressible rapid pressure-strain correlation closure are needed for applicability in compressible flows. Furthermore, these changes should be parameterized by the gradient Mach number [8, 17, 45].

The findings of the rapid distortion studies of compressible homogeneous shear flow performed by Bertsch [5] and Lavin et al. [45] are now briefly discussed. A schematic of homogeneous shear flow is shown in figure 2.2. Figures 2.3 and 2.4 show the turbulent kinetic energy evolution in acoustic and shear time respectively. From figure 2.3 a three stage behavior in the growth rate of turbulent kinetic energy can be observed. This three stage behavior can be used to establish a fundamental guideline for the effect of pressure at low, intermediate, and high gradient Mach

$$t = 0: \quad S = \frac{\partial \tilde{u}_1}{\partial x_2}, \quad R_{ij} = \frac{2k}{3}\delta_{ij}$$
$$t > 0: \quad S = \frac{\partial \tilde{u}_1}{\partial x_2}, \quad R_{ij} \neq \frac{2k}{3}\delta_{ij}$$

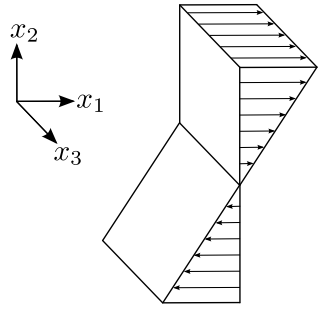

Figure 2.2: Schematic of homogeneous shear flow.

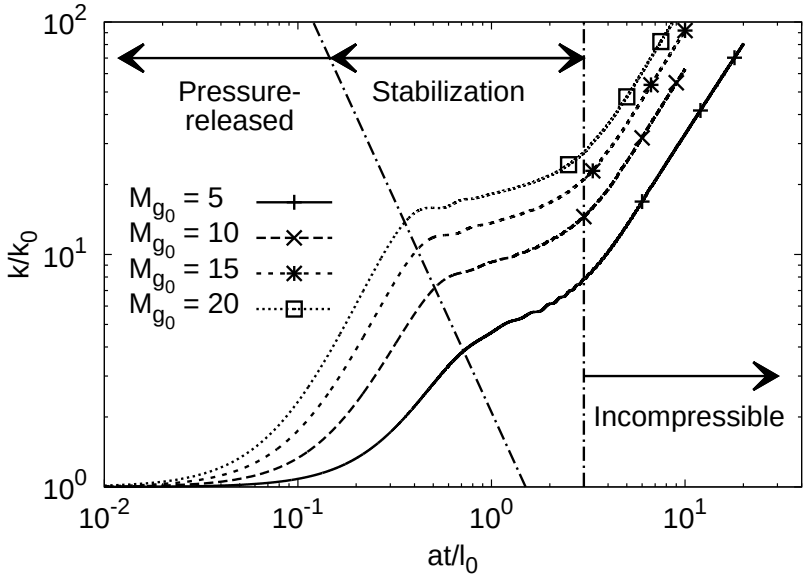

Figure 2.3: Turbulent kinetic energy evolution in acoustic time. RDT of compressible homogeneous shear flow, taken from Bertsch [5].

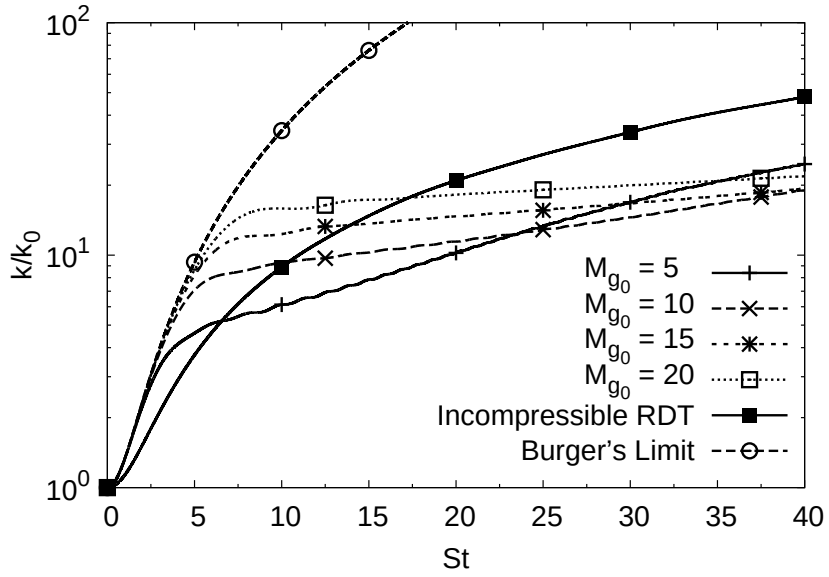

Figure 2.4: Turbulent kinetic energy evolution in shear time. RDT of compressible homogeneous shear flow, taken from Bertsch [5].

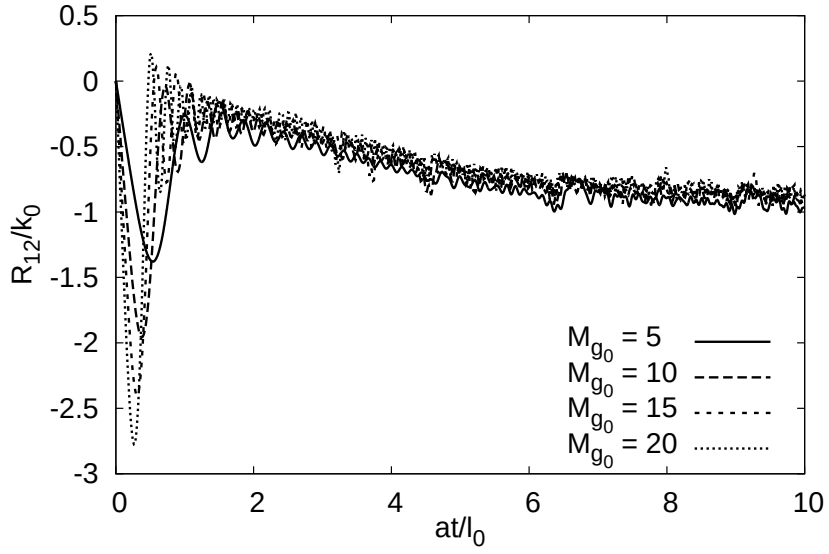

Figure 2.5: Normalized Reynolds shear stress evolution in acoustic time. RDT of compressible homogeneous shear flow, taken from Bertsch [5].

number.

Regime 1 – $M_g \gg 1$, $\tau_a \gg \tau_d$**:** In this regime the acoustic time scale is much larger than that of shear. Pressure responds too slowly to affect the flow dynamics. As a result, turbulence evolution is dominated by the production process

$$\Pi_{ij} \ll \overline{\rho} P_{ij}. \tag{2.29}$$

This regime is characterized by minimal flow thermodynamics interactions as well as high levels of Reynolds stress anisotropy. The turbulent kinetic energy growth rate in the pressure-released stage increases with initial gradient Mach number, as can be seen for $St < 2$ in figure 2.4. In this limit, the flow evolution can be closely approximated by the three-dimensional Burgers equation – which is the Navier–Stokes equation without the pressure term [6].

Regime 2 – $M_g \sim 1$, $\tau_a \sim \tau_d$**:** This flow regime occurs when the mean distortion and acoustic timescales are of similar magnitude. In this stage both inertial and pressure effects play critical roles. The acoustic character of the pressure field is most evident in this regime. Pressure waves are established in the flow normal (shear) direction. This leads to oscillatory behavior of shear normal velocity fluctuations [45]. Consequently the fluctuating shear stress also evolves in an oscillatory manner [5, 45]. The small integrated value of R_{12} in this stage results in a negligible net growth of turbulent kinetic energy as seen in figure 2.3. During this stabilization stage Bertsch [5] demonstrates that on an average

$$\Pi_{12}^{(r)} + \overline{\rho} P_{12} \approx 0. \tag{2.30}$$

This regime has the highest level of flow thermodynamics interactions, leading

to maximum energy exchange between turbulent kinetic and potential forms. The spectral cascade rate is affected the most in this regime. Anisotropy is moderate and flow stabilization is incipient. Based on these observations, it is suggested that shear production blocking by the corresponding pressure-strain correlation component is the critical aspect of flow physics that must be incorporated into compressible closure models.

Regime 3 – $M_g \ll 1$, $\tau_a \ll \tau_d$**:** At low gradient Mach number, pressure assumes the role of enforcing incompressibility and is governed by a Poisson equation. Pressure equilibrates almost instantaneously to inertial effects and maintains incompressibility. Any remnant dilatational fluctuations are rapidly dissipated by viscous effects. For this low M_g regime, a standard incompressible pressure-strain correlation model is taken to be adequate

$$\Pi_{ij} \approx \Pi_{ij}^{I}. \tag{2.31}$$

This regime is characterized by negligible flow thermodynamics interactions with low levels of anisotropy and no flow stabilization. In this regime, the turbulent kinetic energy growth rates for all cases are reasonably similar to that of low gradient Mach number, as seen in figure 2.3. The RDT computations of Bertsch [5] demonstrate that for this stage the normalized shear Reynolds stress goes to an approximately constant value independent of initial gradient Mach number, as seen for large acoustic time in figure 2.5.

2.3.1.1 Closure modeling of the linear pressure-strain correlation

In summary, Lavin et al. [45] conclude that dilatational fluctuations dominate the flow physics in Regimes 1 and 2 whereas solenoidal fluctuations dominate in Regime

3. Residual dilatations may exist in Regime 3 but as a modeling simplification can be taken to be small and perhaps negligible. Thus motivated a compressible pressure-strain correlation of the following general form [63] is proposed

$$\Pi_{ij}^{(r)} = \overline{\rho}\varepsilon \sum_{k} C_k\left(M_g\right) T_{ij}^{k(r)} - \overline{\rho} C_P\left(M_g\right) P_{ij}. \tag{2.32}$$

For the sake of generality, the coefficients are functions of gradient Mach number. The addition of the production blocking term does not violate form invariance since the production tensor can be expressed as a sum of tensor-valued isotropic functions. The production-blocking term is clearly motivated by the behavior observed in Regime 2 as described above. On the other hand, the dependence of the coefficients on Mach number is to accommodate Regime 1 behavior, wherein the effect of the pressure-strain correlation gradually fades with increasing Mach number.

The same tensor groups found in the rapid pressure-strain correlation of the LRR model [43] are used

$$\begin{aligned}\Pi_{ij}^{(r)} = {} & C_3\left(M_g\right)\overline{\rho}kS_{ij} + C_4\left(M_g\right)\overline{\rho}k\left(b_{ik}S_{jk} + b_{jk}S_{ik} - \tfrac{2}{3}b_{mn}S_{mn}\delta_{ij}\right) \\ & + C_5\left(M_g\right)\overline{\rho}k\left(b_{ik}W_{jk} + b_{jk}W_{ik}\right) - C_P\left(M_g\right)\overline{\rho}P_{ij}.\end{aligned} \tag{2.33}$$

The linearity of equation (2.33) permits a straightforward implementation to the standard Explicit Algebraic Reynolds Stress Model (EARSM) approach [25], a concurrent undertaking to the present modeling efforts.

Some treatments of compressible flows partition the fluctuating velocity field into solenoidal (vortical) and dilatational (acoustic) fields. Dilatational effects are relevant at high Mach numbers in the pressure-released and stabilization regimes. The solenoidal velocity and pressure fields play the dominant role in the incompressible

regime. In this work, the two types of fluctuations are not distinguished explicitly. As mentioned earlier, the two different physical effects are implicit in the nature of the closure in the three stages. Rather, here the focus is on model development in the three regimes identified from the RDT study. It is found that Regimes 1 and 2 are dominated by dilatational fluctuations as the pressure does not effectively impose the divergence-free condition on the velocity gradient field. In Regime 3, the solenoidal aspects are the most important. Thus, the dilatational and solenoidal aspects of flow physics are naturally incorporated in this approach at the appropriate parameter regimes.

2.3.2 Non-linear pressure-strain correlation

Lee & Girimaji [46] performed a DNS study of decaying anisotropic compressible turbulence for a range of turbulent Mach numbers and temperature fluctuations. This study isolates the effects compressibility and thermodynamic fluctuations have on the non-linear pressure-strain correlation in the limit of decaying turbulence. Lee & Girimaji [46] conclude that the return to isotropy of the solenoidal kinetic energy k_s is largely unaffected for moderate turbulent Mach number ($M_t \leq 0.6$), and temperature fluctuations ($T'_{rms}/\overline{T} \leq 0.27$). On the other hand, the dilatational kinetic energy k_d is affected by both turbulent Mach number and temperature fluctuations. However the total kinetic energy field returns to isotropy at approximately the same rate for the entire parameter range in the study. Therefore, as long as the flows of interest are within the turbulent Mach number and temperature fluctuation parameter range examined in the study, we can use the same the form of the slow incompressible pressure-strain correlation for compressible flows. However, this does not preclude modifications to the slow pressure-strain correlation model at higher turbulent Mach number.

2.3.2.1 Closure modeling of the non-linear pressure-strain correlation

Based on the findings above, the Rotta [68] model is chosen for the slow pressure-strain correlation

$$\Pi_{ij}^{(s)} = -C_1 \left(M_t\right) \overline{\rho} \varepsilon b_{ij}. \tag{2.34}$$

The dependence on M_t reflects the degree of influence of dilatational fluctuations. The modification can be expected to be higher at larger M_t due to a greater fraction of dilatational fluctuations.

For completeness, the full form of the pressure-strain correlation used in this work is given. For notational convenience the dependence of the C_k and C_P coefficients on M_g is not shown explicitly.

$$\begin{aligned} \Pi_{ij} = & - C_1 \overline{\rho} \varepsilon b_{ij} + C_3 \overline{\rho} k S_{ij} + C_4 \overline{\rho} k \left(b_{ik} S_{jk} + b_{jk} S_{ik} - \tfrac{2}{3} b_{mn} S_{mn} \delta_{ij} \right) \\ & + C_5 \overline{\rho} k \left(b_{ik} W_{jk} + b_{jk} W_{ik} \right) - C_P \overline{\rho} P_{ij}. \end{aligned} \tag{2.35}$$

2.3.3 Linear pressure-dilatation

Sarkar et al. [73] and Lavin et al. [45] report that the linear pressure-dilatation acts to bring about equipartition between dilatational kinetic energy and turbulent internal energy. In homogeneous shear flow without heat release, the net energy transfer is from kinetic to internal form. This is the most fundamental interaction pressure-dilatation can cause, and should at a minimum be the basis for pressure-dilatation modeling.

2.3.3.1 Closure modeling of the linear pressure-dilatation

The trace of equation (2.32) leads to the following linear pressure-dilatation model

$$\frac{1}{2}\Pi_{ii}^{(r)} = -\overline{\rho}C_P\left(M_g\right)P = \overline{\rho}kC_P\left(M_g\right)\left(2b_{mn}S_{mn} + \frac{2}{3}\frac{\partial\tilde{u}_m}{\partial x_m}\right), \quad P = \frac{1}{2}P_{ii}. \tag{2.36}$$

For positive C_P, the above model guarantees that for shear dominated flows in the absence of heat release the net transfer of energy is from kinetic to internal, as observed in DNS.

2.3.4 Non-linear pressure-dilatation

Livescu et al. [49] performed a DNS study on the effects of heat release in reacting turbulent shear flow. They report that significant heat release can change the direction of energy transfer due to pressure-dilatation. Lee & Girimaji [46] find similar trends for imposed temperature fluctuations on decaying anisotropic compressible turbulence. Although the direction of energy transfer is affected by heat release and temperature fluctuations, the role of the non-linear and linear pressure-dilatation is the same – enforce equipartition between dilatational kinetic and turbulent internal energies. The observed physics can be incorporated into a closure model by following the guidelines given by Lee & Girimaji [46].

2.3.4.1 Closure modeling of the non-linear pressure-dilatation

In the cases of interest here, the slow term is expected to be negligible and hence a non-linear pressure-dilatation model is not used in the calibration or computations.

$$\Pi^{(s)} = \frac{1}{2}\Pi_{ii}^{(s)} = 0. \tag{2.37}$$

2.3.5 Dissipation rate

Closure modeling of dissipation in compressible flows entails consideration of three novel aspects absent in incompressible flows: (i) dilatational dissipation, (ii) the effect of large viscosity gradients on solenoidal dissipation, and (iii) inviscid passage of energy from kinetic to internal (due to pressure-dilatation) and thus by-passing the spectral cascade. In the following, each point is discussed individually.

It is now commonly accepted [80] that in the absence of heat release, the dilatational to solenoidal dissipation ratio scales as

$$\varepsilon_d/\varepsilon_s \sim M_t^4. \tag{2.38}$$

Livescu et al. [49] show that for compressible homogeneous shear without heat release, dilatational dissipation is small compared to solenoidal dissipation. However the magnitude of dilatational dissipation can be strongly magnified by intense heat release. Lee & Girimaji [46] estimate that the extent of dilatational kinetic energy is proportional to the pressure fluctuation induced by heat release. It is clear that the presence of significant heat release can severely complicate the energetic turbulence dynamics. The development of an all-encompassing model is beyond the scope of the current work. Instead, as a first step, the focus is on non-reacting compressible turbulence with moderate turbulent Mach number, and thermodynamic fluctuations. For the parameter range of interest, $M_t \leq 0.6$, the effect of compressible dissipation can be neglected.

Due to the high degree of interactions between momentum, energy, and state equations in compressible flow, large gradients of temperature and therefore viscosity can be expected. Under these circumstances, the validity of Taylor's postulate that dissipation rate is independent of viscosity at high Reynolds number can come into

question. Lee et al. [47] use DNS to examine if Taylor's postulate holds true in a variable viscosity medium. They find that the velocity gradients rapidly adapt to the viscosity field, and within one-half eddy turnover time, the dissipation rate becomes independent of viscosity. Thus as a first approximation, it can be expected that even in the presence of large gradients of viscosity, Taylor's postulate is valid after a brief initial transient period.

For non-reacting compressible homogeneous shear, pressure-dilatation transfers turbulent kinetic energy to turbulent internal energy. This energy transfer can potentially affect the dissipation rate equation. In the standard incompressible dissipation rate model, the spectral cascade rate is taken to be equal to the dissipation rate. However for compressible flows, the energy transferred by pressure-dilatation does not cascade down to smaller scales as the spectral energy flux. In this work, an attempt is made to determine if this reduction in the cascade rate must be incorporated into the closure model.

2.3.5.1 Closure modeling of dissipation

A turbulent dissipation rate equation is presented that is suitably modified from its standard form to allow for the effect of pressure-dilatation

$$\frac{\partial}{\partial t}(\overline{\rho}\varepsilon) + \frac{\partial}{\partial x_i}(\overline{\rho}\varepsilon\tilde{u}_i) = \frac{\partial}{\partial x_j}\left[\left(\mu + \frac{\mu_t}{\sigma_\varepsilon}\right)\frac{\partial \varepsilon}{\partial x_j}\right] + C_{\varepsilon_1}\overline{\rho}\frac{\varepsilon}{k}P\left(1 - C_P\right) - C_{\varepsilon_2}\overline{\rho}\frac{\varepsilon^2}{k}. \quad (2.39)$$

The overall effect of including C_P in the dissipation rate equation is to reduce the production of dissipation. To assess the impact of cascade by-pass, two closure proposals for the dissipation equation are presented: closure GG-I uses the standard dissipation rate equation (equation (2.39) without the C_P term) and closure GG-II includes the proposed modification.

2.3.6 Choice of lengthscale

The most appropriate lengthscale for use in the gradient Mach number definition is the characteristic acoustic lengthscale. Sarkar [71] characterizes this as the representative lengthscale in the shear direction. Lavin et al. [45] show that the acoustic component is dominant in the shear direction and hence Lavin et al. [45] and Sarkar [71] are consistent with one another. Such a lengthscale can also be of use in modeling dilatational dissipation. However, in the traditional second-moment approach the only lengthscale available is the integral scale given by $\ell = k^{3/2}/\varepsilon$. Two possible options for obtaining the requisite acoustic lengthscale are: (i) solve a modeled evolution equation for the acoustic lengthscale, and (ii) relate the acoustic lengthscale to the integral lengthscale by suitable calibration. Development of a new modeled evolution equation for the acoustic lengthscale, while highly desirable, is the more difficult of the two options. Such an equation is likely to be even more empirical than the incompressible lengthscale equation, and would represent a major paradigm shift. In this work, the simpler alternative is chosen and the development of an acoustic lengthscale equation is deferred to the future. Thus, in the present work compressibility effects are characterized using a gradient Mach number that utilizes $\ell = k^{3/2}/\varepsilon$ as the lengthscale. Any difference between the acoustic and integral lengthscales is accounted for in the calibration process. With this choice of lengthscale, the gradient and turbulent Mach numbers are related. Therefore the gradient Mach number is the only compressible parameter used in the fixed point analysis. The gradient Mach number is found using

$$M_g \equiv \frac{S\ell}{a}, \quad S = \sqrt{2S_{ij}S_{ij}}, \quad \ell = \frac{k^{3/2}}{\varepsilon}, \quad a = \sqrt{\gamma R\tilde{T}}, \quad \frac{M_t}{M_g} = \sqrt{2}\left(\frac{Sk}{\varepsilon}\right)^{-1}. \quad (2.40)$$

Now that the model forms of the unclosed terms have been established, a validation road map is developed using fixed point analysis.

2.4 Fixed point analysis

Fixed point and dynamical system analysis have long been used for incompressible turbulence closure model development [27, 82, 83]. Analytical relationships between model coefficients and asymptotic behavior can be derived for homogeneous flows. Girimaji [27] states that demanding the model coefficients yield the correct asymptotic self-similar turbulence state is an effective closure model development strategy. Here that approach is extended to compressible flows. As the focus of this work is shear dominated flows, the closure coefficients are determined by matching model fixed point behavior to DNS asymptotic Reynolds stress anisotropy values at various gradient Mach numbers. It is shown how this approach leads to reasonable agreement with the temporal evolution of compressible homogeneous shear DNS.

2.4.1 Incompressible flow

Detailed methodology for utilizing fixed point analysis for incompressible second-moment closure is given in Girimaji [27]. Here a brief synopsis is provided before extending it to compressible flows. From a given initial state parameterized by mean strain and rotation rate, kinetic energy and dissipation, a homogeneous turbulence field evolves toward an asymptotic state where appropriately normalized turbulence field variables approach an invariant state. In incompressible turbulence the key parameters that characterize the initial state of turbulence are normalized strain Sk/ε, and rotation $\Omega k/\varepsilon$ rates. The specific initial values of k, ε, and anisotropic state are less important. The normalized field variables that characterize the fixed point asymptotic state are anisotropy components b_{ij}, and production to dissipation ratio P/ε. This cause-effect relationship is used to determine the unknown coefficients in

the pressure-strain correlation closure. In other words, the closure model coefficients are chosen to yield the correct asymptotic state for a given initial strain/rotation tensor combination. In inhomogeneous unsteady calculations, mean strain and rotation rates change in time and space. The closure model temporally advances the computed solution toward the fixed point corresponding to the current strain and rotation rate tensors. As these tensors change in space and time, the evolution trajectory will change correspondingly. This approach has led to successful calibration of incompressible turbulence closure models [27, 83].

2.4.2 Extension to compressible flow

The fixed point calibration rationale should in principle also apply for compressible turbulence closure models. The main challenge is to identify novel parameters that characterize the initial state as well as additional fixed point characteristics appropriate for compressible turbulence. Beyond the incompressible turbulence parameters it is suggested that gradient Mach number and turbulent Mach number are the key new causal parameters that must be accounted for in modeling compressibility effects. The additional asymptotic state variable that characterizes the compressibility effect [71] is

$$X_\varepsilon = \frac{\overline{\rho}\varepsilon - \Pi}{\overline{\rho}P}. \tag{2.41}$$

This is the key compressible turbulence characteristic for the following reasons:

1. Π accounts for energy exchange between compressible and incompressible turbulence.

2. The stabilizing effect of compressibility also manifests via production, P.

3. The effect of compressibility on energy cascade rate is represented via ε.

	Causal parameters	Asymptotic state	Calibrated coefficients
Incompressible	Sk/ε, $\Omega k/\varepsilon$	b_{ij}, P/ε	C_1, C_3, C_4, C_5
Compressible	Sk/ε, $\Omega k/\varepsilon$, M_g, M_t	b_{ij}, P/ε, X_ε	C_1, C_3, C_4, C_5, C_P

Table 2.1: Causal parameters and effects for incompressible and compressible flows.

Furthermore, the modification to turbulence anisotropy is reflected in the variation of b_{ij} with Mach number. The choice of b_{ij}, P/ε, and X_ε as the asymptotic characteristics addresses all of the physical effects of relevance. In summary, the parameters (causes) of a compressible closure are normalized initial mean strain rate and rotation rate tensors, gradient Mach number, and turbulent Mach number. The asymptotic state variables of relevance (effects) are b_{ij}, P/ε, and X_ε. The causal parameters and effects in incompressible and compressible flows are shown in table 2.1.

The asymptotic states can be written in a general fashion [83] as

$$b_{ij_\infty} = f_{ij}\left(Sk/\varepsilon,\, \Omega k/\varepsilon,\, M_g,\, M_t\right), \tag{2.42}$$

$$\left(\frac{P}{\varepsilon}\right)_\infty = g\left(Sk/\varepsilon,\, \Omega k/\varepsilon,\, M_g,\, M_t\right), \tag{2.43}$$

and

$$X_{\varepsilon_\infty} = h\left(Sk/\varepsilon,\, \Omega k/\varepsilon,\, M_g,\, M_t\right), \tag{2.44}$$

where the subscript $(\cdot)_\infty$ refers to an asymptotic fixed point value. In the following section it is shown that for calibration purposes equations (2.42) – (2.44) can be rewritten as

$$b_{ij_\infty} = F_{ij}\left(C_1,\, C_3,\, C_4,\, C_5,\, C_P\right), \tag{2.45}$$

$$\left(\frac{P}{\varepsilon}\right)_\infty = G\left(C_{\varepsilon_1},\, C_{\varepsilon_2},\, C_P\right), \tag{2.46}$$

and

$$X_{\varepsilon_\infty} = H\left(C_{\varepsilon_1},\, C_{\varepsilon_2},\, C_P\right). \tag{2.47}$$

By determining the C_k coefficients in equations (2.45) – (2.47) in terms of the causal initial parameters in equations (2.42) – (2.44), the desired asymptotic states can be adequately reproduced.

2.4.3 Fixed point analysis for shear flows

In pure homogeneous shear the Reynolds stress, turbulent kinetic energy, and dissipation rate equations reduce to

$$\frac{d(\overline{\rho}R_{ij})}{dt} = \overline{\rho}P_{ij} - \frac{2}{3}\overline{\rho}\varepsilon\delta_{ij} + \Pi_{ij}, \tag{2.48}$$

$$\frac{d(\overline{\rho}k)}{dt} = \overline{\rho}P - \overline{\rho}\varepsilon + \Pi = \overline{\rho}P\left(1 - C_P\right) - \overline{\rho}\varepsilon, \tag{2.49}$$

and

$$\frac{d(\overline{\rho}\varepsilon)}{dt} = C_{\varepsilon_1}\overline{\rho}\frac{\varepsilon}{k}P\left(1 - C_P\right) - C_{\varepsilon_2}\overline{\rho}\frac{\varepsilon^2}{k}. \tag{2.50}$$

The velocity gradient tensor for homogeneous shear is

$$\frac{\partial\tilde{u}_i}{\partial x_j} = S\delta_{i1}\delta_{j2}, \tag{2.51}$$

and the modified rate of strain and rotation rate tensors are

$$S_{ij} = \begin{bmatrix} 0 & S/2 & 0 \\ S/2 & 0 & 0 \\ 0 & 0 & 0 \end{bmatrix}, \quad W_{ij} = \begin{bmatrix} 0 & S/2 & 0 \\ -S/2 & 0 & 0 \\ 0 & 0 & 0 \end{bmatrix}, \tag{2.52}$$

respectively.

The fixed points of the anisotropy tensor are given by

$$\frac{db_{ij}}{dt} \to 0. \tag{2.53}$$

Expressing equation (2.48) in terms of the anisotropy tensor yields

$$\overline{\rho}\frac{dR_{ij}}{dt} = 2\overline{\rho}\left[k\frac{db_{ij}}{dt} + \left(b_{ij} + \frac{1}{3}\delta_{ij}\right)\frac{dk}{dt}\right] = \overline{\rho}P_{ij} - \frac{2}{3}\overline{\rho}\varepsilon\delta_{ij} + \Pi_{ij}. \tag{2.54}$$

Inserting dk/dt from equation (2.49) and setting $db_{ij}/dt = 0$ leads to the following algebraic system for describing the asymptotic state

$$2\left(b_{ij} + \frac{1}{3}\delta_{ij}\right)\left[\frac{P}{\varepsilon}\left(1 - C_P\right) - 1\right] = \frac{P_{ij}}{\varepsilon} - \frac{2}{3}\delta_{ij} + \frac{\Pi_{ij}}{\overline{\rho}\varepsilon}. \tag{2.55}$$

Substitution of equations (2.51) and (2.52) into (2.15), (2.35), and finally into (2.55) yields the following system for the fixed points of the anisotropy tensor in pure homogeneous shear

$$\begin{aligned} 2\left(b_{11} + \frac{1}{3}\right)\left[\frac{P}{\varepsilon}\left(1 - C_P\right) - 1\right] =& \frac{-4Skb_{12}}{\varepsilon} - \frac{2}{3} + \frac{Sk}{\varepsilon}\left[-\frac{\varepsilon}{Sk}C_1 b_{11}\right. \\ &\left. + \frac{1}{3}C_4 b_{12} + C_5 b_{12} + 4C_P b_{12}\right], \end{aligned} \tag{2.56}$$

$$2\left(b_{22} + \frac{1}{3}\right)\left[\frac{P}{\varepsilon}\left(1 - C_P\right) - 1\right] = -\frac{2}{3} + \frac{Sk}{\varepsilon}\left[-\frac{\varepsilon}{Sk}C_1 b_{22} + \frac{1}{3}C_4 b_{12} - C_5 b_{12}\right], \tag{2.57}$$

$$\begin{aligned} 2b_{12}\left[\frac{P}{\varepsilon}\left(1 - C_P\right) - 1\right] =& \frac{-2Sk\left(b_{22} + 1/3\right)}{\varepsilon} + \frac{Sk}{\varepsilon}\left[-\frac{\varepsilon}{Sk}C_1 b_{12} + \frac{1}{2}C_3 + \frac{1}{2}C_4\left(b_{11} + b_{22}\right)\right. \\ &\left. + \frac{1}{2}C_5\left(b_{22} - b_{11}\right) + 2C_P\left(b_{22} + 1/3\right)\right]. \end{aligned} \tag{2.58}$$

The production to dissipation ratio

$$\frac{P}{\varepsilon} = \frac{-2Skb_{12}}{\varepsilon}, \tag{2.59}$$

is used to simplify equations (2.56) – (2.58) and determine the fixed points of the anisotropy tensor

$$b_{11_\infty} = \frac{(P/\varepsilon)_\infty (-1/12\, C_4 - 1/4\, C_5 - 2/3\, C_P + 2/3)}{(P/\varepsilon)_\infty (1 - C_P) + 1/2\, C_1 - 1}, \tag{2.60}$$

$$b_{22_\infty} = \frac{(P/\varepsilon)_\infty (-1/12\, C_4 + 1/4\, C_5 + 1/3\, C_P - 1/3)}{(P/\varepsilon)_\infty (1 - C_P) + 1/2\, C_1 - 1}, \tag{2.61}$$

$$b_{12_\infty} = -\left[\frac{b_{12}^*}{-24\left\{(P/\varepsilon)_\infty (1 - C_P) + 1/2\, C_1 - 1\right\}}\right]^{1/2}, \tag{2.62}$$

$$b_{12}^* = (P/\varepsilon)_\infty \left[3\, b_{11_\infty} (C_4 - C_5) + 3\, b_{22_\infty} (C_4 + C_5 + 4\, C_P - 4) + 3\, C_3 + 4\, C_P - 4\right]. \tag{2.63}$$

In the above the subscript $(\,\cdot\,)_\infty$ refers to an asymptotic fixed point value.

The final step is to determine the asymptotic value of the production to dissipation ratio. This ratio depends on the dissipation rate equation coefficients as well as the pressure-dilatation model. To test the effect of modifying the standard dissipation rate equation the two proposed models are calibrated separately: GG-I does not include the dissipation rate equation modification (equation (2.50) without the C_P term) and GG-II does include the modification. To find the fixed points of the production to dissipation ratio, the fixed points of the dimensionless shear rate Sk/ε are required.

$$\frac{d}{dt}\left(\frac{Sk}{\varepsilon}\right) = \frac{S}{\varepsilon}\frac{dk}{dt} - \frac{Sk}{\varepsilon^2}\frac{d\varepsilon}{dt} = 0. \tag{2.64}$$

Substituting for dk/dt and $d\varepsilon/dt$ the fixed point value of dimensionless shear for

GG-I is

$$\left(\frac{Sk}{\varepsilon}\right)_{\infty} = \frac{1}{-2b_{12_\infty}} \frac{(C_{\varepsilon_2} - 1)}{(C_{\varepsilon_1} - 1 + C_P)}. \tag{2.65}$$

Similarly, by using the GG-II dissipation rate equation the following is obtained

$$\left(\frac{Sk}{\varepsilon}\right)_{\infty} = \frac{1}{-2b_{12_\infty}} \frac{(C_{\varepsilon_2} - 1)}{(C_{\varepsilon_1} - 1)(1 - C_P)}. \tag{2.66}$$

Finally for GG-I the production to dissipation ratio can be written as

$$\left(\frac{P}{\varepsilon}\right)_{\infty} = \frac{C_{\varepsilon_2} - 1}{C_{\varepsilon_1} - 1 + C_P}, \tag{2.67}$$

and for GG-II

$$\left(\frac{P}{\varepsilon}\right)_{\infty} = \frac{C_{\varepsilon_2} - 1}{(C_{\varepsilon_1} - 1)(1 - C_P)}. \tag{2.68}$$

It is interesting to note that the asymptotic P/ε from both the traditional dissipation model equation (GG-I) and the spectral by-pass model equation (GG-II) exhibit dependence on the production blockage term C_P. In the GG-I model this is due to the direct effect of energy transfer from dilatational kinetic to internal form. This represents the physics that not all of the energy extracted from the mean flow by production resides in the kinetic form. A portion proportional to C_P is converted to internal energy. The GG-II model additionally incorporates the indirect effect of the kinetic-internal energy exchange on the spectral cascade and hence dissipation.

Following the incompressible SSG [83] dissipation rate evolution equation for both GG-I and GG-II the following equation is used

$$C_{\varepsilon_1} = 1.44, \quad C_{\varepsilon_2} = 1.83. \tag{2.69}$$

As mentioned in § 2.3.5, viscosity variation does not affect the dissipation evolution

significantly. The fixed points of the anisotropy tensor can now be calculated using equations (2.67) or (2.68) in equations (2.60) – (2.63). As expected, the fixed points of homogeneous shear depend exclusively on the closure model coefficients of the dissipation rate equation and pressure-strain correlation closure. The model coefficients are determined by requiring consistency between the model asymptotic behavior depicted in equations (2.60) – (2.63) and DNS results.

2.4.4 Model closure using DNS

The DNS of compressible homogeneous shear performed by Sarkar [71], provides full time history evolution of the anisotropy tensor b_{ij}, normalized dilatation X_ε, and normalized growth rates of turbulent kinetic energy Λ, for four cases of different initial gradient Mach number. Each simulation, characterized by the initial gradient Mach number, leads to a different set of asymptotic values for the five quantities of interest. The long time behavior of the five quantities b_{11}, b_{22}, b_{12}, X_ε and Λ is used to determine the five coefficients of the pressure-strain correlation C_1, C_3, C_4, C_5, and C_P based on the initial gradient Mach number of each DNS case. Sarkar's DNS spans the range $0.51 \leq M_{g_0} \leq 3.05$. The normalized quantities X_ε and Λ are defined as

$$X_\varepsilon = \frac{\overline{\rho}\varepsilon - \Pi}{\overline{\rho}P}, \quad \Lambda = \frac{1}{Sk}\frac{dk}{dt}. \tag{2.70}$$

The gradient Mach number in equation (2.40) differs slightly from that calculated by Sarkar due to a different lengthscale definition. Whereas Sarkar uses an integral lengthscale in the transverse shearing direction, in this work a large-eddy lengthscale is employed similar to the one used by Simone et al. [77] Nonetheless, as shown by Simone et al. [77], both gradient Mach number definitions appropriately characterize compressibility effects.

The GG-I and GG-II pressure-strain correlation coefficients are calibrated with

DNS at four non-zero gradient Mach numbers. To calibrate at the incompressible limit, i.e. $M_g = 0$, the equilibrium values found in the incompressible homogeneous shear experiments of Tavoularis & Corrsin [87] are used. Figure 2.6 shows the dependence of the model coefficients on gradient Mach number, where C_{i_0} are the incompressible model coefficients. A comparison of the incompressible coefficients with existing models is shown in table 2.2. The least squares curve fit functions and coefficients can be found in Appendix A. The calibration of the GG-I and GG-II compressible pressure-strain correlation models is now complete. It is interesting to note that the production blocking effect is significant only in the proximity of $M_g \approx 1$, which corresponds to Regime 2 of flow-pressure interactions. At higher M_g, the coefficients tend to very small values consistent with Regime 1 where the influence of pressure on turbulence is negligible. Thus, the present calibration methodology naturally yields physically consistent behavior.

Calibration for a broader range of compressible homogeneous flows with different mean flow gradients can be achieved in a similar fashion. Preliminary steps towards such a calibration applied to two dimensional incompressible turbulence is outlined in Mishra & Girimaji [55]. Accordingly, the coefficients would also be functions of mean flow gradient invariants. Cambon et al. [8] point out that compressibility effects may enhance turbulent kinetic energy for axial compression. Such behavior can be easily accommodated through increased P/ε by sensitizing C_P to mean flow gradient invariants. Here the focus is on shear dominated flows as reliable data of compressible homogeneous turbulence for other flows is currently unavailable.

2.4.5 Preliminary model assessment

The model development takes into account only the asymptotic state of Reynolds stress anisotropy. Such a model cannot guarantee correct transient behavior or the

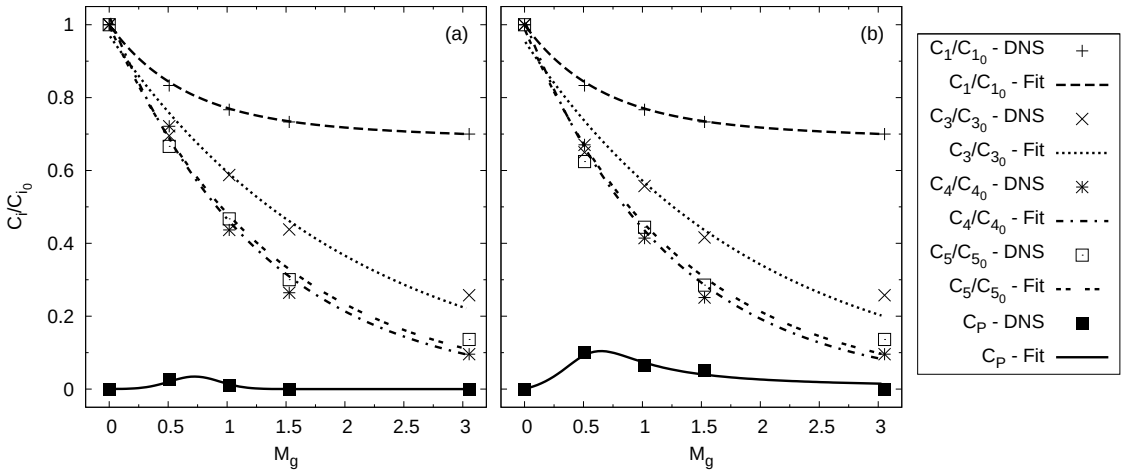

Figure 2.6: Calibrated coefficients for (a) GG-I, and (b) GG-II as functions of gradient Mach number. Symbols show best agreement with DNS [71], lines are least squares curve fits, given by equations (A.1)–(A.4) and table A.1.

C_{i_0}	SSG	SSG-S	LRR-IP	LRR	JM	GG-I	GG-II
C_{1_0}	3.4	3.4	3.6	3.0	3.0	3.0	3.0
$C^*_{1_0}$	1.8	1.8	—	—	—	—	—
C_{2_0}	4.2	4.2	—	—	—	—	—
C_{3_0}	0.8	0.8	0.8	0.8	0.82	0.82	0.82
$C^*_{3_0}$	1.3	1.3	—	—	—	—	—
C_{4_0}	1.25	1.25	1.2	1.75	1.59	1.59	1.59
C_{5_0}	0.4	0.4	1.2	1.31	1.09	1.12	1.12
C_{ε_1}	1.44	1.44	1.44	1.44	1.40	1.44	1.44
C_{ε_2}	1.83	1.90	1.90	1.90	1.90	1.83	1.83
α_1	—	0.5	—	—	—	—	—
α_2	—	0.15	—	—	—	—	—
α_3	—	0.2	—	—	—	—	—

Table 2.2: Pressure-strain correlation model coefficients.

prediction of other flow parameters in compressible homogeneous shear flow. Unlike the asymptotic behavior, the transient behavior is strongly dependent upon the initial wave-vector distribution and hence not unique. Nevertheless, a comparison between the model computations and DNS at the transient stages is made. The objective here is not a quantitative comparison, but to examine if the model captures the correct trends with increasing Mach numbers.

For this validation, equations (2.48) and (2.50) are numerically integrated using a fourth order Runge–Kutta–Fehlberg numerical scheme. The initial conditions match those found in Sarkar's DNS: isotropic Reynolds stresses, gradient Mach number, turbulent Mach number, and Sk/ε. Figures 2.7 – 2.10 show the results obtained for GG-I and GG-II respectively. It is clear that both models are able to capture the essential physical features seen in compressible homogeneous shear DNS. Specifically both models display the following characteristics as the initial gradient Mach number increases:

1. Increase in Reynolds stress anisotropy, figures 2.7(a) and 2.9(a).

2. Reduction of shear Reynolds stress and therefore production, figures 2.7(b) and 2.9(b).

3. Reduction of normalized growth rates of turbulent kinetic energy, figures 2.8(a) and 2.10(a).

4. Long time behavior of dilatational effects is insensitive to initial gradient Mach number, figures 2.8(b) and 2.10(b).

Using equations (2.67) and (2.68), the production to dissipation ratio at equilibrium for homogeneous shear is plotted in figure 2.11. The models display different behavior at intermediate M_g due to the exclusion (GG-I) or inclusion (GG-II) of the

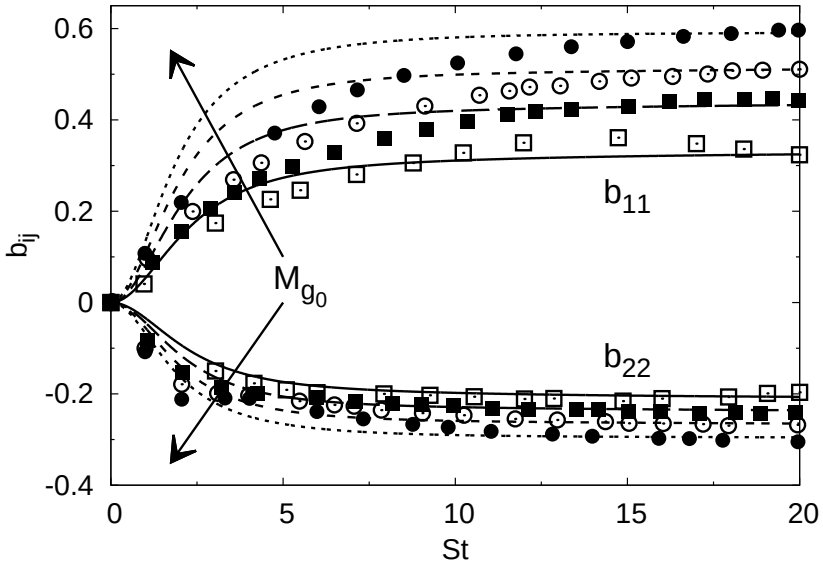

(a)

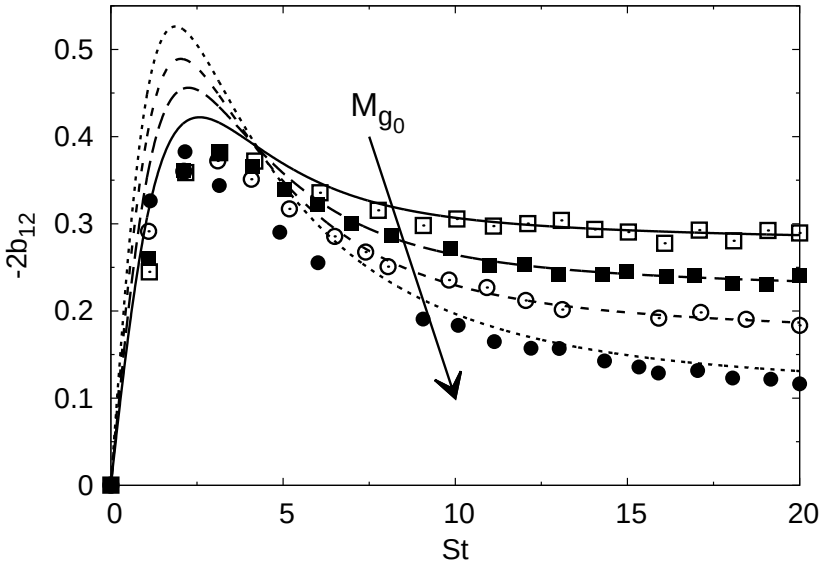

(b)

Figure 2.7: GG-I model preliminary validation with the compressible homogeneous shear DNS of Sarkar [71], arrows point towards increasing initial gradient Mach number. (a) b_{11} and b_{22}, and (b) b_{12}. For legend see following figure.

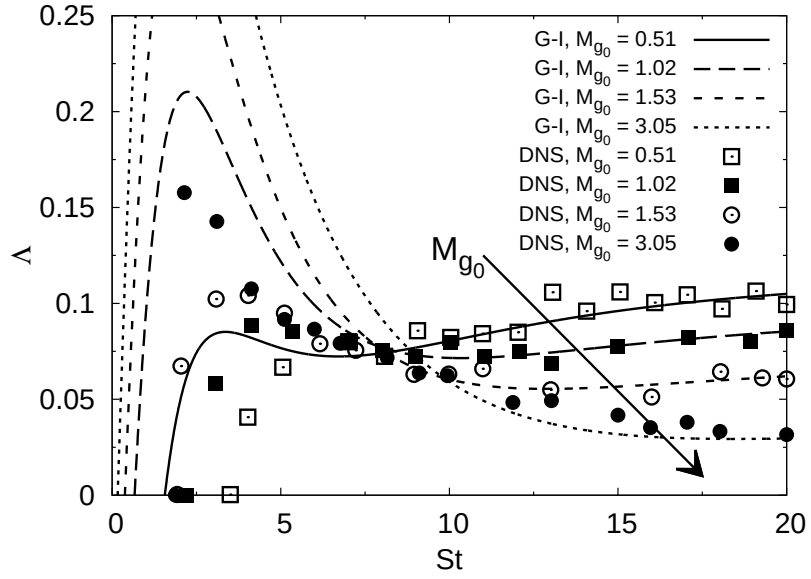

(a)

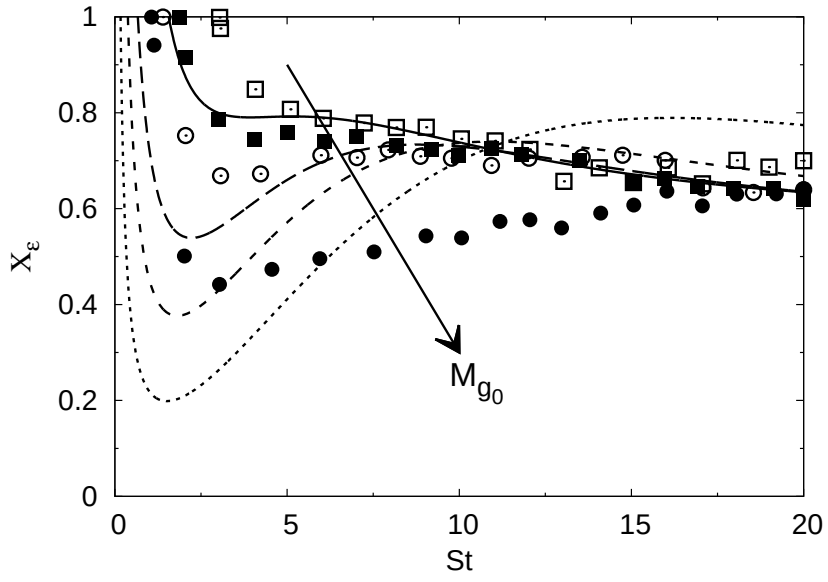

(b)

Figure 2.8: GG-I model preliminary validation with the compressible homogeneous shear DNS of Sarkar [71], arrows point towards increasing initial gradient Mach number. (a) Λ, and (b) X_ε.

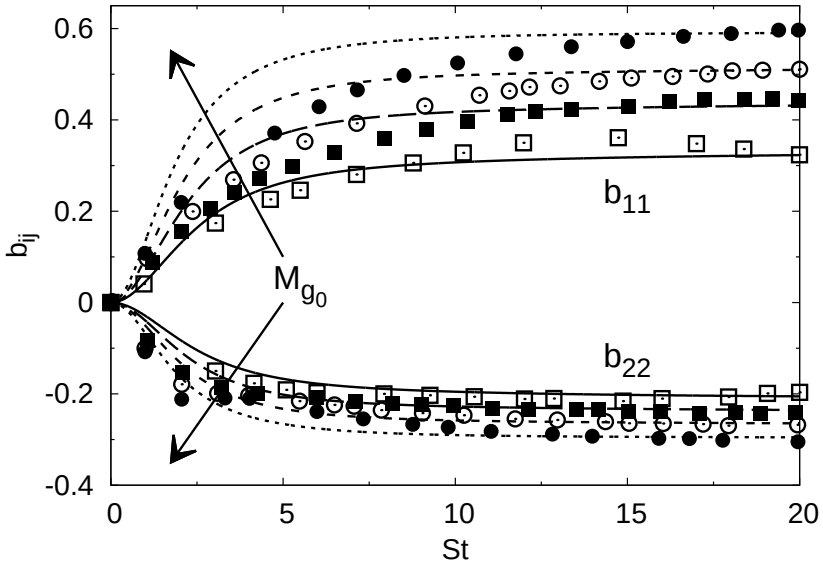

(a)

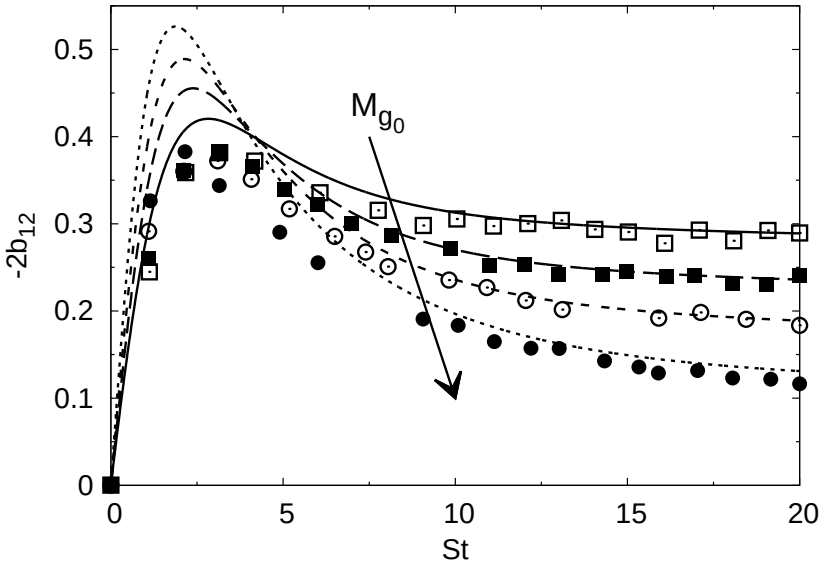

(b)

Figure 2.9: GG-II model preliminary validation with the compressible homogeneous shear DNS of Sarkar [71], arrows point towards increasing initial gradient Mach number. (a) b_{11} and b_{22}, and (b) b_{12}. For legend see following figure.

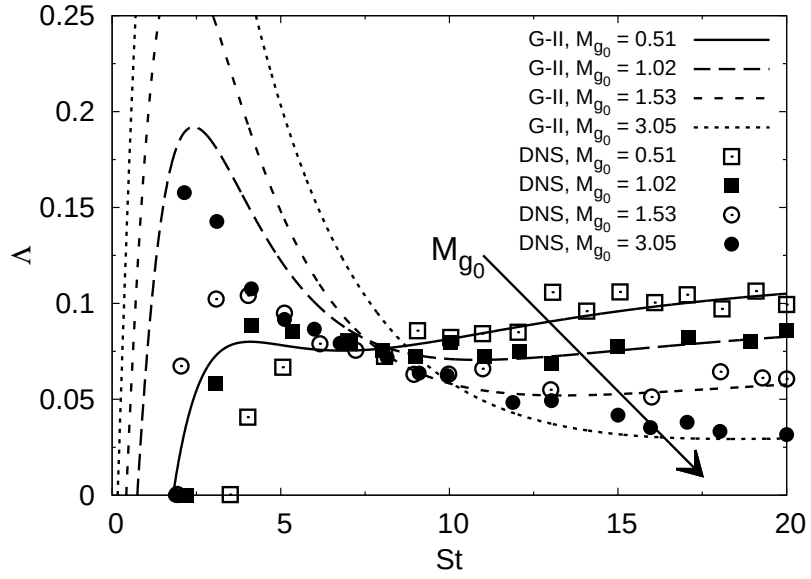

(a)

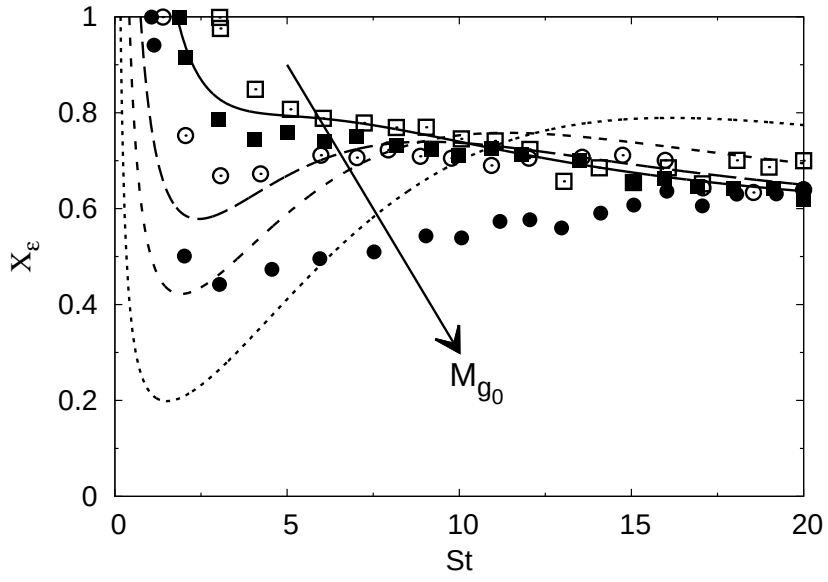

(b)

Figure 2.10: GG-II model preliminary validation with the compressible homogeneous shear DNS of Sarkar [71], arrows point towards increasing initial gradient Mach number. (a) Λ, and (b) X_ε.

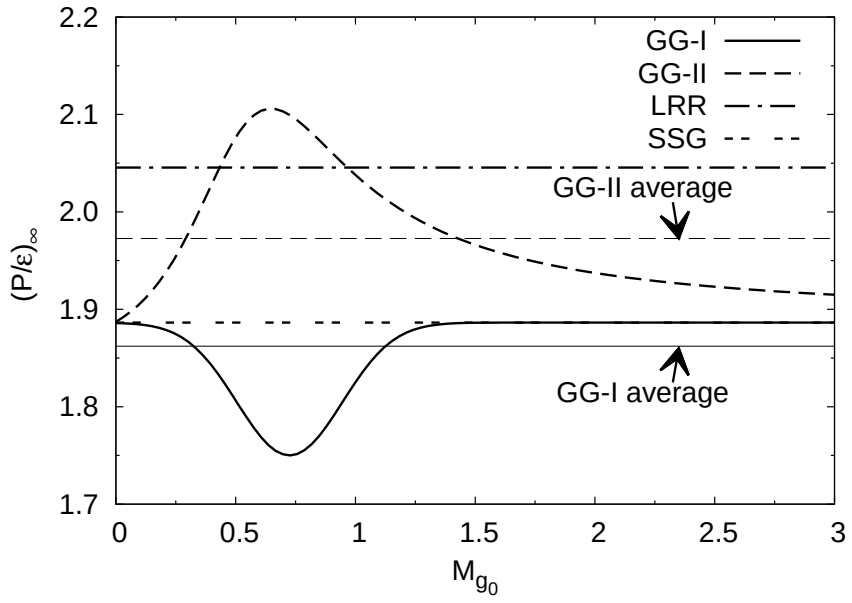

Figure 2.11: Production to dissipation ratios at equilibrium for homogeneous shear.

C_P term in the dissipation rate equation (2.39). For the range shown in figure 2.11 the average production to dissipation ratios are 1.86 and 1.97 for the GG-I and GG-II models respectively. These average values are not significantly different from the LRR [43] or SSG [83] equilibrium production to dissipation ratios for homogeneous shear, as seen in figure 2.11. Therefore the difference in P/ε ratio is not significant.

The present pressure-dilatation model is now compared with the one derived by Sarkar [70]. By performing an order of magnitude analysis of the fluctuating pressure equation, Sarkar obtained the following pressure-dilatation model

$$\Pi = 2\alpha_2 \overline{\rho} k M_t \frac{\partial \tilde{u}_m}{\partial x_n} b_{mn} + \alpha_3 \overline{\rho} \varepsilon M_t^2. \tag{2.71}$$

Some similarity between the present model, equation (2.36), and Sarkar model, equation (2.71), is clearly evident. However, the main difference lies in the trends as a function of Mach number. Whereas the Sarkar model suggests increasing energy

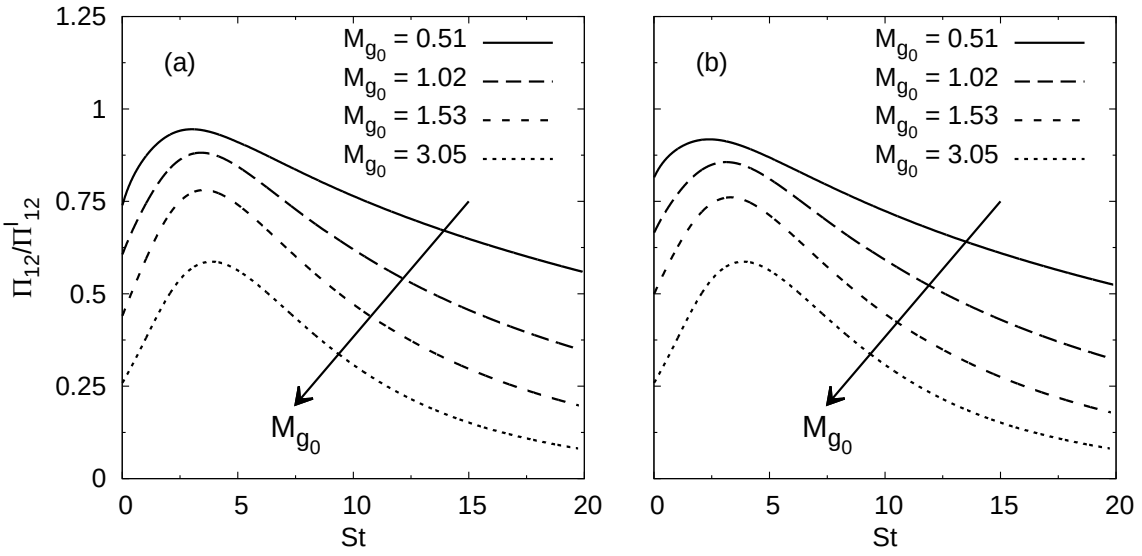

Figure 2.12: Evolution of compressible to incompressible pressure-strain correlation ratio for different initial gradient Mach numbers, (a) GG-I, (b) GG-II.

transfer from kinetic to internal form as M_t increases, the present model shows maximum transfer when acoustic and shear timescales are of the same order. For the present closure model at excessively high Mach numbers, the transfer vanishes, consistent with no flow-thermodynamic interactions in Regime 1.

Overall the compressible pressure-strain correlation models GG-I and GG-II possess three notable features. First, for low gradient Mach number, i.e. the incompressible limit, the model coefficients are very close to those of the Jones & Musonge [39] incompressible pressure-strain correlation model as seen in table 2.2. If desired, one may set $C_{3_0} = 0.8$ to satisfy the Crow constraint [13] without a significant impact on model performance. Second, as DNS [20,57] has shown, for very large gradient Mach number the effect of the pressure-strain correlation is diminished, as can be observed in figures 2.6 and 2.12. And third, the inclusion of the production blocking term suggested by RDT [5] allows the GG-I and GG-II models to capture the long time behavior of the normalized dilatational effects X_ε fairly well for the intermediate gra-

dient Mach number calibrations, as seen in figures 2.8(b) and 2.10(b). The models display consistency with RDT behavior at low, intermediate and high gradient Mach number. This attribute enables both GG-I and GG-II to capture a range of physics beyond the scope of calibration alone.

A final observation regarding figures 2.7 – 2.10 is in order to explain the lack of agreement between model and data at small St. There are two principal reasons. First, it is important to point out that a more accurate model representation of the interim behavior can be obtained if the acoustic lengthscale is employed in the gradient Mach number definition. However, as mentioned earlier, this lengthscale requires a separate closure model. The second reason is more critical. The main challenge of any pressure-strain correlation model is to determine the closure expression without any knowledge of the wave-number content of the flow and thermodynamic fields. Thus, by definition, pressure-strain correlation modeling in terms of only second-moments is an ill-posed problem. For example, two DNS calculations with the same Reynolds stress initial condition, but with different wave-number content can evolve quite differently. However, given the limitations of single-point closure, both flows will elicit the same closure model. Therefore, the models are derived based on a "seasoned" or "aged" wave-vector field. Any arbitrary initial condition will soon pass through transient stages and reach the seasoned state. Finally it approaches the asymptotic state via the seasoned state. As pointed out by Simone et al. [77], the initial conditions used in Sarkar's DNS were not properly aged to become representative of a "physical" turbulent field. Thus, no single-point closure model, lacking wave-vector information, can be expected to capture the transient behavior precisely. Furthermore, the behavior of GG-I and GG-II for small St shown in figures 2.7(b), 2.9(b), 2.8(a), and 2.10(a) agrees very well qualitatively with the DNS of Simone et al. [77] that employs more physically consistent initial conditions.

2.5 Model validation: high-speed mixing-layer

One of the biggest challenges in the development of a compressible pressure-strain correlation is the ability to capture the reduction of normalized supersonic mixing-layer growth rates observed experimentally by Papamoschou & Roshko [58], Goebel & Dutton [33], Clemens & Mungal [11], and many others [10,35,42,69]. In this section the results of incorporating compressible pressure-strain correlations GG-I and GG-II into the ANSYS® FLUENT Reynolds stress solver are presented. A description of the numerical implementation can be found in Appendix B. To compare with existing popular models, calculations are performed with the incompressible LRR [43], and compressible SSG-S [70, 83] models. The boundary conditions encountered in the experiments of Goebel & Dutton [33] are matched as closely as possible to compare similarity profiles, mixing-layer spreading rates and Reynolds stresses.

Three grids are studied to ensure grid insensitivity. The coarse grid consists of 24,000 cells (300 by 80), the medium grid 48,000 cells (400 by 120), and the fine grid 96,000 cells (600 by 160). Figures 2.13 and 2.14 show representative results from the grid study. The mean square error is plotted in figure 2.15 and is computed by using

$$MSE = \frac{1}{n}\sum_{i=1}^{n}\left(\tilde{u}_{1_i} - \tilde{u}^*_{1_i}\right)^2, \tag{2.72}$$

where $\tilde{u}^*_1$ is the streamwise velocity of the finest grid. It is concluded that the medium grid provides adequate resolution due to the negligible difference between the medium and fine grid results.

The experimental setup of a two dimensional mixing-layer consists of a channel with two incoming streams separated by a splitter plate. The top stream is labeled as “primary" and the lower as “secondary". It is customary to choose the primary stream as the high-speed inlet. For the computations we use a rectangular domain

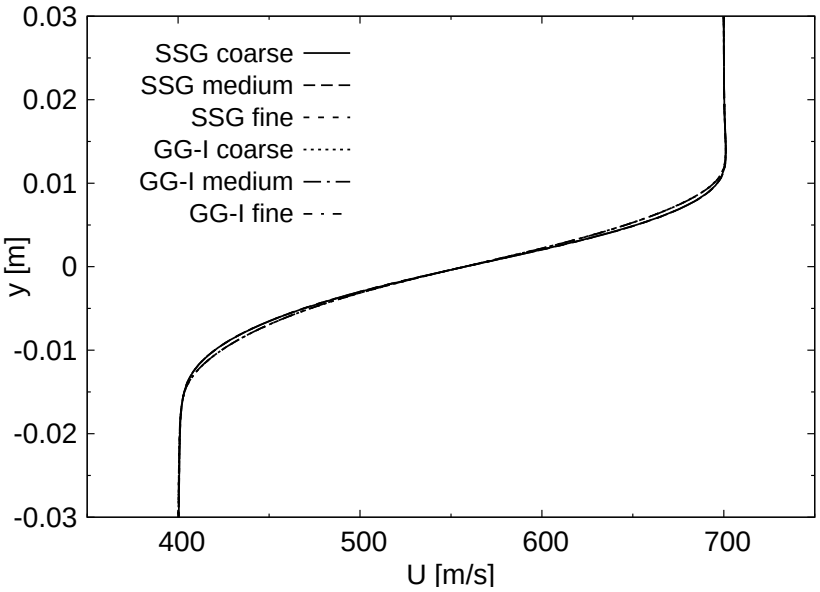

(a) Streamwise velocity profile.

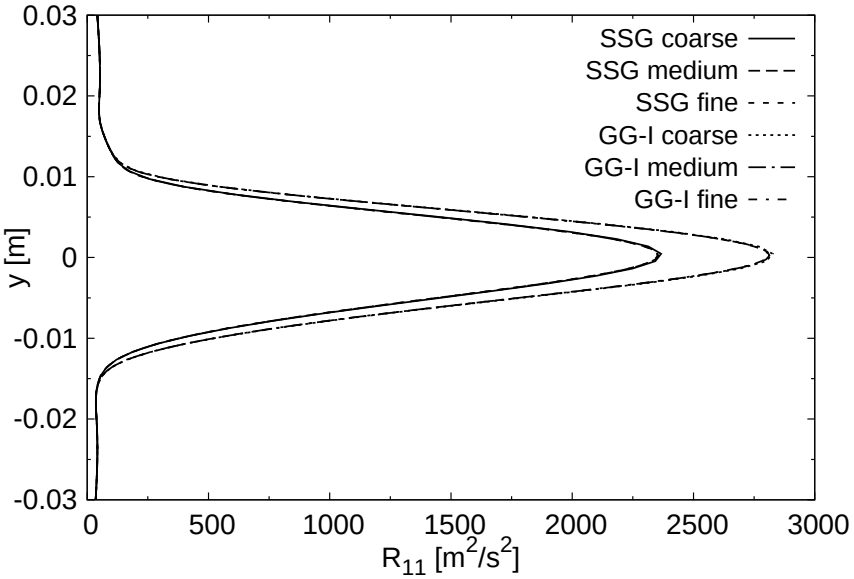

(b) Streamwise Reynolds stress.

Figure 2.13: RSM mixing-layer grid convergence study. (a) Streamwise velocity profile, and (b) streamwise Reynolds stress.

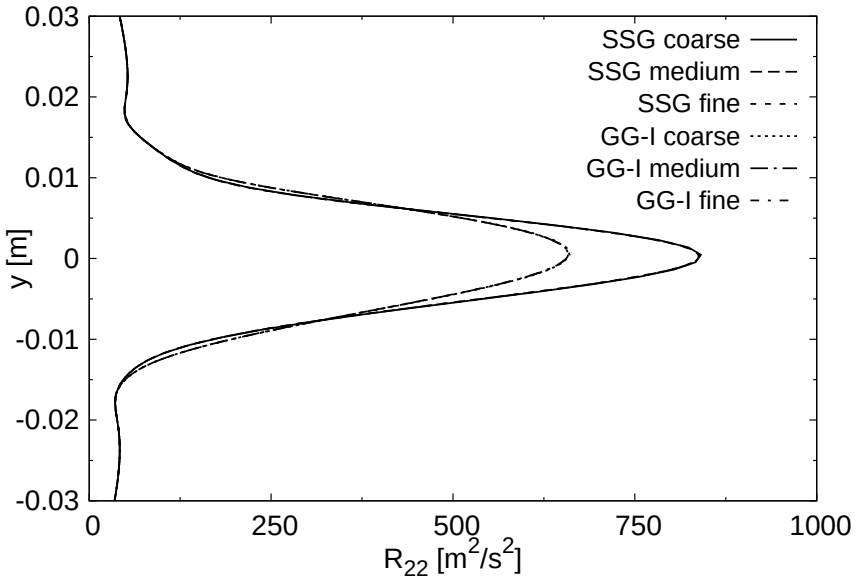

(a) Cross-stream Reynolds stress.

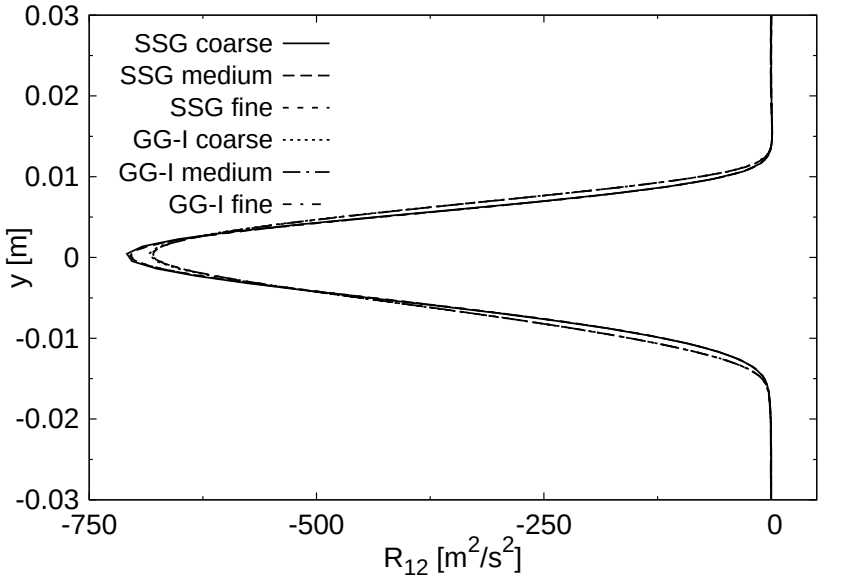

(b) Shear Reynolds stress.

Figure 2.14: RSM mixing-layer grid convergence study. (a) Cross-stream Reynolds stress, and (b) shear Reynolds stress.

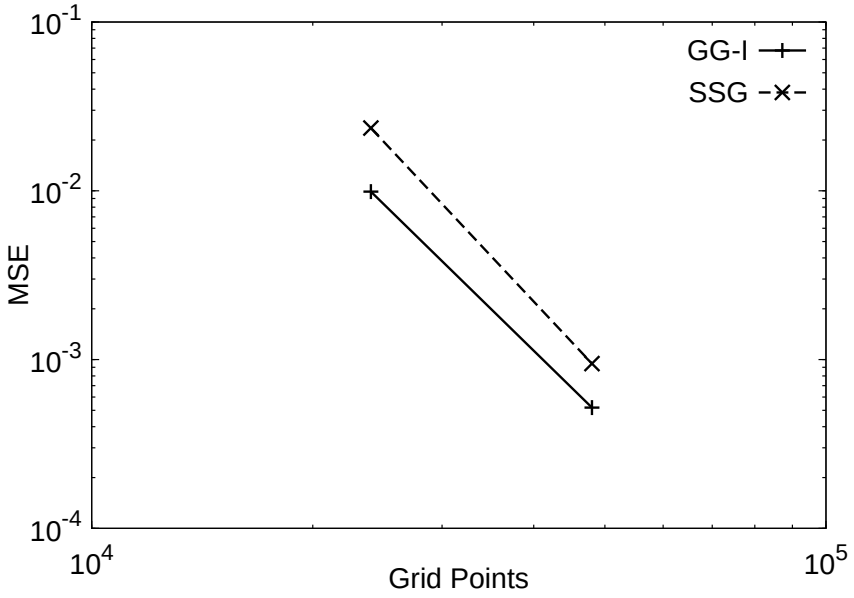

Figure 2.15: Mean square error of $\tilde{u}_1$ velocity.

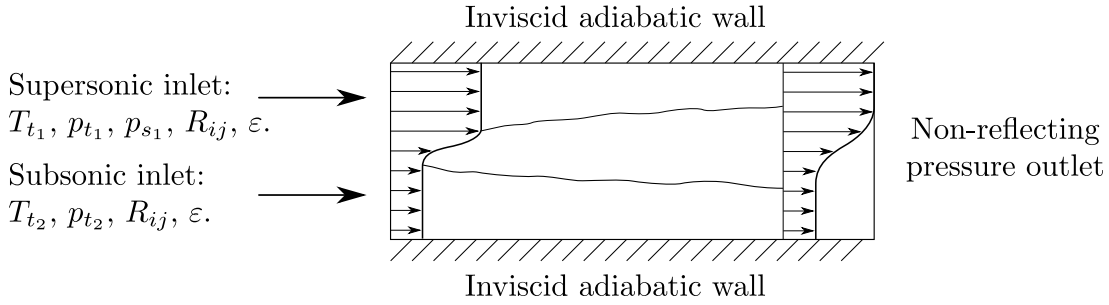

Figure 2.16: Two dimensional supersonic mixing-layer boundary conditions.

downstream of the splitter plate to avoid any near wall effects. A schematic of the computational domain along with the type of boundary conditions is shown in figure 2.16. The domain is 0.3 meters long in the streamwise direction and 0.1 meters high in the cross-stream direction. At the inlet, the Reynolds stress tensor is isotropic. Hyperbolic tangent and piecewise cubic polynomial functions are used to set the boundary conditions at the inlet to avoid sharp gradients and to expedite a fully developed self-similar flow. The flow becomes self-similar between 0.1 and 0.2 meters downstream of the inlet for all cases. Table 2.3 summarizes the inlet conditions.

Case	M_r	M_1	M_2	U_1	U_2	T_{t_1}	T_{t_2}	p_{t_1}	p_{t_2}	p_{s_1}
C1	0.40	2.01	1.38	515	404	295	295	365.6	142.3	46
C2	0.91	1.91	1.36	700	399	578	295	333.4	147.4	49
C3	1.37	1.96	0.27	499	92	285	285	389.7	55.8	53
C4	1.73	2.35	0.30	616	100	360	290	486.8	38.3	36
C5	1.97	2.27	0.38	830	131	675	300	381.8	35.4	32

Table 2.3: Supersonic mixing-layer inlet conditions. Dimensional quantities are in [m/s], [K], and [kPa] for velocity, temperature, and pressure respectively.

Goebel & Dutton [33] characterize the mixing-layer using relative Mach number defined as

$$M_r \equiv \frac{U_1 - U_2}{(a_1 + a_2)/2} = \frac{\Delta U}{\bar{a}}, \tag{2.73}$$

where the subscripts 1 and 2 refer to the primary and secondary streams respectively, U is the mean inlet velocity, and $\bar{a}$ is the average inlet speed of sound. Papamoschou & Roshko [58] observed that overall compressibility effects are found mainly between $0.5 \leq M_r \leq 2.0$. Goebel & Dutton's experiments span this range of M_r going from 0.4 to 1.97. Here results are presented for five of their cases: $M_r = 0.40, 0.91, 1.37, 1.73,$ and 1.97, which in the following are referred to as C1, C2, C3, C4, and C5 respectively.

Figures 2.17 – 2.26 compare similarity profiles $(U - U_2)/\Delta U$; normalized streamwise Reynolds stresses $\sigma_u/\Delta U$; normalized cross-stream Reynolds stresses $\sigma_v/\Delta U$; and normalized shear Reynolds stresses $R_{12}/(\Delta U)^2$ of RSM results against experimental data. All results are plotted in the self-similar region of the flow. In these plots b is the mixing-layer thickness defined as the transverse distance between locations where the mean streamwise velocity is $U_1 - 0.1\Delta U$ and $U_2 + 0.1\Delta U$. The y coordinate of the mixing-layer centerline is y_0. The standard deviations of the

	C1	C2	C3	C4	C5
Re_b (10^5)	0.8	1.5	4.4	3.5	2.8

Table 2.4: Reynolds number based on mixing-layer thickness at self-similar locations.

Reynolds stresses are defined as

$$\sigma_u = \sqrt{R_{11}}, \qquad \sigma_v = \sqrt{R_{22}}. \tag{2.74}$$

Table 2.4 shows a representative value for the Reynolds number at the self-similar locations where data is taken from the computations. This Reynolds number is based on velocity difference and mixing-layer thickness

$$Re_b = \frac{\overline{\rho}\Delta U b}{\overline{\mu}}. \tag{2.75}$$

2.5.1 Similarity profiles

Figures 2.17(a), 2.19(a), 2.21(a), 2.23(a), and 2.25(a) compare the similarity profiles obtained from each model against experimental data for the different Mach number cases. Although not shown here, multiple cross sections were plotted to ensure that the flows are fully self-similar. The experimental similarity profile is taken to be the error function curve fit that Goebel & Dutton found to be universal in all their cases. All models capture the self-similar profile for the five mixing-layer cases reasonably well.

2.5.2 Streamwise Reynolds stresses

Figures 2.17(b), 2.19(b), 2.21(b), 2.23(b), and 2.25(b) compare the normalized streamwise Reynolds stresses. For the lowest two relative Mach number cases, all models perform fairly well in matching the experimental data as seen in figures 2.17(b) and 2.19(b). However as the relative Mach number increases, the present models GG-I and GG-II show improvement in capturing the peak value of normalized streamwise Reynolds stress compared to the LRR and SSG-S models, as seen in figures 2.21(b) – 2.25(b).

2.5.3 Cross-stream Reynolds stresses

Figures 2.18(a), 2.20(a), 2.22(a), 2.24(a), 2.26(a) compare the normalized cross-stream Reynolds stresses. These figures show that the GG-I and GG-II models do a significantly better job of capturing the reduction of the cross-stream Reynolds stresses as the relative Mach number is increased. Figure 2.28(b) compares the Reynolds stress anisotropy σ_u/σ_v each model computes at different relative Mach numbers. Since an isotropic Reynolds stress tensor is used at the inlet for all simulations, the anisotropy found in the fully developed region is almost entirely due to the effect of the pressure-strain correlation. From figure 2.28(b) it is clear that whereas the GG-I and GG-II models are able to capture the trend of increasing anisotropy with increasing relative Mach number, both the LRR and SSG-S models predict almost constant values of anisotropy regardless of the relative Mach number of the mixing-layer.

2.5.4 Shear Reynolds stresses

Figures 2.18(b), 2.20(b), 2.22(b), 2.24(b), and 2.26(b) compare the normalized shear Reynolds stress. It is clear that the GG-I, GG-II, and SSG-S models predict the

reduction of the shear Reynolds stress as the relative Mach number increases fairly well, whereas the LRR model lacking compressibility corrections, does not. Being able to predict both the reduction of shear Reynolds stress as well as the increase in Reynolds stress anisotropy σ_u/σ_v is of paramount importance to capture the reduced spreading rates for compressible mixing-layers. Capturing only one of the two trends indicates that the physics is not well represented by the model. It may be useful to recall that in Regime 2, the Reynolds shear stress level diminishes due to pressure effects blocking production. This physics is incorporated into the present closure model.

2.5.5 Spreading rates

Figure 2.27 shows a compilation of experimental data [10, 11, 33, 35, 42, 58, 69] for normalized mixing-layer spreading rates as a function of relative Mach number. It can be immediately observed that there is a significant disparity among the experimental data. The Langley curve appears to mark an upper limit, while the experiments of Hall et al. [35] represent the lower limit. The experiments of Goebel & Dutton [33] fall in the middle of these two limits making their results a good data set for model validation. Figure 2.28(a) shows the normalized spreading rates of the RSM calculations, where the incompressible spreading rates are estimated [33, 58] as

$$\left(\frac{db}{dx}\right)_i = 0.0825\frac{\left(1-r\right)\left(1+s^{1/2}\right)}{1+rs^{1/2}}, \quad r=\frac{U_2}{U_1}, \quad s=\frac{\rho_2}{\rho_1}. \tag{2.76}$$

The LRR model does not include any compressibility corrections and therefore over-predicts the spreading rates for all five cases, although it does capture to a small degree the overall trend of reduced normalized spreading rates as the relative Mach number increases. The SSG-S model, which is specifically calibrated for compressible shear layers, does a reasonable job of approximating the experimental values, albeit

Case	LRR	SSG-S	GG-I	GG-II	Experimental
C1	0.026	0.022	0.023	0.023	0.020
C2	0.043	0.031	0.036	0.035	0.038
C3	0.110	0.071	0.059	0.056	0.059
C4	0.087	0.059	0.051	0.049	0.050
C5	0.118	0.068	0.048	0.049	0.049

Table 2.5: Mixing-layer spreading rates, db/dx.

by using a compressible dissipation model [72]. On the other hand, the GG-I and GG-II models do an excellent job of predicting the normalized spreading rates, while more closely capturing the experimental anisotropy of the Reynolds stresses. Table 2.5 shows the mixing-layer spreading rates for each model as well as the experimental values. The incompressible LRR model expectedly overpredicts the spreading rates, and the SSG-S model provides a reasonable first approximation averaging about a 20% error. The present compressible pressure-strain correlation models GG-I and GG-II are generally less than 10% in error with respect to the experimental spreading rates.

2.5.6 GG-I & GG-II model coefficient behavior

Figure 2.29 shows the variation of the normalized pressure-strain correlation coefficients inside the mixing-layer for both the quasi-incompressible case C1 and highly compressible case C5. Whereas the lower relative Mach number case displays only a minor deviation from incompressible behavior, case C5 shows how compressibility effects become dominant at higher relative Mach number. Figure 2.29 provides additional support for the selection of gradient Mach number as an appropriate parameter for characterizing compressibility effects.

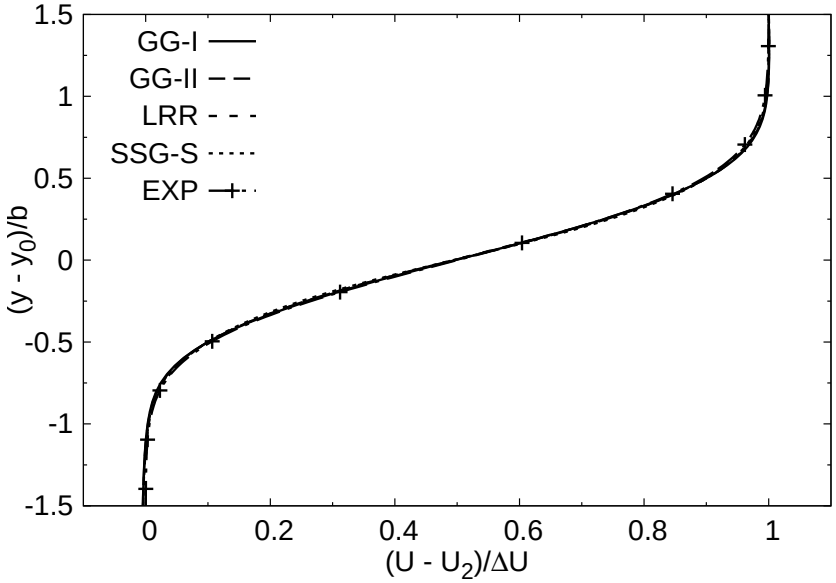

(a) Streamwise velocity similarity profile.

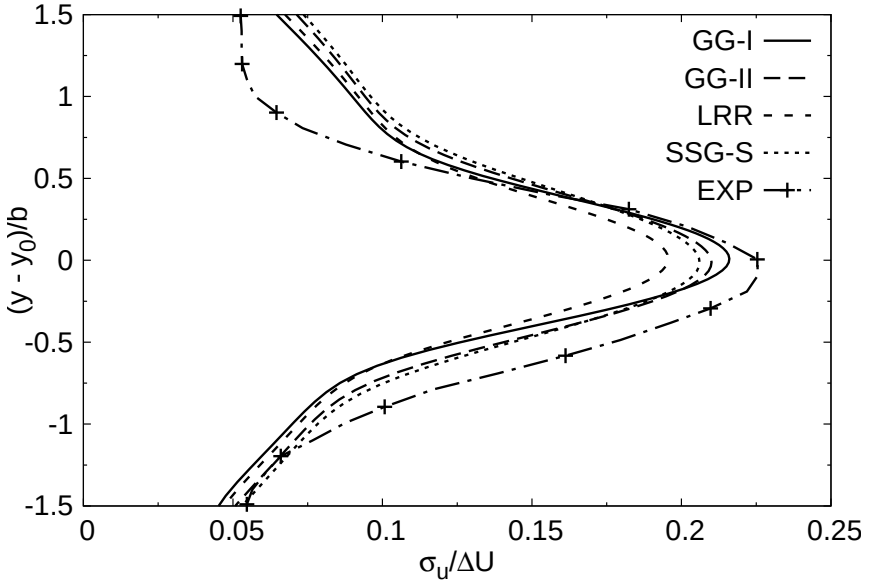

(b) Normalized streamwise Reynolds stress.

Figure 2.17: RSM mixing-layer results for C1, $M_r = 0.40$. (a) Normalized velocity profile, and (b) normalized streamwise Reynolds stress.

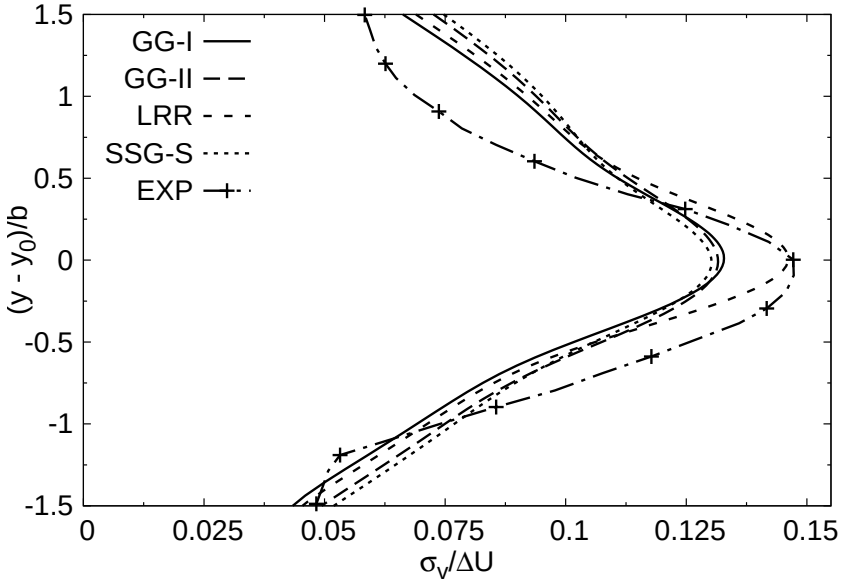

(a) Normalized cross-stream Reynolds stress.

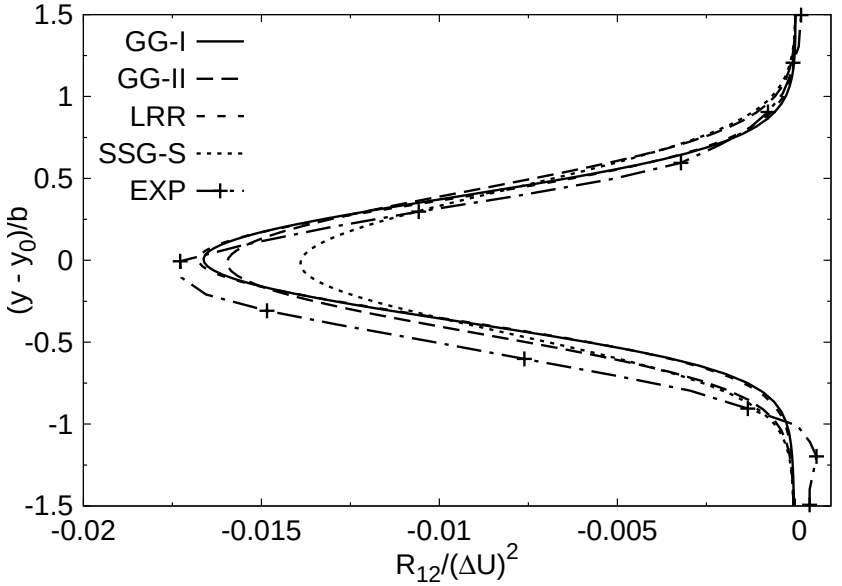

(b) Normalized shear Reynolds stress.

Figure 2.18: RSM mixing-layer results for C1, $M_r = 0.40$. (a) Normalized cross-stream Reynolds stress, and (b) normalized shear Reynolds stress.

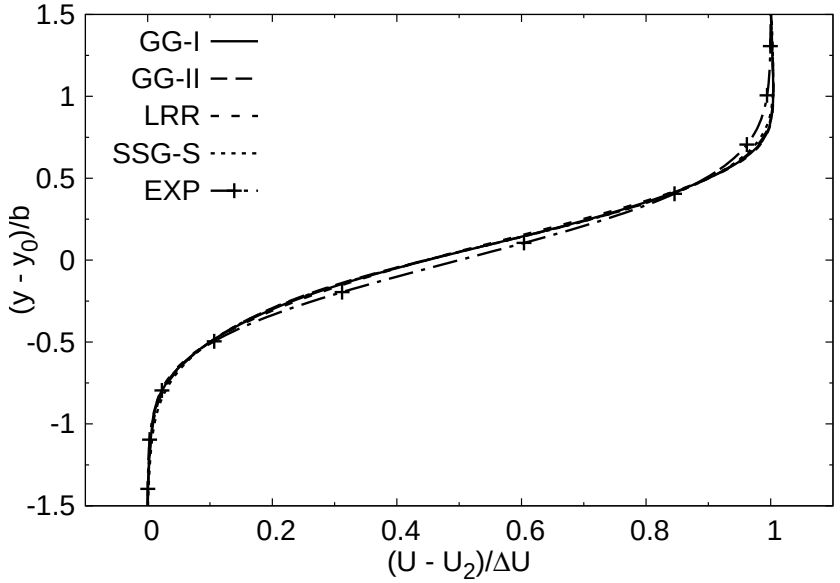

(a) Streamwise velocity similarity profile.

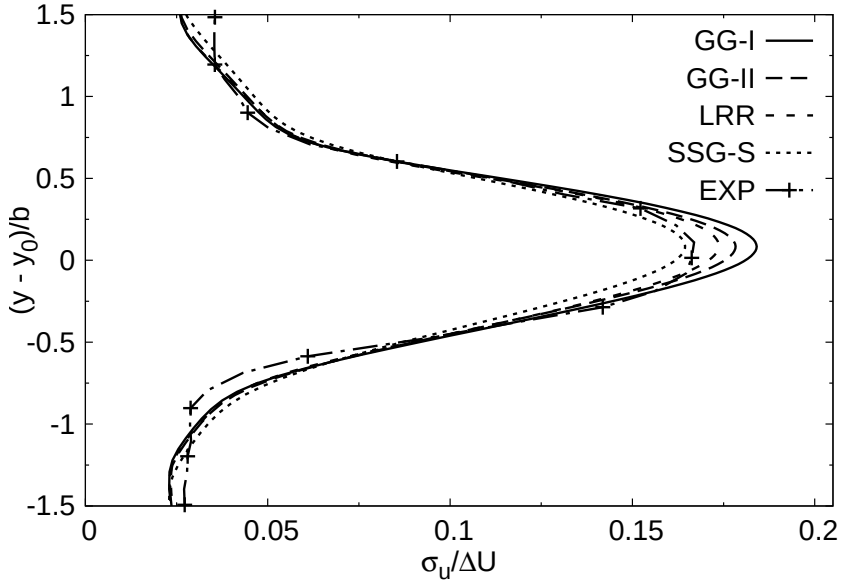

(b) Normalized streamwise Reynolds stress.

Figure 2.19: RSM mixing-layer results for C2, $M_r = 0.91$. (a) Normalized velocity profile, and (b) normalized streamwise Reynolds stress.

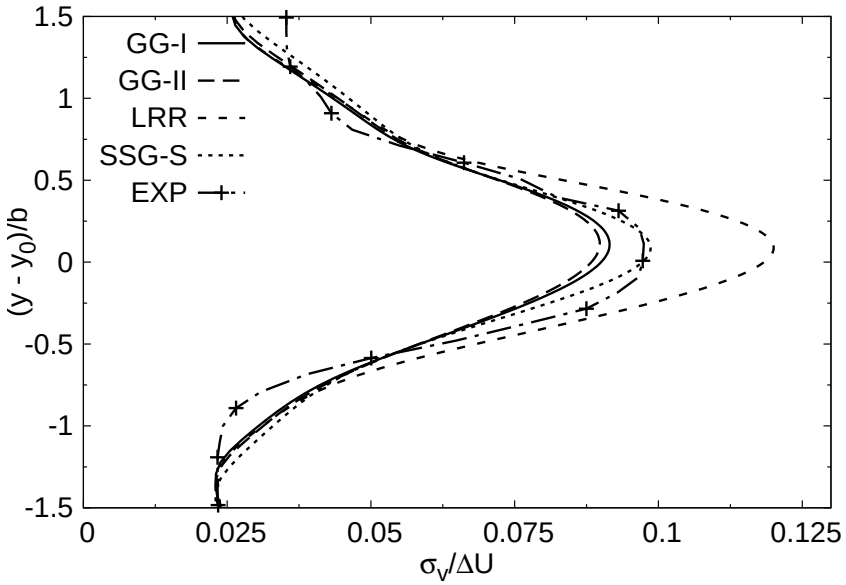

(a) Normalized cross-stream Reynolds stress.

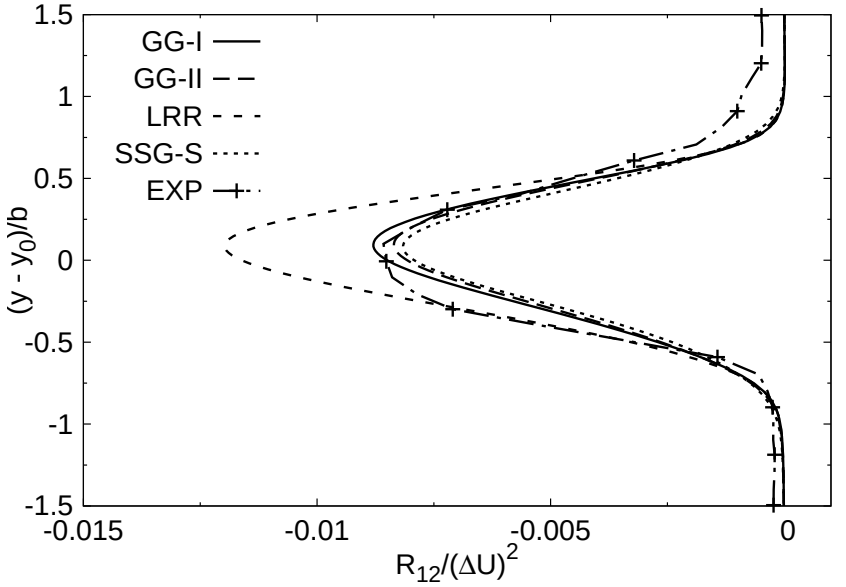

(b) Normalized shear Reynolds stress.

Figure 2.20: RSM mixing-layer results for C2, $M_r = 0.91$. (a) Normalized cross-stream Reynolds stress, and (b) normalized shear Reynolds stress.

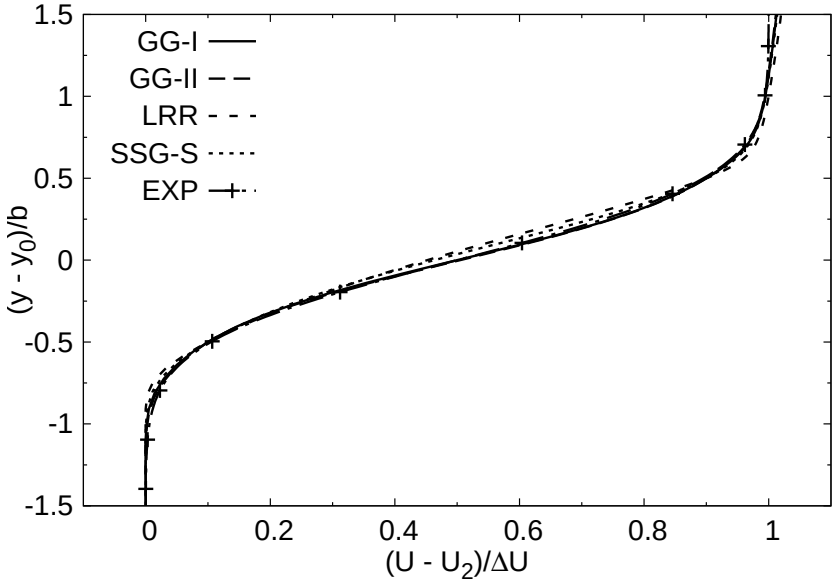

(a) Streamwise velocity similarity profile.

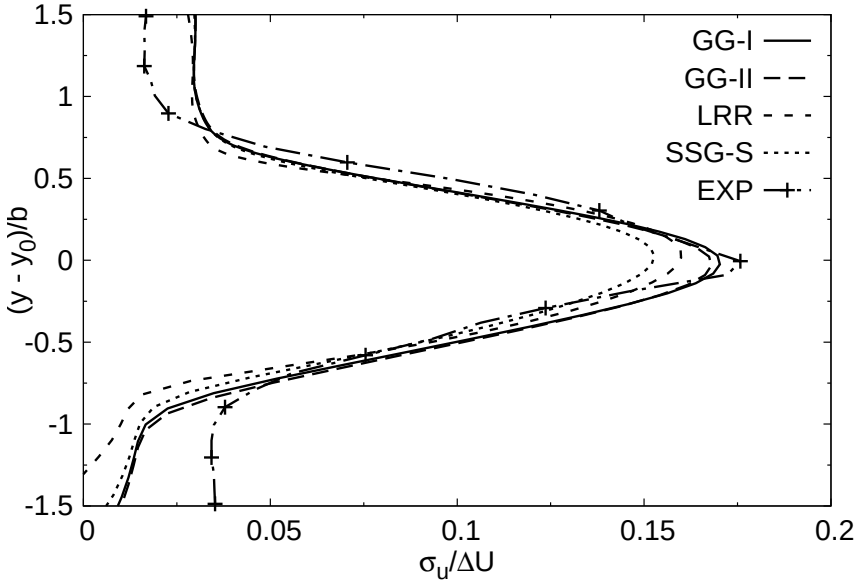

(b) Normalized streamwise Reynolds stress.

Figure 2.21: RSM mixing-layer results for C3, $M_r = 1.37$. (a) Normalized velocity profile, and (b) normalized streamwise Reynolds stress.

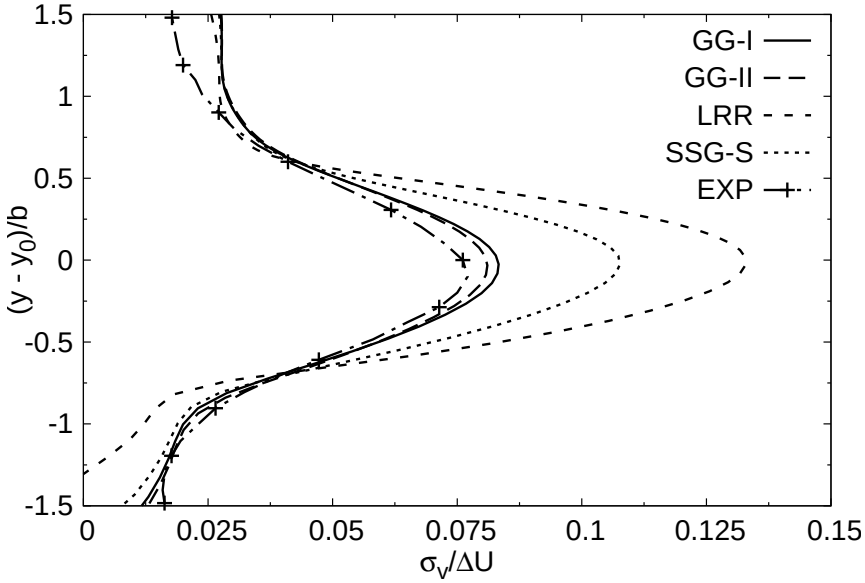

(a) Normalized cross-stream Reynolds stress.

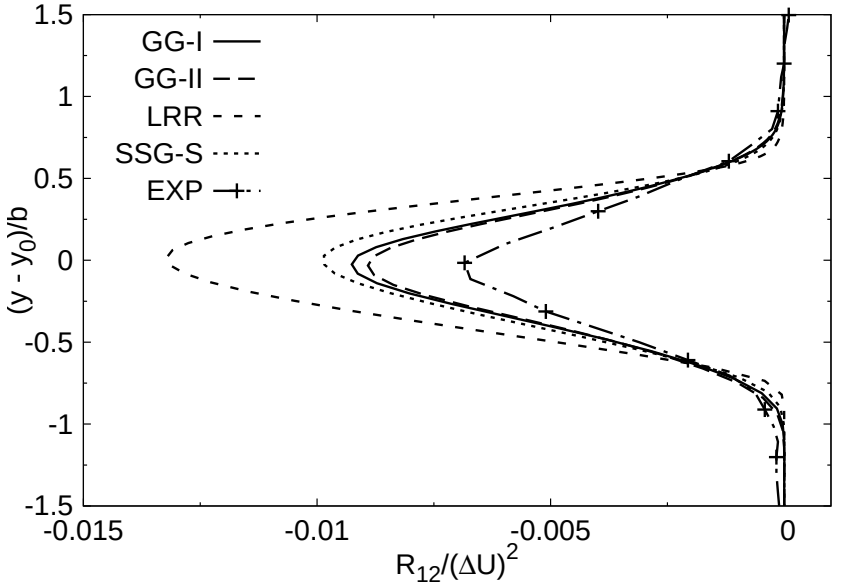

(b) Normalized shear Reynolds stress.

Figure 2.22: RSM mixing-layer results for C3, $M_r = 1.37$. (a) Normalized cross-stream Reynolds stress, and (b) normalized shear Reynolds stress.

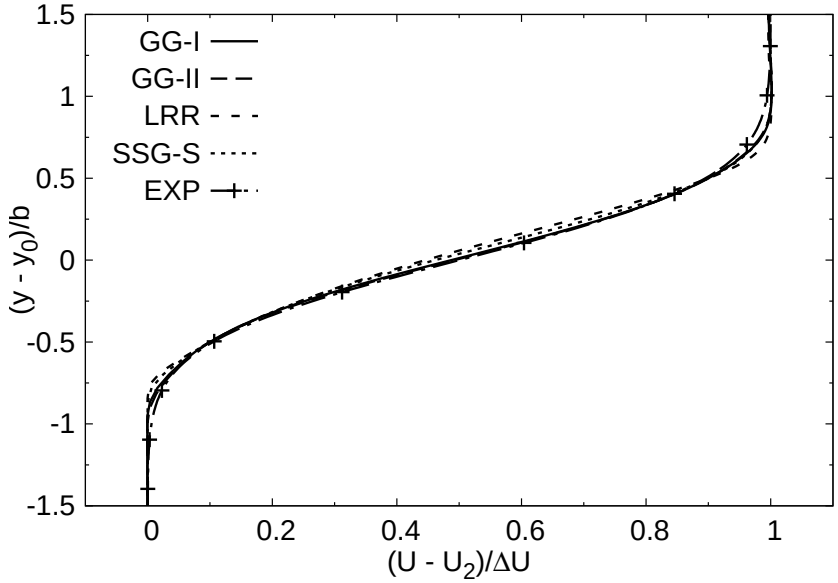

(a) Streamwise velocity similarity profile.

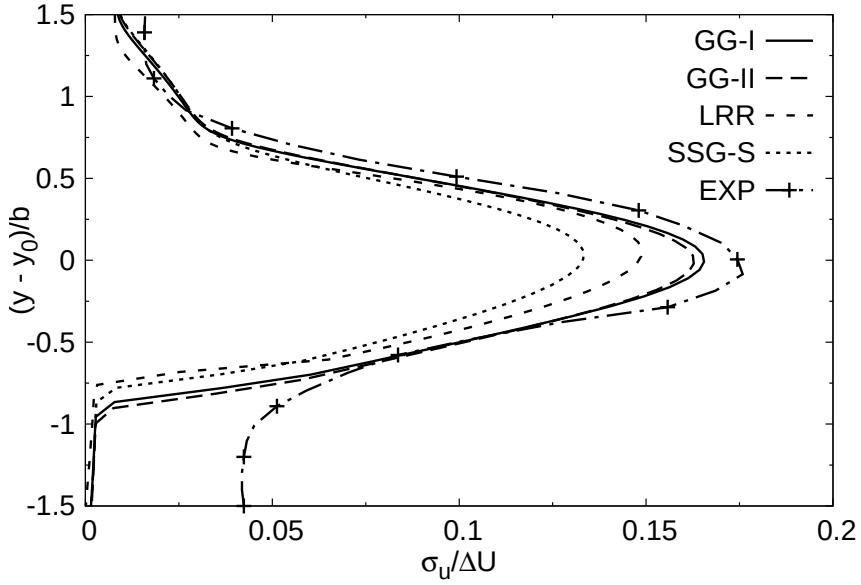

(b) Normalized streamwise Reynolds stress.

Figure 2.23: RSM mixing-layer results for C4, $M_r = 1.73$. (a) Normalized velocity profile, and (b) normalized streamwise Reynolds stress.

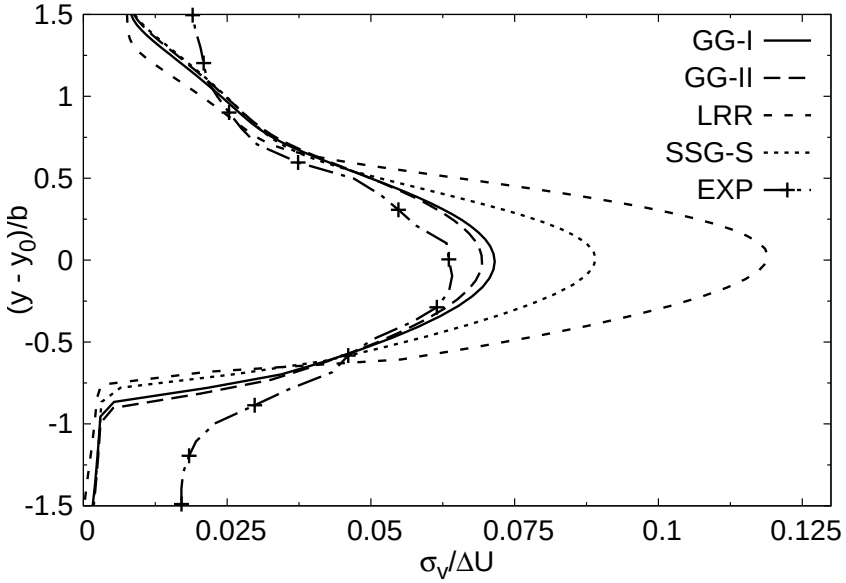

(a) Normalized cross-stream Reynolds stress.

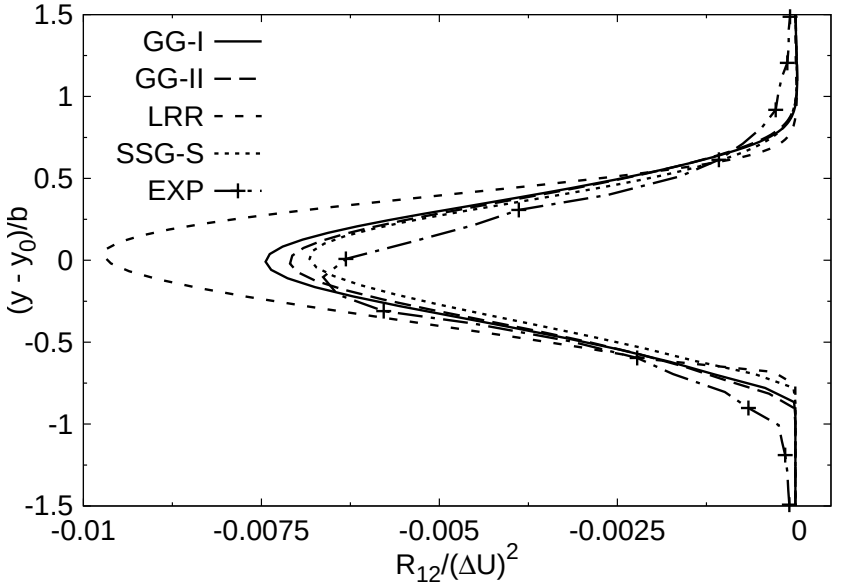

(b) Normalized shear Reynolds stress.

Figure 2.24: RSM mixing-layer results for C4, $M_r = 1.73$. (a) Normalized cross-stream Reynolds stress, and (b) normalized shear Reynolds stress.

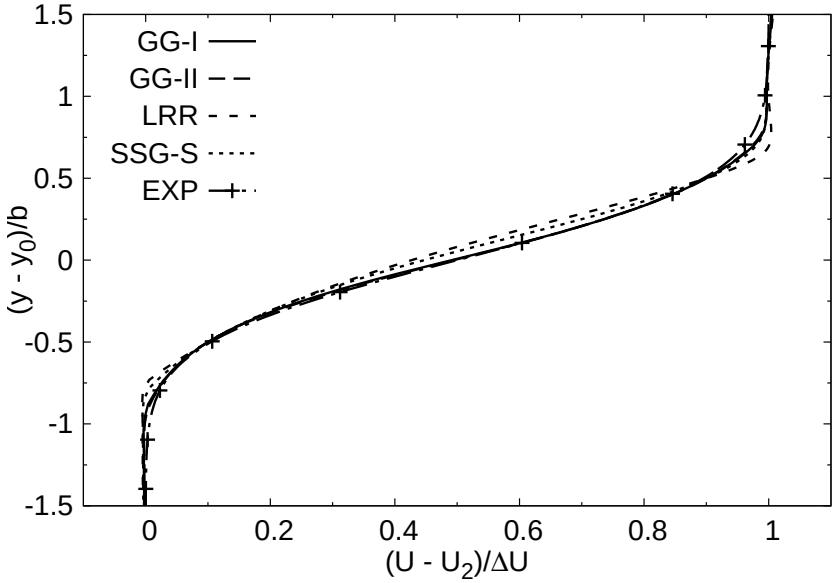

(a) Streamwise velocity similarity profile.

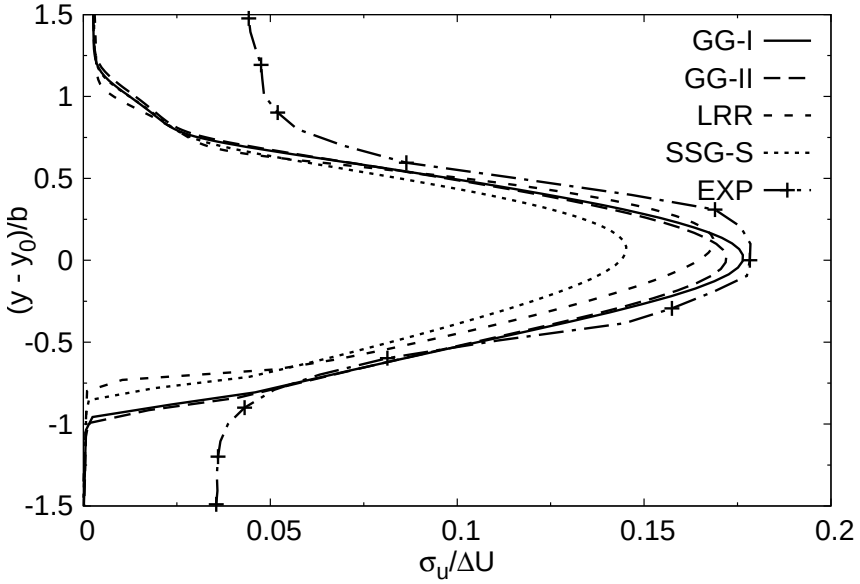

(b) Normalized streamwise Reynolds stress.

Figure 2.25: RSM mixing-layer results for C5, $M_r = 1.97$. (a) Normalized velocity profile, and (b) normalized streamwise Reynolds stress.

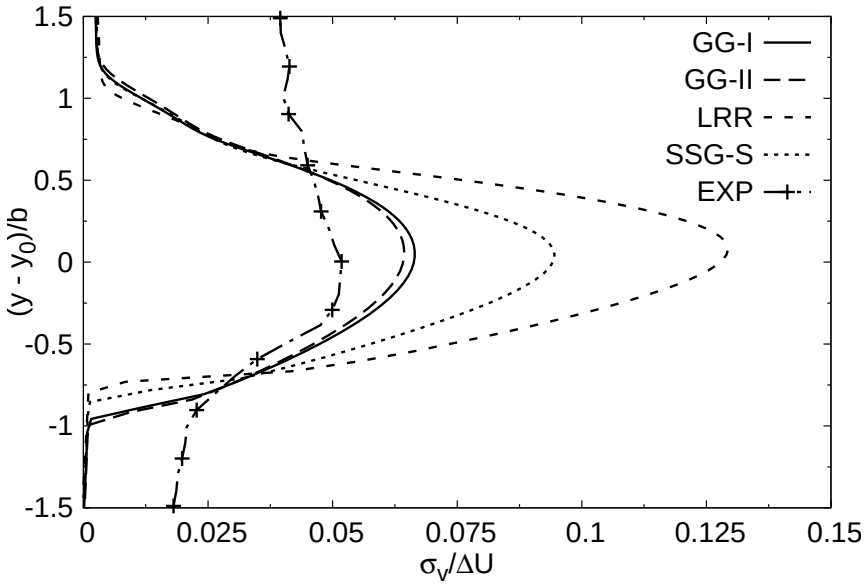

(a) Normalized cross-stream Reynolds stress.

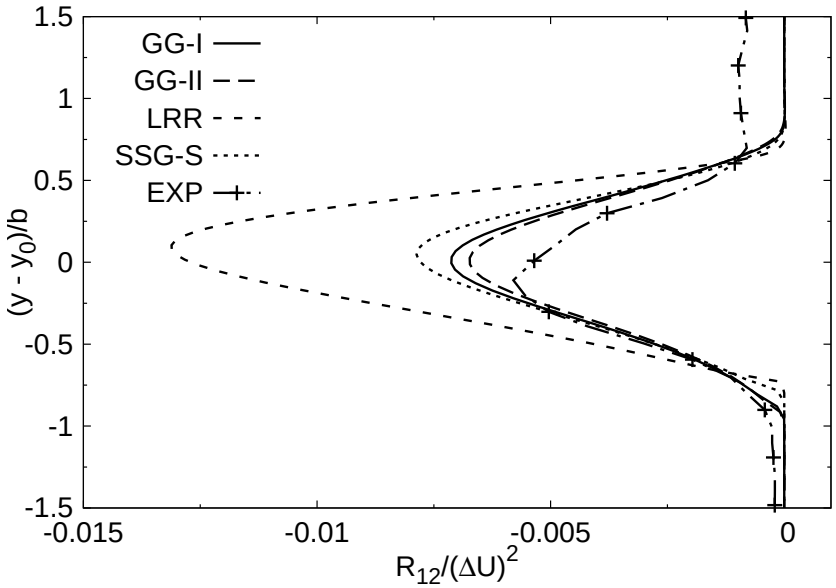

(b) Normalized shear Reynolds stress.

Figure 2.26: RSM mixing-layer results for C5, $M_r = 1.97$. (a) Normalized cross-stream Reynolds stress, and (b) normalized shear Reynolds stress.

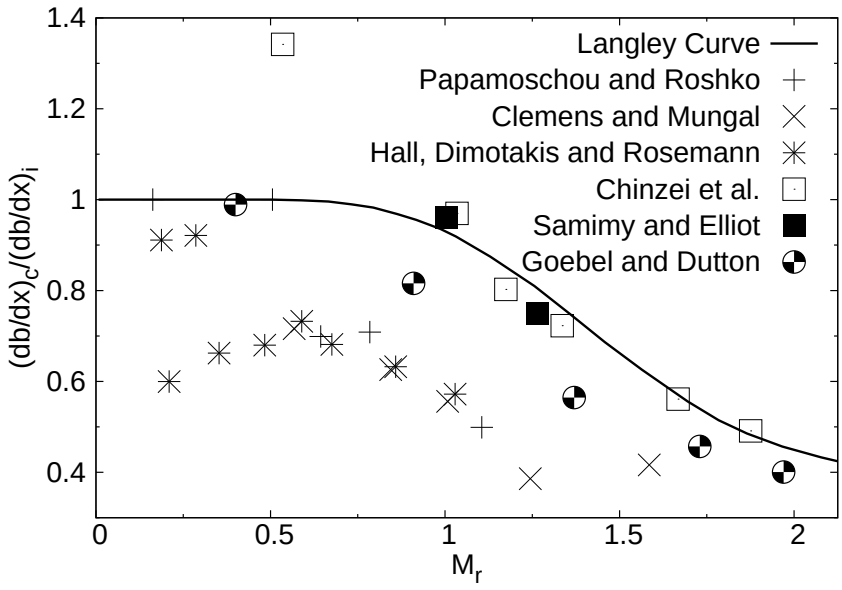

Figure 2.27: Normalized experimental spreading rates.

2.6 Conclusions

Flow stabilization, increased anisotropy, flow-thermodynamics and spectral cascade modification are some of the critical effects of compressibility on turbulence in high-speed flows. In this work, the development of a second-moment closure modeling framework in which all of the above effects can be accounted for is presented in a self-consistent manner. Progress in second-moment closures is of intrinsic utility, and central to advancements in low-order RANS and high-fidelity variable-resolution computational methods for turbulence. Working towards physics-based second-moment closures closures for pressure-strain correlation, pressure-dilatation and the consequent effects on the spectral cascade / lengthscale equation are presented. The physical foundation of the rapid pressure models is derived from RDT analysis which reveals a three-regime turbulence behavior that depends on gradient Mach number. The functional form of the closure model is taken to be a pragmatic incompressible model with added dilatational terms. For effective calibration

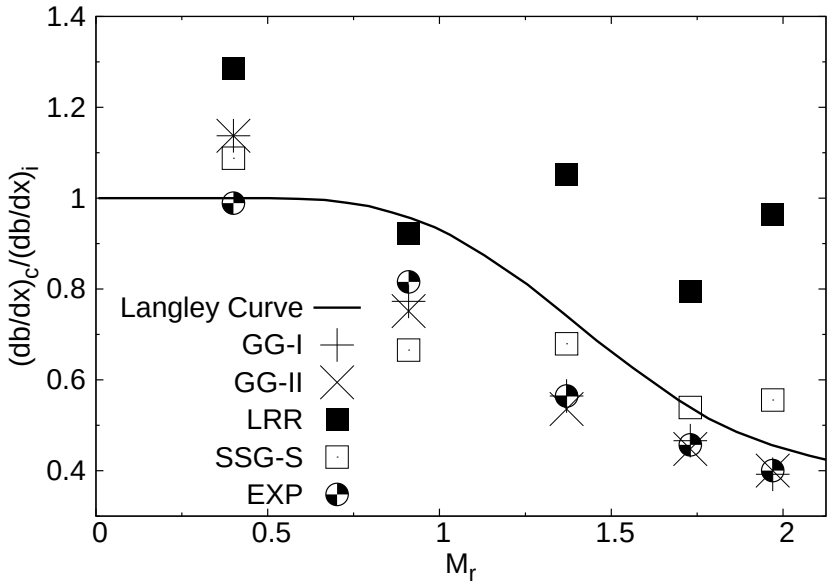

(a) Normalized spreading rates.

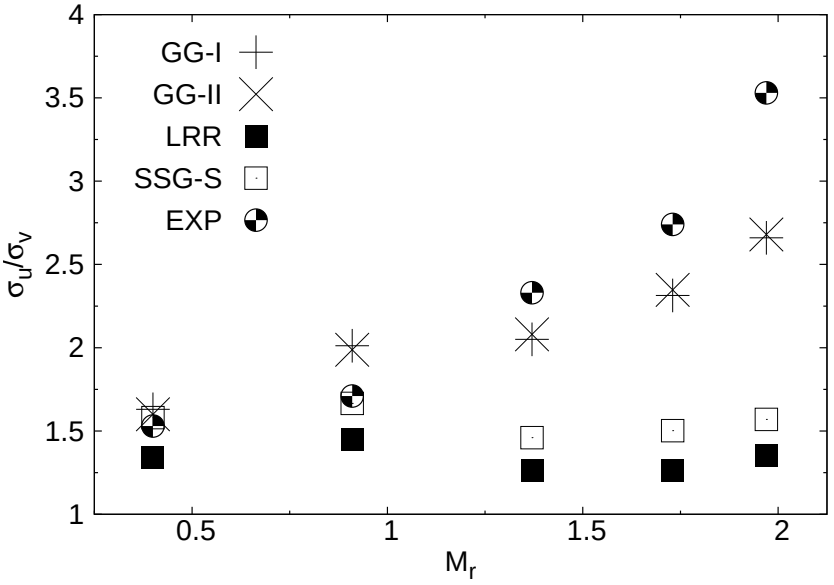

(b) Reynolds stress anisotropy.

Figure 2.28: RSM mixing-layer results. (a) Normalized spreading rates, and (b) Reynolds stress anisotropy.

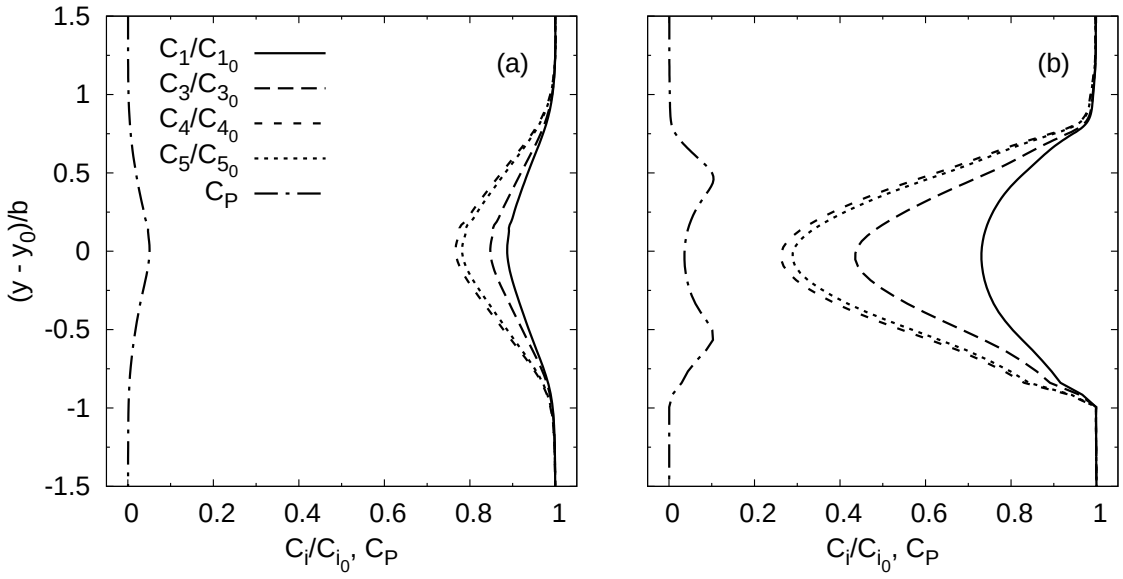

Figure 2.29: Normalized GG-II model coefficients for (a) C1, and (b) C5.

of the closure model coefficients, fixed point analysis is extended to compressible SMC models. The pressure-strain correlation closure coefficients are established by requiring consistency between model fixed point behavior and compressible homogeneous shear DNS data at self-similar asymptotic state. The closure coefficients are functions of gradient Mach number. The coefficients asymptote to very small values at high gradient Mach number indicating that pressure effects diminish at very high speeds. At low gradient Mach number, the coefficients tend to incompressible values. The pressure-dilatation model is obtained by simply taking the trace of the pressure-strain correlation closure expression. The dissipation equation is modified to account for the conversion of kinetic energy to internal energy by pressure-dilatation.

The model is validated against the high-speed mixing-layer data of Goebel & Dutton [33]. The main findings of the validation study are that as the relative Mach number of the mixing-layer increases, the new model can adequately capture: (i) increasing Reynolds stress anisotropy, (ii) decrease in Reynolds shear stress, and (iii) consequent reduction in compressible mixing-layer growth rates.

One of the important simplifications invoked in this work is the use of the turbulence integral lengthscale in the definition of gradient Mach number, instead of the more precise acoustic lengthscale. A possible future direction is a new evolution equation for acoustic lengthscale. Indeed, this could be critically important for accurate compressible shear flow computations.

3. ALGEBRAIC REYNOLDS STRESS MODEL (ARSM) FOR COMPRESSIBLE SHEAR FLOWS

3.1 Introduction

The design and development of aerodynamic and propulsion components of hypersonic flight vehicles relies heavily on computational tools as ground-based experimental facilities cannot adequately replicate flight conditions. Development of computational tools for hypersonic turbulent flows presents challenges not encountered in lower speed regimes. One of the major challenges is the inadequate understanding of compressible turbulence flow physics leading to the need for accurate and computationally viable closure models. The most important difference between low and high-speed regimes is the change in the action of pressure. In low speed flows, the role of pressure is merely to impose the incompressibility constraint and is completely governed by a Poisson equation. With increase in Mach number, pressure assumes its role as a thermodynamic state variable and its evolution is governed by energy balance and state equations which must be satisfied in addition to mass and momentum conservation requirements. One of the most prominent effects of compressibility in high-speed flows is its stabilizing influence on turbulence. In a propulsion device reduced turbulence levels can be highly detrimental as they reduce the rate at which fuel and oxidizer mix. Figure 3.1 shows a compilation of experimental data [10, 11, 33, 35, 42, 58, 69] of normalized mixing-layer spreading rate as a function of relative Mach number: the so-called Langley [42] curve. At low relative Mach number, compressible mixing-layer spreading rates are close to the incompressible values. However, with increasing relative Mach number the spreading rate diminishes substantially. For over the past two decades, turbulence researchers have

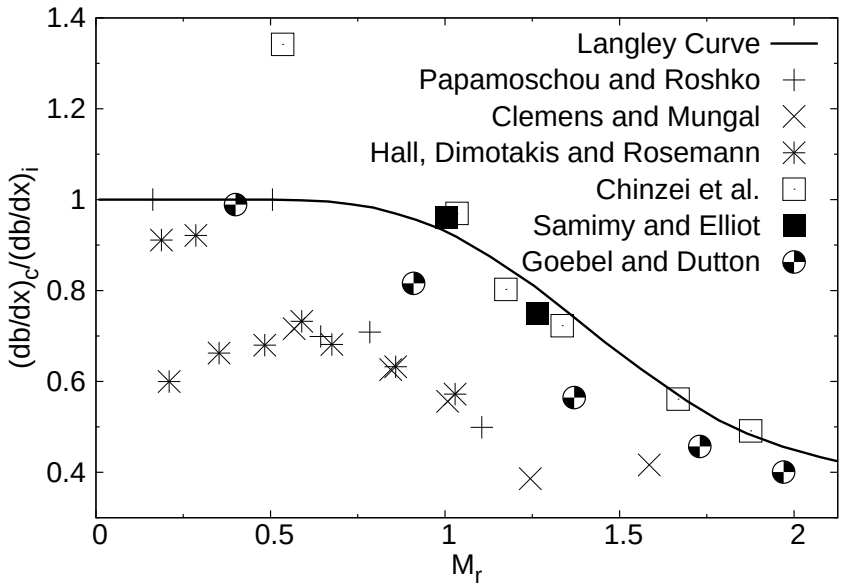

Figure 3.1: Compilation of normalized mixing-layer spreading rates.

sought closure models that can accurately capture the Langley [42] curve behavior along with the underlying flow physics.

3.1.1 Relevant previous investigations

One of the earliest works on closure modeling addressing the stabilization of high-speed mixing-layers is the work of Sarkar et al. [72]. Therein it was suggested that compressibility effects may manifest themselves *via* dilatational dissipation. Sarkar et al. [72] proposed a closure model dependent on turbulent Mach number, $M_t \equiv \sqrt{2k}/a$, where k is the turbulent kinetic energy, and a is the speed of sound. More recently, Aupoix [3] proposed a lengthscale modification to obtain a reduction in mixing-layer spreading rates. However, direct numerical simulation (DNS) studies [20,57,71] have shown that the largest contribution toward the growth inhibition of mixing-layers comes from the pressure-strain correlation which scrambles the streamwise and stream-normal fluctuations leading to a low turbulent shear stress and decreased production. Several subsequent works such as those by Fuji-

wara et al. [21], Pantano & Sarkar [57], Park & Park [59], Huang & Fu [37], and most recently Kim & Park [41] have contributed toward improved pressure-strain correlation models in compressible turbulent flows. While these models have yielded some plausible results such as reduction in mixing-layer thickness, concomitant effects pertaining to increase in anisotropy or the exchange of energy between kinetic and potential (thermodynamic) forms are not consistently explained. Thus previous closures in literature need further enhancement before they can be considered complete. Recently a pressure-strain correlation model has been developed [34] that is consistent with all the above compressibility effects observed in rapid distortion theory (RDT) [5, 44, 45], and direct numerical simulations [71]. This pressure-strain correlation model has been derived from a unified framework that takes into account the following compressibility effects: stabilization and anisotropy, kinetic-potential energy transfer due to pressure-dilatation, and corrections to the spectral cascade (dissipation rate). The objective of this work is to develop an algebraic model that captures fundamental compressibility effects by employing a physically consistent compressible pressure-strain correlation model [34].

3.1.2 Algebraic Reynolds stress modeling

Among the Reynolds averaged Navier–Stokes (RANS) closure options, the seven-equation Reynolds stress closure model (RSCM) offers the highest degree of fidelity but at the highest computational cost. The standard Boussinesq approximation based two-equation models are the preferred choice for practical flows due to considerable computational simplicity. Algebraic Reynolds stress models (ARSM) attempt to incorporate the improved physics of RSCM at the computational expense of two-equation models. The ARSM closure employs a nonlinear constitutive relation and is derived from a parent RSCM invoking the weak-equilibrium assump-

Name	CPU Expense	Physical Fidelity	Limitations / Challenges
RSCM	Highest	Highest	Expensive to compute
Non-linear ARSM	Moderate	High	Numerical stiffness
Linear ARSM	Low	Moderate	Non-linear effects absent
Boussinesq	Lowest	Low	Unphysical / unrealizable

Table 3.1: Hierarchy of common RANS closures.

tion [23, 25, 61, 89]. The linear ARSM approach employs only the linear term present in the full ARSM. Although similar to the standard Boussinesq approximation in computational effort, linear ARSM has several positive attributes as viscosity coefficient (C_μ) can vary according to flow physics. Table 3.1 shows the hierarchy of common RANS closures with the limitations of each approach. It is important to note that the weak-equilibrium assumption is implicit in all algebraic constitutive relationships for turbulent stresses.

3.1.3 Objective

An algebraic Reynolds stress model is developed for compressible flows by accounting for the changing nature of pressure at different gradient Mach number regimes, $M_g \equiv S\ell/a$, where S is the magnitude of the rate of strain tensor, and ℓ is a turbulent lengthscale. The present ARSM derives its physical attributes from the rapid distortion theory calculations of Lavin et al. [45], and Bertsch [5], as well as the direct numerical simulations of Sarkar [71]. It is demonstrated that the resulting constitutive relation is realizable. The ARSM is initially validated by comparing model calculations against the long time behavior of the compressible homogeneous shear DNS of Sarkar [71]. To assess the utility of the proposed model for inhomogeneous high-speed flows, computations are performed of the plane supersonic mixing layer and compared against the experimental data of Goebel & Dutton [33]. Comparisons

are also made against incompressible ARSM, and standard $k-\varepsilon$ models both with and without the Sarkar et al. [72] compressibility correction.

3.1.4 Chapter outline

In §3.2 the Reynolds stress equations are given, and the pressure-strain correlation modeling philosophy is briefly outlined. Section 3.3 develops the ARSM for compressible shear flows. The realizability of the resulting ARSM is provided in §3.4. The ARSM is used to compute homogeneous shear flow and compared with DNS data in §3.5. In §3.6 the ARSM is used to compute high-speed plane mixing-layers and the results are compared with experiments. Concluding remarks are given in §3.7. Appendix A provides curve fits of the compressible pressure-strain correlation model coefficients employed in the ARSM.

3.2 Reynolds stress closure equation

For compressible flows, the Navier–Stokes equations are typically expressed in Favre-averaged form. The Favre average of a variable ϕ is defined as

$$\tilde{\phi} = \frac{\overline{\rho\phi}}{\overline{\rho}}, \tag{3.1}$$

where ρ is the fluid density, $\overline{(\cdot)}$ denotes a Reynolds average, and $\tilde{(\cdot)}$ a Favre average. In the following ϕ' and ϕ'' denote Reynolds and Favre fluctuations respectively. The Reynolds stress tensor is given by

$$R_{ij} = \frac{\overline{\rho u_i'' u_j''}}{\overline{\rho}}. \tag{3.2}$$

Using these definitions, the Favre averaged conservation of mass, momentum and total energy equations become

$$\frac{\partial \overline{\rho}}{\partial t} + \frac{\partial}{\partial x_i}(\overline{\rho}\tilde{u}_i) = 0, \tag{3.3}$$

$$\frac{\partial}{\partial t}(\overline{\rho}\tilde{u}_i) + \frac{\partial}{\partial x_j}(\overline{\rho}\tilde{u}_i\tilde{u}_j) = -\frac{\partial \overline{p}}{\partial x_i} + \frac{\partial}{\partial x_k}\left(\overline{\sigma}_{ik} - \overline{\rho}R_{ik}\right), \tag{3.4}$$

$$\frac{\partial}{\partial t}(\overline{\rho}E) + \frac{\partial}{\partial x_i}\left(\overline{\rho}\tilde{u}_i H\right) = \frac{\partial}{\partial x_j}\left[-q_{L_j} - \overline{\rho u_j'' h''} + \overline{\sigma_{ij}u_i''} - \frac{1}{2}\overline{\rho u_i'' u_i'' u_j''} + \tilde{u}_i\left(\overline{\sigma}_{ij} - \overline{\rho}R_{ij}\right)\right], \tag{3.5}$$

where $\overline{p}$ is the average pressure, $\overline{\sigma}_{ij}$ the viscous stress tensor, E total energy, H total enthalpy, and q_{L_j} the laminar heat flux vector. The total energy and enthalpy are given by

$$E = \tilde{e} + \frac{\tilde{u}_i\tilde{u}_i}{2} + k, \quad H = \tilde{h} + \frac{\tilde{u}_i\tilde{u}_i}{2} + k, \tag{3.6}$$

where $\tilde{e}$ is the specific internal energy, $\tilde{h}$ specific enthalpy, and $k = R_{ii}/2$ is the turbulent kinetic energy. For a Newtonian fluid, the viscous stress tensor is

$$\sigma_{ij} = \mu\left(\frac{\partial u_i}{\partial x_j} + \frac{\partial u_j}{\partial x_i}\right) - \frac{2}{3}\mu\frac{\partial u_k}{\partial x_k}\delta_{ij}, \quad \delta_{ij} = \begin{cases} 1 & \text{if } i = j, \\ 0 & \text{otherwise,} \end{cases} \tag{3.7}$$

where μ is the molecular viscosity, and δ_{ij} the Kronecker delta tensor. The laminar heat flux vector is

$$q_{L_j} = -\kappa\frac{\partial \tilde{T}}{\partial x_j}, \tag{3.8}$$

where κ is the thermal conductivity, and $\tilde{T}$ temperature. The focus of this work is on the development of an algebraic model that incorporates the changing role of pressure on the turbulent constitutive relation. For the sake of completeness, models for the other unclosed terms are briefly discussed.

3.2.1 Energy equation closures

At the most elementary level, the turbulent enthalpy flux is modeled as

$$q_{T_j} = \overline{\rho u_j'' h''} = -\frac{c_p \mu_t}{Pr_t} \frac{\partial \tilde{T}}{\partial x_j}, \tag{3.9}$$

where Pr_t is the turbulent Prandtl number, μ_t is the turbulent viscosity, and c_p is the specific heat at constant pressure. Standard two equation models compute the turbulent viscosity using

$$\mu_t = \frac{\overline{\rho} C_\mu k^2}{\varepsilon}, \quad k = \frac{1}{2} R_{ii}, \quad \varepsilon = \frac{1}{2} \varepsilon_{ii}, \tag{3.10}$$

where ε is the dissipation rate. Typical modeling constants used are

$$C_\mu = 0.09, \quad Pr_t = 0.85. \tag{3.11}$$

A more sophisticated closure model for the turbulent heat flux in high-speed shear flows is presented by Bowersox [7]. The two terms $\overline{\sigma_{ij} u_i''}$ and $\frac{1}{2}\overline{\rho u_i'' u_i'' u_j''}$ on the right hand side of equation (3.5) are the molecular diffusion and turbulent transport of turbulence kinetic energy. If $\overline{\rho} k \ll \overline{p}$, these terms may be neglected, see Wilcox [94]. However, for hypersonic flows these terms may be important, and the following approximation has been suggested

$$\overline{\sigma_{ij} u_i''} - \frac{1}{2}\overline{\rho u_i'' u_i'' u_j''} = \left(\mu + \frac{\mu_t}{\sigma_k} \right) \frac{\partial k}{\partial x_j}, \quad \sigma_k = 0.82. \tag{3.12}$$

Introducing equations (3.9) and (3.12) in equation (3.5) yields the modeled total energy equation

$$\frac{\partial}{\partial t}(\overline{\rho}E) + \frac{\partial}{\partial x_i}\left(\overline{\rho}\tilde{u}_i H\right) = \frac{\partial}{\partial x_j}\left[\left(\kappa + \frac{c_p \mu_t}{Pr_t}\right)\frac{\partial \tilde{T}}{\partial x_j} + \left(\mu + \frac{\mu_t}{\sigma_k}\right)\frac{\partial k}{\partial x_j} + \tilde{u}_i\left(\overline{\sigma}_{ij} - \overline{\rho}R_{ij}\right)\right]. \tag{3.13}$$

3.2.2 Reynolds stress closures

Starting from the momentum equation, it is straightforward to arrive at the Favre averaged Reynolds stress equation

$$\frac{\partial(\overline{\rho}R_{ij})}{\partial t} + \frac{\partial(\overline{\rho}\tilde{u}_k R_{ij})}{\partial x_k} = \overline{\rho}\left(P_{ij} - \varepsilon_{ij}\right) - \frac{\partial T_{ijk}}{\partial x_k} + \Pi_{ij} + \Sigma_{ij}, \tag{3.14}$$

where P_{ij} is the production tensor, ε_{ij} the dissipation tensor, T_{ijk} the turbulent transport tensor, Π_{ij} the pressure-strain correlation, and Σ_{ij} the mass flux coupling tensor. Of the five terms on the right hand side of equation (3.14), the production tensor is the only one in closed form

$$P_{ij} = -R_{ik}\frac{\partial \tilde{u}_j}{\partial x_k} - R_{jk}\frac{\partial \tilde{u}_i}{\partial x_k}. \tag{3.15}$$

The remaining four terms require closure modeling

$$\varepsilon_{ij} = \frac{1}{\overline{\rho}}\left(\overline{\sigma'_{jk}\frac{\partial u''_i}{\partial x_k} + \sigma'_{ik}\frac{\partial u''_j}{\partial x_k}}\right), \tag{3.16}$$

$$T_{ijk} = \overline{\rho u''_i u''_j u''_k} + \overline{p' u''_i}\delta_{jk} + \overline{p' u''_j}\delta_{ik} - \overline{\sigma'_{jk}u''_i} - \overline{\sigma'_{ik}u''_j}, \tag{3.17}$$

$$\Pi_{ij} = \overline{p'\left(\frac{\partial u''_i}{\partial x_j} + \frac{\partial u''_j}{\partial x_i}\right)}, \tag{3.18}$$

and

$$\Sigma_{ij} = \overline{u_i''}\left(\frac{\partial \overline{\sigma}_{jk}}{\partial x_k} - \frac{\partial \overline{p}}{\partial x_j}\right) + \overline{u_j''}\left(\frac{\partial \overline{\sigma}_{ik}}{\partial x_k} - \frac{\partial \overline{p}}{\partial x_i}\right). \tag{3.19}$$

The transport tensor is modeled using the traditional scalar turbulent diffusivity approach [48]

$$-\frac{\partial T_{ijk}}{\partial x_k} = \frac{\partial}{\partial x_k}\left[\left(\mu + \frac{\mu_t}{\sigma_k}\right)\frac{\partial R_{ij}}{\partial x_k}\right]. \tag{3.20}$$

An isotropic model is used for the dissipation tensor

$$\varepsilon_{ij} = \frac{2}{3}\varepsilon\delta_{ij}, \tag{3.21}$$

where the turbulent dissipation rate ε is found by solving a model evolution equation.

DNS of supersonic shear layers [57] has demonstrated that the mass flux coupling term Σ_{ij} is negligible in the Reynolds stress budgets. Since the present model is intended to capture the compressibility effects associated with high-speed boundary and mixing-layers, it is reasonable to neglect this term. However, for flows driven by density gradients, this term is of paramount importance, see Livescu & Ristorcelli [51, 52]. An algebraic turbulent mass flux model is presented by Ristorcelli [65] for buoyancy driven flows.

3.2.2.1 Pressure-strain correlation

The only term remaining that requires modeling is the pressure-strain correlation tensor. Classical pressure-strain correlation modeling methodology [83] commences from the following form

$$\Pi_{ij} = \overline{\rho}\varepsilon\mathcal{A}_{ij}(\mathbf{b}) + \overline{\rho}k\mathcal{M}_{ijkl}(\mathbf{b})\frac{\partial \tilde{u}_k}{\partial x_l}, \tag{3.22}$$

where

$$b_{ij} \equiv \frac{R_{ij}}{2k} - \frac{1}{3}\delta_{ij}, \tag{3.23}$$

is the anisotropy tensor. The pressure-strain correlation is decomposed into its slow (non-linear) and rapid (linear) parts

$$\Pi_{ij} = \Pi_{ij}^{(s)} + \Pi_{ij}^{(r)}, \quad \Pi_{ij}^{(s)} = \overline{\rho}\varepsilon\mathcal{A}_{ij}\left(\mathbf{b}\right), \quad \Pi_{ij}^{(r)} = \overline{\rho}k\mathcal{M}_{ijkl}\left(\mathbf{b}\right)\frac{\partial\tilde{u}_k}{\partial x_l}. \tag{3.24}$$

Dimensional analysis and representation theory [60, 79] of tensor-valued isotropic functions allows the pressure-strain correlation to be written as

$$\Pi_{ij} = \overline{\rho}\varepsilon f_{ij}\left(\mathbf{b}, \tau\mathbf{S}^*, \tau\mathbf{W}^*\right) = \overline{\rho}\varepsilon\sum_k C_k T_{ij}^k, \quad \tau = \frac{k}{\varepsilon}, \tag{3.25}$$

where

$$S_{ij}^* = \frac{1}{2}\left(\frac{\partial\tilde{u}_i}{\partial x_j} + \frac{\partial\tilde{u}_j}{\partial x_i}\right) - \frac{1}{3}\frac{\partial\tilde{u}_k}{\partial x_k}\delta_{ij}, \quad W_{ij}^* = \frac{1}{2}\left(\frac{\partial\tilde{u}_i}{\partial x_j} - \frac{\partial\tilde{u}_j}{\partial x_i}\right), \tag{3.26}$$

are the modified rate of strain and rotation rate tensors respectively. The C_k coefficients in equation (3.25) are in general scalar functions of the independent tensor invariants of T_{ij}^k, although many popular models use constant values for some or all of these coefficients [39, 43, 83]. Pressure-strain correlation models that have been developed with variable coefficients are given by Ristorcelli et al. [66], Girimaji [27], and Mishra & Girimaji [55].

Compressible rapid distortion theory studies have shown that the linear pressure-strain correlation is profoundly affected by compressibility [5,8,45,50,77]. The studies by Simone et al. [77] and Thacker et al. [88] suggest that the rapid or linear pressure is chiefly responsible for the reduction of turbulent kinetic energy growth rates in compressible homogeneous shear at high gradient Mach number. The implication for

modeling is that critical changes to the incompressible rapid pressure-strain correlation closure are needed for applicability in compressible flows. Furthermore, these changes should be parameterized by the gradient Mach number [8, 17, 45, 71]. In this work, the gradient (M_g) and turbulent (M_t) Mach numbers are defined as

$$M_g \equiv \frac{S\ell}{a}, \quad S = \sqrt{2S^*_{ij}S^*_{ij}}, \quad \ell = \frac{k^{3/2}}{\varepsilon}, \quad a = \sqrt{\gamma R\tilde{T}}, \tag{3.27}$$

$$M_t \equiv \frac{\sqrt{2k}}{a}, \quad \frac{M_t}{M_g} = \sqrt{2}\left(\frac{Sk}{\varepsilon}\right)^{-1}, \tag{3.28}$$

where a is the speed of sound, γ the specific heat ratio, and R the specific gas constant. The gradient Mach number represents the ratio of shear to acoustic timescale, whereas the turbulent Mach number characterizes the magnitude of velocity fluctuations relative to speed of sound. The relative magnitudes of the mean flow distortion timescale ($\tau_d = 1/S$), and acoustic timescale ($\tau_a = \ell/a$) determine the magnitude of the gradient Mach number ($M_g = \tau_a/\tau_d$). As a simplification the integral length-scale is employed to compute the gradient Mach number. For details regarding this simplification, please see Gomez & Girimaji [34]. In hypersonic flows of aerospace engineering interest, gradient Mach numbers can be much larger than unity. However, turbulent Mach numbers are typically smaller than unity. In the model development phase, only a parameter range of practical utility is used: gradient Mach numbers up to 10 and turbulence Mach numbers less than 0.6.

In this work the pressure-strain correlation model developed by Gomez & Girimaji [34] is used, which incorporates compressibility effects through the gradient Mach number. This model has been shown to be able to capture the essential physics of compressible homogeneous shear DNS and supersonic mixing-layers [34]. The form

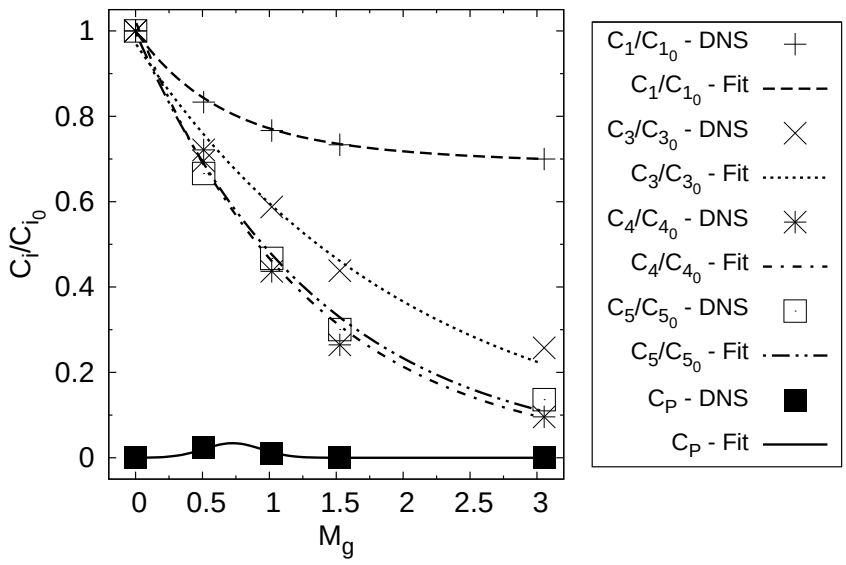

Figure 3.2: Calibrated coefficients of the GG-I pressure-strain correlation model [34]. Symbols show best agreement with DNS [71], lines are least squares curve fits, given by equations (A.1)–(A.4) and table A.1.

of the Gomez & Girimaji model, hereafter referred to as the GG-I model, is given by

$$\begin{aligned}\Pi_{ij} = &- C_1\overline{\rho}\varepsilon b_{ij} + C_3\overline{\rho}kS^*_{ij} + C_4\overline{\rho}k\left(b_{ik}S^*_{jk} + b_{jk}S^*_{ik} - \tfrac{2}{3}b_{mn}S^*_{mn}\delta_{ij}\right) \\ &+ C_5\overline{\rho}k\left(b_{ik}W^*_{jk} + b_{jk}W^*_{ik}\right) - C_P\overline{\rho}P_{ij}, \end{aligned} \tag{3.29}$$

where the C_k and C_P coefficients are functions of gradient Mach number. The model coefficients have been calibrated with the compressible homogeneous shear DNS of Sarkar [71] and are shown in figure 3.2.

The GG-I pressure-strain correlation model has its basis in previous works using rapid distortion theory [5, 44, 45]. The details regarding the development of the GG-I model can be found in Gomez & Girimaji [34], here the three stage behavior that served as physical inspiration is briefly outlined. By examining the effect of pressure at different gradient Mach number regimes, the following three important

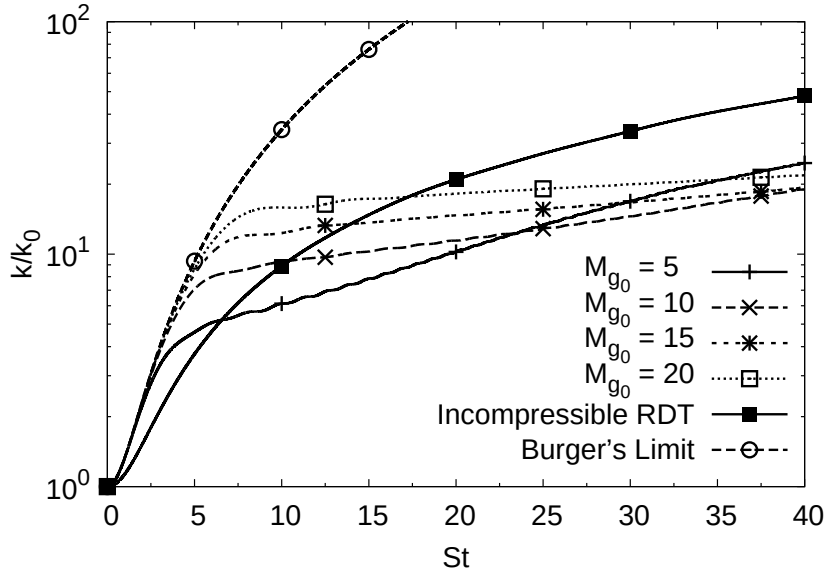

Figure 3.3: Turbulent kinetic energy evolution in shear time. RDT of compressible homogeneous shear flow, taken from Bertsch [5].

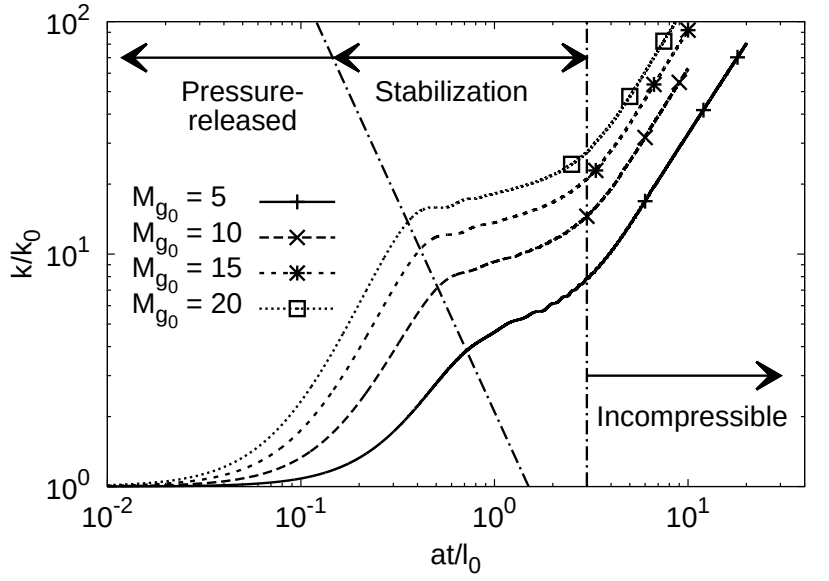

Figure 3.4: Turbulent kinetic energy evolution in acoustic time. RDT of compressible homogeneous shear flow, taken from Bertsch [5].

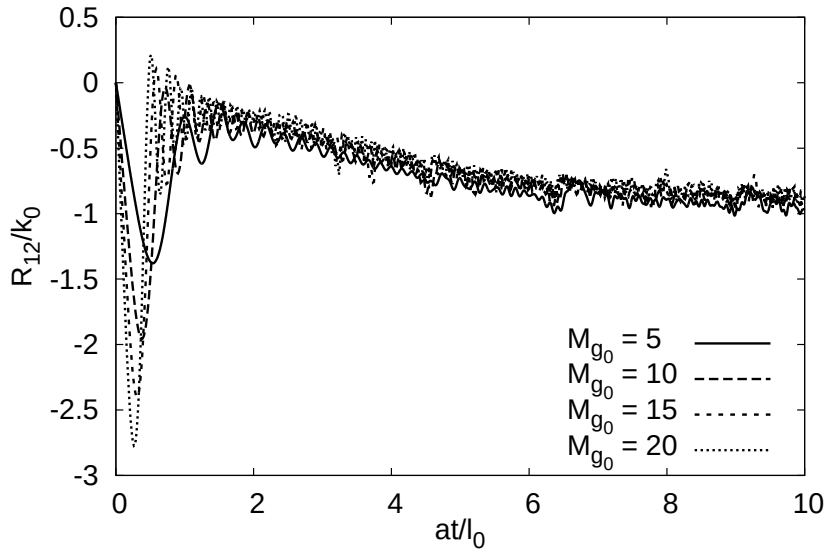

Figure 3.5: Normalized Reynolds shear stress evolution in acoustic time. RDT of compressible homogeneous shear flow, taken from Bertsch [5].

observations can be made:

Regime 1, – ($M_g \gg 1$, $\tau_a \gg \tau_d$): In this regime the acoustic time scale is much larger than that of shear. Pressure changes too slowly to affect the flow dynamics. The turbulent kinetic energy growth rate in the pressure-released stage increases with initial gradient Mach number, as can be seen for $St < 2$ in figure 3.3. In this limit, the flow evolution can be closely approximated by the three-dimensional Burgers equation.

Regime 2, – ($M_g \sim 1$, $\tau_a \sim \tau_d$): This flow regime occurs when the mean distortion and acoustic timescales are of similar magnitude. In this stage both inertial and pressure effects play critical roles. The acoustic character of the pressure field is most evident in this regime. Pressure waves are established in the flow normal (shear) direction. This leads to oscillatory behavior of shear-normal velocity fluctuations [45]. Consequently the fluctuating shear stress also evolves

in an oscillatory manner as shown by Bertsch [5] and Lavin et al. [45] The small value of R_{12} in this stage results in a negligible net growth of turbulent kinetic energy as seen in figure 3.4. During this stabilization stage Bertsch [5] demonstrates that on an average $\Pi_{12}^{(r)} + \overline{\rho} P_{12} \approx 0$. Based on these observations, the shear production blocking by the corresponding pressure-strain correlation component is incorporated into the compressible pressure-strain correlation closure model, equation (3.29).

Regime 3, – ($M_g \ll 1$, $\tau_a \ll \tau_d$): In this regime, the turbulent kinetic energy growth rates for all cases are reasonably similar to that of low gradient Mach number, as seen in figure 3.4. The RDT computations of Bertsch [5] demonstrate that for this stage the normalized shear Reynolds stress goes to an approximately constant value independent of initial gradient Mach number, as seen for large acoustic time in figure 3.5. At low gradient Mach number, pressure assumes the role of enforcing incompressibility and is governed by a Poisson equation. Pressure equilibrates almost instantaneously to inertial effects and maintains incompressibility. Any remnant dilatational fluctuations are rapidly dissipated by viscous effects. For this low M_g regime, a standard incompressible pressure-strain correlation model is adequate. Figure 3.2 shows that the compressible pressure-strain correlation model reverts to a standard incompressible form as $M_g \rightarrow 0$.

The trace of equation (3.29) yields the implied model for the pressure dilatation Π:

$$\Pi \equiv \frac{1}{2}\Pi_{ii} = -\overline{\rho} C_P P. \tag{3.30}$$

where $P = P_{ii}/2$. For positive C_P, the above model guarantees that for shear dominated flows in the absence of heat release the net transfer of energy is from

kinetic to internal, as observed in DNS [49, 70]. Thus Π will be predominantly negative leading to a reduced production of turbulent kinetic energy and an increase in internal energy. In Gomez & Girimaji [34] it is argued that pressure-dilatation modifies the spectral cascade rate, and therefore a modification to the standard dissipation rate model is required. Therein it was found that the modified dissipation rate model yielded almost identical results with the standard dissipation model. Therefore, in the present work the standard dissipation rate model is used

$$\frac{\partial}{\partial t}(\overline{\rho}\varepsilon) + \frac{\partial}{\partial x_i}(\overline{\rho}\varepsilon\tilde{u}_i) = \frac{\partial}{\partial x_j}\left[\left(\mu + \frac{\mu_t}{\sigma_\varepsilon}\right)\frac{\partial \varepsilon}{\partial x_j}\right] + C_{\varepsilon_1}\overline{\rho}\frac{\varepsilon}{k}P - C_{\varepsilon_2}\overline{\rho}\frac{\varepsilon^2}{k}, \tag{3.31}$$

where the constants used are [48, 83]

$$C_{\varepsilon_1} = 1.44, \quad C_{\varepsilon_2} = 1.83, \quad \sigma_\varepsilon = 1.0. \tag{3.32}$$

This completes the turbulence modeling at the RSCM level of closure. In the next section, the algebraic model for the Reynolds stresses is developed from the RSCM equations.

3.3 ARSM for compressible flows

The sequence of steps in the explicit ARSM closure development procedure [25] are summarized in figure 3.6. Invoking the weak equilibrium assumption yields an implicit algebraic equation for the anisotropy tensor. Next either the full or truncated form of the anisotropy tensor given by representation theory is employed in the implicit algebraic equation. Inserting models for the pressure-strain correlation and dissipation tensor into the algebraic equation yields a polynomial equation that must be solved with a procedure that identifies the physically correct root. This section will only discuss the main steps towards obtaining the algebraic model, additional

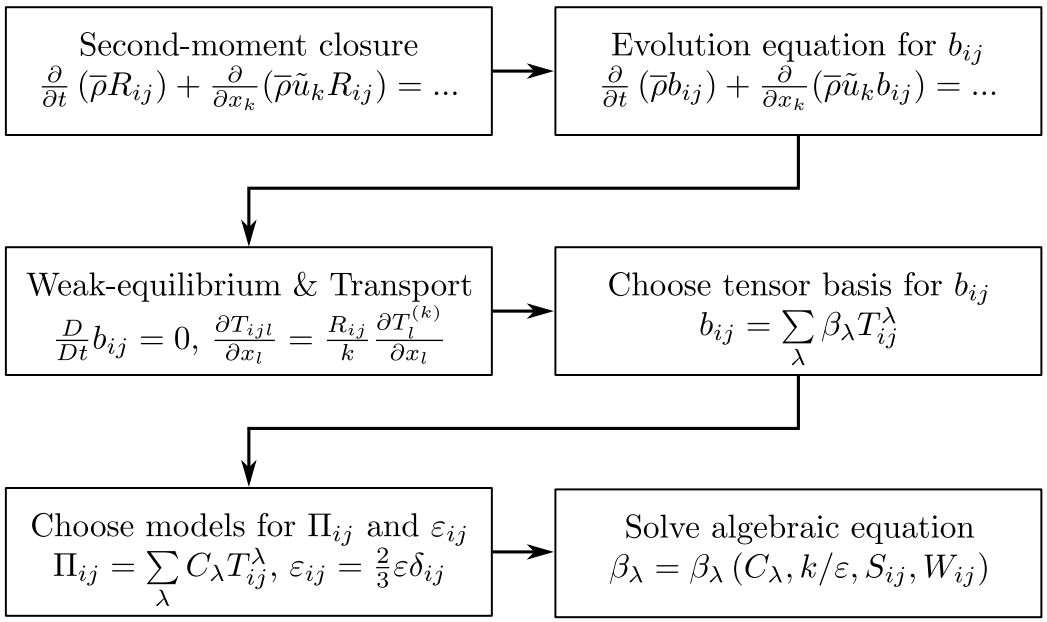

Figure 3.6: ARSM development steps.

details may be found elsewhere [23,25,26,31,61,89]. Gatski & Jongen [22] provide an excellent summary of the similarities and differences among current algebraic models.

The starting point is the evolution equation of the Reynolds stresses, repeated here for convenience

$$\frac{\partial(\overline{\rho}R_{ij})}{\partial t} + \frac{\partial(\overline{\rho}\tilde{u}_k R_{ij})}{\partial x_k} = \overline{\rho}\left(P_{ij} - \varepsilon_{ij}\right) - \frac{\partial T_{ijk}}{\partial x_k} + \Pi_{ij}, \tag{3.33}$$

where the terms on the right hand side are defined in equations (3.15), (3.20), (3.21), (3.29), and the mass-flux tensor has been neglected. Contracting equation (3.33) gives

$$\overline{\rho}\frac{Dk}{Dt} = \overline{\rho}\Big[\left(1 - C_P\right)P - \varepsilon\Big] - \frac{\partial T_l^{(k)}}{\partial x_l}, \tag{3.34}$$

where

$$\frac{D}{Dt} \equiv \left(\frac{\partial}{\partial t} + \tilde{u}_k\frac{\partial}{\partial x_k}\right), \tag{3.35}$$

is the Lagrangian derivative. Expressing the Reynolds stress evolution equation (3.33) in terms of the anisotropy tensor equation (3.23) and using equation (3.34) yields

$$2k\overline{\rho}\frac{Db_{ij}}{Dt}+\left(T_{ijl,l}-\frac{R_{ij}}{k}\frac{\partial T_l^{(k)}}{\partial x_l}\right)=-\frac{\overline{\rho}R_{ij}}{k}\left[\left(1-C_P\right)P-\varepsilon\right]+\overline{\rho}\left(P_{ij}-\varepsilon_{ij}\right)+\Pi_{ij}, \quad (3.36)$$

where $P=P_{ii}/2$, and $\varepsilon=\varepsilon_{ii}/2$.

For many flows of practical interest, further simplification can be achieved by invoking the weak-equilibrium assumption [23, 25, 61, 89]

$$\frac{Db_{ij}}{Dt}=\frac{\partial b_{ij}}{\partial t}+\tilde{u}_k\frac{\partial b_{ij}}{\partial x_k}=0. \quad (3.37)$$

The weak-equilibrium equation is valid in many flows wherein the timescale of anisotropy evolution is rapid compared to the timescales of mean flow, turbulent kinetic energy, and dissipation rate [28]. A Galilean-invariant weak-equilibrium simplification can also be formulated for flows with streamline curvature, for details see Girimaji [26], and Wallin & Johansson [90]. Additional improvements can be achieved by incorporating low-order non-equilibrium terms within the algebraic modeling framework as shown by Girimaji [28]. For notational simplicity, here the weak-equilibrium assumption in the standard Cartesian coordinate frame [23, 25, 61, 89] is used.

By modeling the turbulent transport tensor as

$$T_{ijl,l}=\frac{R_{ij}}{k}\frac{\partial T_l^{(k)}}{\partial x_l}, \quad (3.38)$$

and using the weak-equilibrium assumption above, the following algebraic equation

for anisotropy can be obtained

$$2b_{ij}\left[(1-C_P)\frac{P}{\varepsilon}-1\right]=\frac{1}{\overline{\rho}\varepsilon}\left[\overline{\rho}\left(P_{ij}-\varepsilon_{ij}\right)+\Pi_{ij}\right]-\frac{2}{3}\left[(1-C_P)\frac{P}{\varepsilon}-1\right]\delta_{ij}. \quad (3.39)$$

Inserting the isotropic dissipation tensor model equation (3.21), the compressible pressure-strain correlation from equation (3.29), and simplifying yields the following implicit algebraic equation for the anisotropy tensor

$$\begin{aligned} b_{ij}\left[(1-C_P)\left(\frac{P}{\varepsilon}+\frac{2\Delta}{3}\right)+\frac{1}{2}C_1-1\right] =& L_3S_{ij}+L_4\left[b_{ik}S_{kj}+S_{ik}b_{kj}-\frac{2}{3}b_{mn}S_{mn}\delta_{ij}\right] \\ &+L_5\left[W_{ik}b_{kj}-b_{ik}W_{kj}\right], \end{aligned} \quad (3.40)$$

where the modified and normalized rate of strain and rotation tensors have been used

$$S_{ij}=\frac{\tau}{2}\left(\frac{\partial\tilde{u}_i}{\partial x_j}+\frac{\partial\tilde{u}_j}{\partial x_i}\right)-\frac{\Delta}{3}\delta_{ij}, \quad W_{ij}=\frac{\tau}{2}\left(\frac{\partial\tilde{u}_i}{\partial x_j}-\frac{\partial\tilde{u}_j}{\partial x_i}\right), \quad \Delta=\tau\frac{\partial\tilde{u}_k}{\partial x_k}. \quad (3.41)$$

The characteristic turbulent time scale is given by τ, and Δ is the normalized dilatation. Here the turbulence timescale is $\tau=k/\varepsilon$. The coefficients of equation (3.40) are

$$L_3=\frac{C_3}{2}-\frac{2}{3}\left(1-C_P\right), \quad L_4=\frac{C_4}{4}-\frac{1}{2}\left(1-C_P\right), \quad L_5=\frac{C_5}{4}-\frac{1}{2}\left(1-C_P\right). \quad (3.42)$$

The three term expansion of the anisotropy tensor for two dimensional incompressible mean flows given by Girimaji [25] is used

$$b_{ij}=\beta_1S_{ij}+\beta_2\left(S_{ik}W_{kj}-W_{ik}S_{kj}\right)+\beta_3\left(S_{ik}S_{kj}-\tfrac{1}{3}\eta_1\delta_{ij}\right), \quad (3.43)$$

where the tensor invariants η_1 and η_2 are defined as

$$\eta_1 = S_{ij}S_{ij}, \qquad \eta_2 = W_{ij}W_{ij}. \tag{3.44}$$

It is important to note that this three term expansion does not form a complete basis for the anisotropy tensor in a general two dimensional *compressible* flow due to the S_{33} term which may now take nonzero values. However adding additional tensor groups to the right hand side of equation (3.43) significantly complicates calculating the coefficients β_i, to the point of rendering the algebraic approach impractical [89]. Nonetheless, the objective of this work is to show that the compressible pressure-strain correlation is able to capture compressibility effects when incorporated in an algebraic model, albeit a simplified one. In the same vein, minor tensor approximations strictly valid only for incompressible flows are required to obtain a fully explicit algebraic model for compressible flows, see Wallin & Johansson [89]. Inserting equation (3.43) in (3.40) yields the tensor coefficients

$$\beta_2 = \frac{-\beta_1 L_5}{-\left(1-C_P\right)\beta_1\eta_1 + \frac{1}{2}C_1 - 1}, \quad \beta_3 = \frac{2\beta_1 L_4}{-\left(1-C_P\right)\beta_1\eta_1 + \frac{1}{2}C_1 - 1}. \tag{3.45}$$

Provided $C_1 > 2$, equation (3.45) guarantees non-singular behavior. Tensor coefficient β_1 is obtained by solving the cubic equation

$$\beta_1^3 + n_1\beta_1^2 + n_2\beta_1 + n_3 = 0. \tag{3.46}$$

The standard procedure for finding the roots of equation (3.46) involves calculating the following quantities

$$n_1 = \frac{-2\left(\frac{1}{2}C_1 - 1\right)}{\left(1-C_P\right)\eta_1}, \quad n_2 = \frac{\left(\frac{1}{2}C_1 - 1\right)^2 + \left(1-C_P\right)\eta_1 L_3 - \frac{2}{3}\eta_1 L_4^2 + 2\eta_2 L_5^2}{\left(1-C_P\right)^2\eta_1^2}, \tag{3.47}$$

$$n_3 = \frac{-\left(\frac{1}{2}C_1 - 1\right) L_3}{\left(1 - C_P\right)^2 \eta_1^2}, \quad n_4 = n_2 - \frac{n_1^2}{3}, \quad n_5 = \frac{1}{27}\left(2n_1^3 - 9n_1 n_2 + 27 n_3\right), \tag{3.48}$$

along with the discriminant D,

$$D = \frac{n_5^2}{4} + \frac{n_4^3}{27}. \tag{3.49}$$

The value of β_1 may now be found using

$$\beta_1 = \begin{cases} -\dfrac{n_1}{3} + \left(-\dfrac{n_5}{2} + \sqrt{D}\right)^{1/3} + \left(-\dfrac{n_5}{2} - \sqrt{D}\right)^{1/3} & \text{for } D > 0, \\ -\dfrac{n_1}{3} + 2\sqrt{\dfrac{-n_4}{3}}\cos\left(\dfrac{\theta}{3}\right) & \text{for } D < 0 \text{ and } n_5 < 0, \\ -\dfrac{n_1}{3} + 2\sqrt{\dfrac{-n_4}{3}}\cos\left(\dfrac{\theta}{3} + \dfrac{2\pi}{3}\right) & \text{for } D < 0 \text{ and } n_5 > 0, \end{cases} \tag{3.50}$$

where θ is given by

$$\cos\left(\theta\right) = \frac{-n_5/2}{\sqrt{-n_4^3/27}}. \tag{3.51}$$

The production to dissipation ratio can be found using

$$\frac{P}{\varepsilon} = -2 b_{mn} S_{mn} - \frac{2}{3}\Delta. \tag{3.52}$$

Figures 3.7(a) – 3.8(b) show β_1 as a function of tensor invariants η_1 and η_2 for different gradient Mach numbers. Figure 3.7(a) corresponds to the incompressible limit and is similar to the incompressible model given by Girimaji [25]. For shear dominated flows, $\eta_1 \approx \eta_2$, and the effect of compressibility is to reduce the absolute value of β_1. This can be seen in figure 3.9 where β_1 is plotted for the case $\eta_1 = \eta_2$ at three different gradient Mach numbers. It is easy to conclude that for shear dominated flows, $\beta_1 \to 0$ as the gradient Mach number increases.

The standard Boussinesq approximation uses

$$b_{ij} = -C_\mu S_{ij}, \quad C_\mu = 0.09, \quad \mu_t = \frac{\overline{\rho} C_\mu k^2}{\varepsilon}. \tag{3.53}$$

Comparing equation (3.53) with the non-linear constitutive equation (3.43), the following relationship becomes clear

$$C_\mu = -\beta_1. \tag{3.54}$$

Therefore the present algebraic model computes the turbulent viscosity using

$$\mu_t = \frac{-\overline{\rho}\beta_1 k^2}{\varepsilon}. \tag{3.55}$$

For comparison, the standard value of C_μ is plotted along with β_1 in figures 3.7(a) – 3.8(b). In the following section, it is shown that the three term algebraic model given by (3.43) yields fully realizable Reynolds stresses.

3.4 Realizability of ARSM

Realizability is an important requirement on closure models [75]. A realizable Reynolds stress model is paramount for eliminating the unphysical behavior that can be exhibited by turbulence closure models near stagnation points in bluff body and impinging jet flows [4, 86]. In turbulence literature there is a considerable body of work that addresses the virtues and usefulness of strong vs. weak forms of realizability, see Pope [63] and references therein. Indeed, current state of the art realizability considerations go beyond positive-definiteness of the Reynolds stress tensor and further directly impose constraints on the pressure-strain correlation closure [29]. However, these constraints can be quite severe, and no current practical

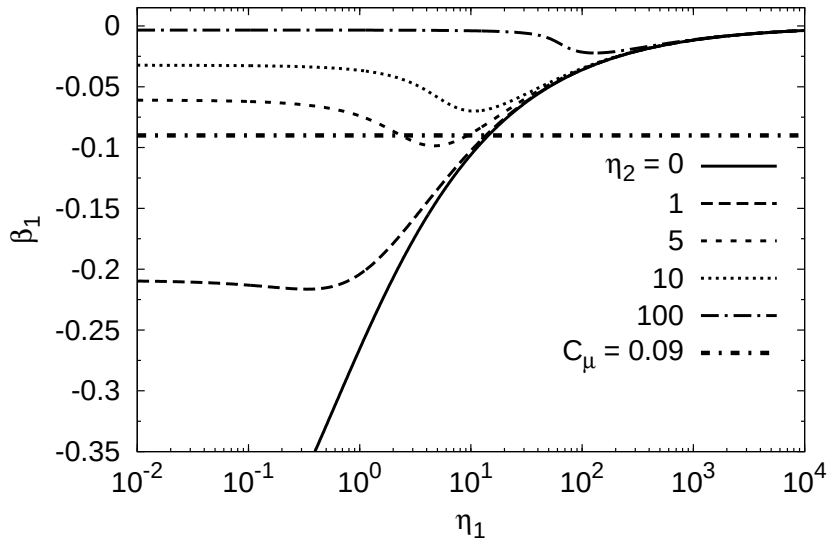

(a) β_1 at $M_g = 0.0$

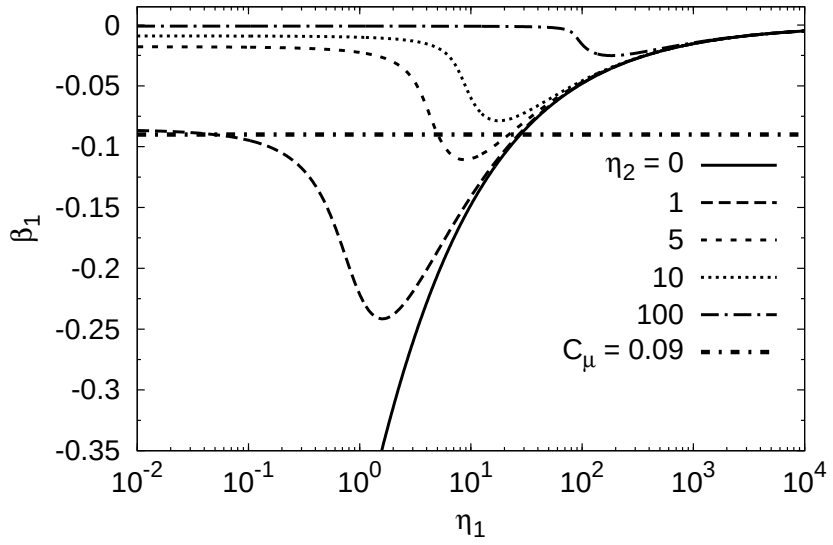

(b) β_1 at $M_g = 0.75$

Figure 3.7: β_1 coefficient for (a) $M_g = 0.0$, and (b) $M_g = 0.75$.

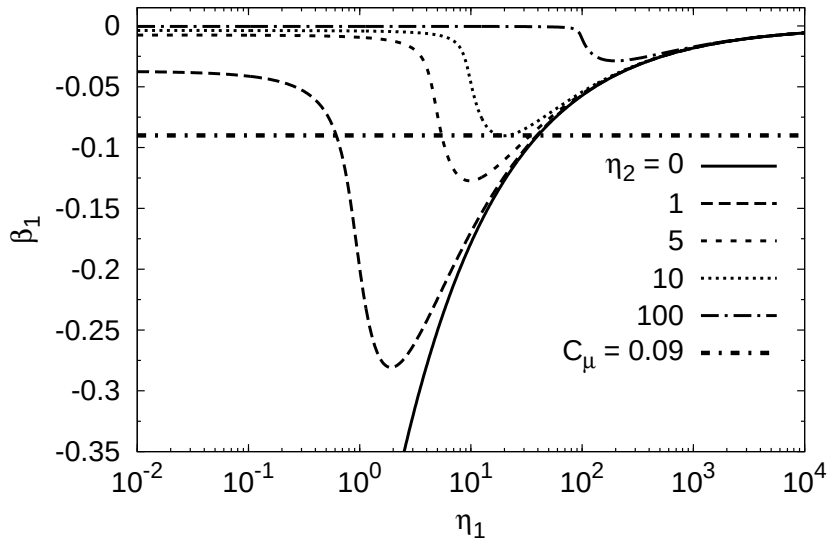

(a) β_1 at $M_g = 1.50$

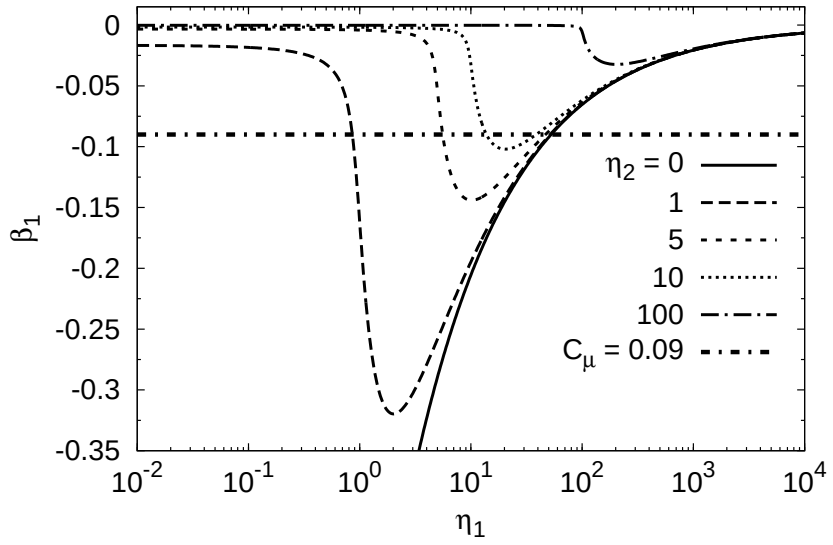

(b) β_1 at $M_g = 3.0$

Figure 3.8: β_1 coefficient for (a) $M_g = 1.50$, and (b) $M_g = 3.0$.

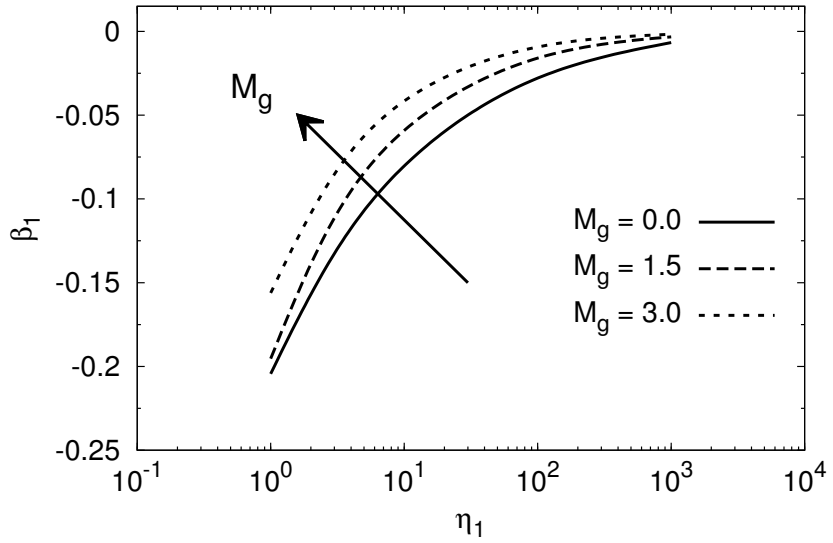

Figure 3.9: β_1 coefficient when $\eta_1 = \eta_2$, shown for different values of M_g. Arrow points towards increasing gradient Mach number.

model satisfies all of them, as discussed in Pope [63] page 427. For engineering applications the pragmatic approach is to disallow negative energetic Reynolds stresses, as proposed by Durbin [15]. This must be considered a necessary if not sufficient condition for realizability. In the present work, following Durbin [15], the positivity requirement on the diagonal elements of the Reynolds stress tensor is analyzed in the principal coordinates of the rate of strain tensor to derive constraints on tensor coefficients β_i. Using the definition of the anisotropy tensor, equation (3.23) and the requirement

$$0 \leq R_{\alpha\alpha} \leq 2k, \quad \forall\, \alpha, \tag{3.56}$$

the anisotropy tensor can be bounded to

$$-\frac{1}{3} \leq b_{\alpha\alpha} \leq \frac{2}{3}, \quad \forall\, \alpha, \tag{3.57}$$

where no summation is implied with repeated α.

If the anisotropy tensor is proven to be realizable in one coordinate frame, then it will be realizable in any other coordinate frame obtained by an orthonormal coordinate transformation. Using this property the strain and rotation rate tensors can be expressed in the principal axes of the strain rate tensor

$$S_{ij} = \begin{bmatrix} \lambda_1 & 0 & 0 \\ 0 & \lambda_2 & 0 \\ 0 & 0 & \lambda_3 \end{bmatrix}, \qquad W_{ij} = \begin{bmatrix} 0 & \omega_1 & \omega_2 \\ -\omega_1 & 0 & \omega_3 \\ -\omega_2 & -\omega_3 & 0 \end{bmatrix}. \tag{3.58}$$

By definition, the modified strain rate tensor in equation (3.41) has zero trace, giving the following additional constraint

$$\lambda_1 + \lambda_2 + \lambda_3 = 0. \tag{3.59}$$

Without any loss of generality it can be assumed that $\lambda_1 > \lambda_2 > \lambda_3$. Similar to the analysis of Durbin [15], the worst case scenario is given by setting $\lambda_2 = 0$. Under this condition the eigenvalues of the rate of strain tensor become

$$\lambda_1 = \sqrt{\frac{\eta_1}{2}}, \qquad \lambda_3 = -\sqrt{\frac{\eta_1}{2}}. \tag{3.60}$$

Equation (3.60) is used in equation (3.58) as well as the constitutive relation (3.43), and finally in inequality (3.57) to find the three conditions that must be satisfied to

guarantee realizability

$$-\frac{1}{3} \leq \beta_1 \sqrt{\frac{\eta_1}{2}} + \frac{1}{6}\eta_1\beta_3 \leq \frac{2}{3}, \tag{3.61a}$$

$$-\frac{1}{3} \leq -\frac{1}{3}\eta_1\beta_3 \leq \frac{2}{3}, \tag{3.61b}$$

$$-\frac{1}{3} \leq -\beta_1 \sqrt{\frac{\eta_1}{2}} + \frac{1}{6}\eta_1\beta_3 \leq \frac{2}{3}. \tag{3.61c}$$

Figures 3.10 – 3.11 display constraints (3.61a) – (3.61c) for a representative gradient Mach number. The present model is entirely realizable as all closures fall within the realizable region. Although not shown here, many different values of M_g were also plotted. No realizability violations were found within the parameter range $0 \leq M_g \leq 3.05$. For locations in a computation where $M_g \geq 3.05$, it is recommended to set the pressure-strain correlation coefficients at the values they attain when $M_g = 3.05$. Figure 3.12 shows that the standard $k-\varepsilon$ model predicts unphysical Reynolds stresses for large values of mean deformation regardless of the chosen value for the C_μ closure constant.

For computational and numerical simplicity, in practice many algebraic models are simplified to use only the linear S_{ij} term. Unfortunately the resulting truncated model is only fully realizable in the range $0 \leq M_g \leq 0.6$. To expand the useful gradient Mach number range of the linear model the following simple realizability truncation is proposed, (similar to Durbin [15])

$$\beta_1 = \max\left\{\beta_1^{\text{ARSM}}, \frac{-1}{3\sqrt{\eta_1/2}}\right\}. \tag{3.62}$$

Equation (3.62) is only required when using the truncated linear ARSM, i.e. $b_{ij} = \beta_1 S_{ij}$. It is important to note that the three term model in equation (3.43) is fully

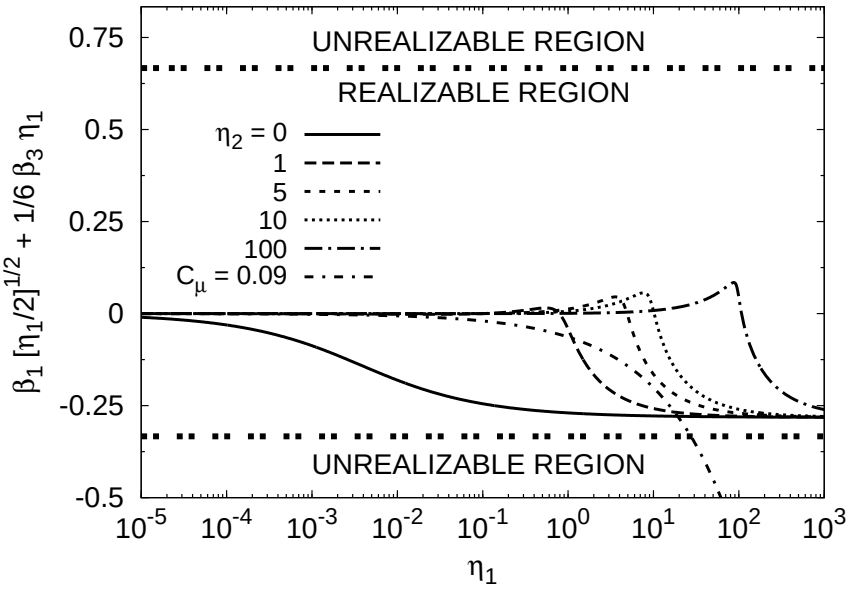

(a) Equation (3.61a) at $M_g = 1.5$

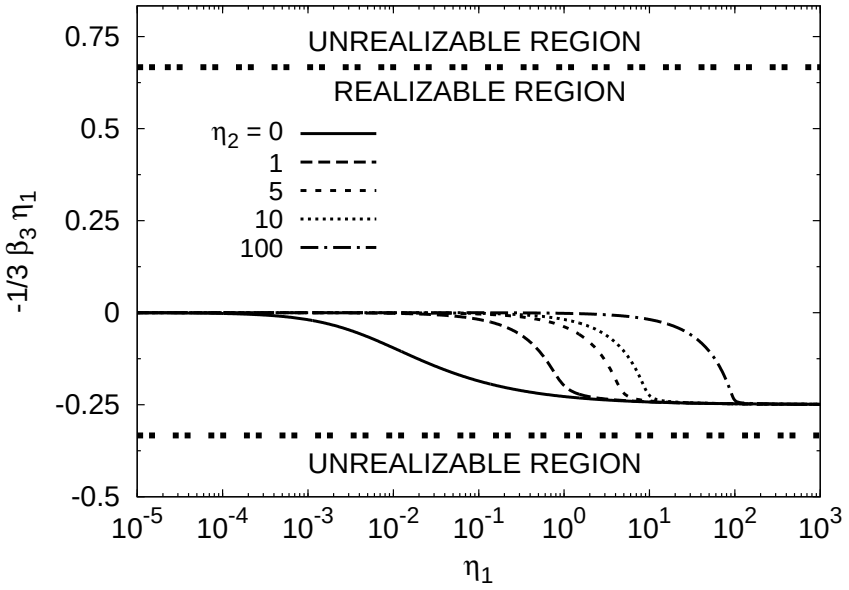

(b) Equation (3.61b) at $M_g = 1.5$

Figure 3.10: Realizability constraint equations (3.61a) and (3.61b) for $M_g = 1.5$.

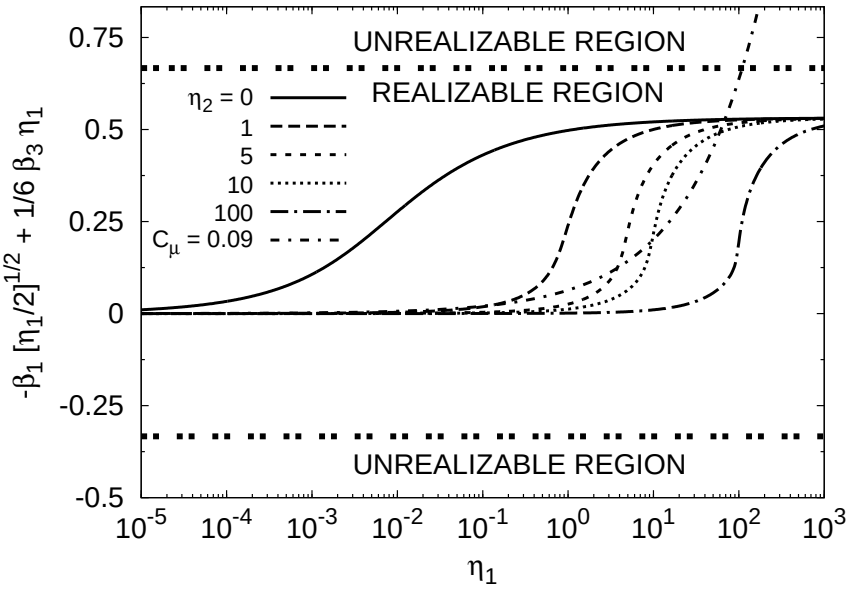

Figure 3.11: Realizability constraint equation (3.61c) for $M_g = 1.5$.

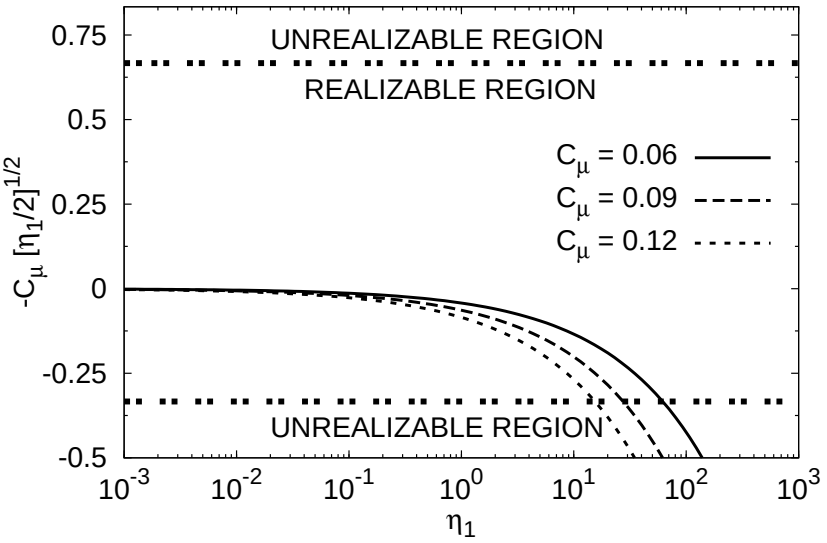

Figure 3.12: Realizability constraint equation (3.61) for standard $k-\varepsilon$ and different values of C_μ.

realizable as shown in figures 3.10 and 3.11. The indication is clearly that the loss of non-linear constitutive physics leads to a realizability violation. However, non-linear models can lead to numerical stiffness. In the following section, both the linear and non-linear models are tested in homogeneous shear and compared with the DNS of Sarkar [71]. However, in inhomogeneous flow computations the linear ARSM is used for the sake of computational ease. The Reynolds stress anisotropy is then calculated in the post-processing step using the fully non-linear constitutive relationship.

3.5 Preliminary validation: compressible homogeneous shear

The DNS of compressible homogeneous shear performed by Sarkar [71], provides full time history evolution of the anisotropy tensor b_{ij}, normalized dilatation X_ε, and normalized growth rates of turbulent kinetic energy Λ, for four cases of different initial gradient Mach number. Each simulation, characterized by the initial gradient Mach number, leads to a different set of asymptotic values. The long time behavior of the five quantities b_{11}, b_{22}, b_{12}, X_ε and Λ have been used to calibrate the five coefficients of the pressure-strain correlation C_1, C_3, C_4, C_5, and C_P based on the initial gradient Mach number of each DNS case, for details see Gomez & Girimaji [34]. Sarkar's DNS spans the range $0.51 \leq M_{g_0} \leq 3.05$. The normalized quantities X_ε and Λ are defined as

$$X_\varepsilon = \frac{\overline{\rho}\varepsilon - \Pi}{\overline{\rho}P}, \quad \Lambda = \frac{1}{Sk}\frac{dk}{dt}. \tag{3.63}$$

In this section the evolution of b_{11}, b_{22}, b_{12}, X_ε and Λ is computed and compared with the DNS results of Sarkar [71]. Both the full three term ARSM, as well as the linearized ARSM are used.

In pure homogeneous shear the turbulent kinetic energy, and dissipation rate

equations reduce to

$$\overline{\rho}\frac{Dk}{Dt} = \overline{\rho}P - \overline{\rho}\varepsilon + \Pi = \overline{\rho}P\left(1 - C_P\right) - \overline{\rho}\varepsilon, \tag{3.64}$$

and

$$\overline{\rho}\frac{D\varepsilon}{Dt} = C_{\varepsilon_1}\overline{\rho}\frac{\varepsilon}{k}P - C_{\varepsilon_2}\overline{\rho}\frac{\varepsilon^2}{k}. \tag{3.65}$$

The velocity gradient tensor for homogeneous shear is

$$\frac{\partial \tilde{u}_i}{\partial x_j} = S\delta_{i1}\delta_{j2}, \tag{3.66}$$

and the modified rate of strain and rotation rate tensors are

$$S^*_{ij} = \begin{bmatrix} 0 & S/2 & 0 \\ S/2 & 0 & 0 \\ 0 & 0 & 0 \end{bmatrix}, \quad W^*_{ij} = \begin{bmatrix} 0 & S/2 & 0 \\ -S/2 & 0 & 0 \\ 0 & 0 & 0 \end{bmatrix}, \tag{3.67}$$

respectively.

Equations (3.64) and (3.65) are integrated using a fourth order Runge–Kutta–Fehlberg numerical scheme. The initial conditions match those found in Sarkar's DNS: isotropic Reynolds stresses, gradient Mach number, turbulent Mach number, and Sk/ε. The ARSM enters through the computation of the production to dissipation ratio, which for homogeneous shear is given by

$$\frac{P}{\varepsilon} = \frac{-2Skb_{12}}{\varepsilon}. \tag{3.68}$$

The results are shown in figures 3.13 – 3.16 for the full three term and linear ARSM respectively. As expected, the only difference between the two models is the anisotropy

shown in figures 3.13(a) and 3.15(a). Both models show reasonable agreement with the long time behavior of DNS. Although it would be trivial to modify the pressure-strain correlation coefficients to achieve better agreement with DNS, instead the pressure-strain correlation developed in Gomez & Girimaji [34] is used without modification. Figures 3.13 – 3.16 show that for shear dominated flows one is at liberty to choose either the full ARSM or simpler linear ARSM. It is important to keep in mind that whereas the full ARSM is realizable, the linear ARSM requires the realizability correction in equation (3.62).

3.6 Model validation for inhomogeneous flow

3.6.1 Numerical implementation

The present compressible ARSM is implemented into the ANSYS® FLUENT Release 13.0 software package. Closure model modifications are implemented into the solver via user defined functions, UDFs. The ANSYS® FLUENT code [2] solves evolution equations for mean mass (3.69), momentum (3.70), and energy (3.71), along with the $k-\varepsilon$ equations (3.73) – (3.74), modified to include the effect of the pressure-dilatation model, equation (3.30). For the present calculations only the linear term β_1 is used in the anisotropy tensor. The turbulent viscosity is calculated using equation (3.75). The same pressure-strain correlation coefficients that have been calibrated with DNS [34] are used, and are shown in figure 3.2. The Reynolds stresses are found using equation (3.78). In the calculations, air is used as the working fluid, and the molecular viscosity is computed using Sutherland's Law [85], equation (3.76). Additional closure constants applicable to all models are given in equations (3.77) and (3.79).

$$\frac{\partial \overline{\rho}}{\partial t} + \frac{\partial}{\partial x_i}(\overline{\rho}\tilde{u}_i) = 0, \tag{3.69}$$

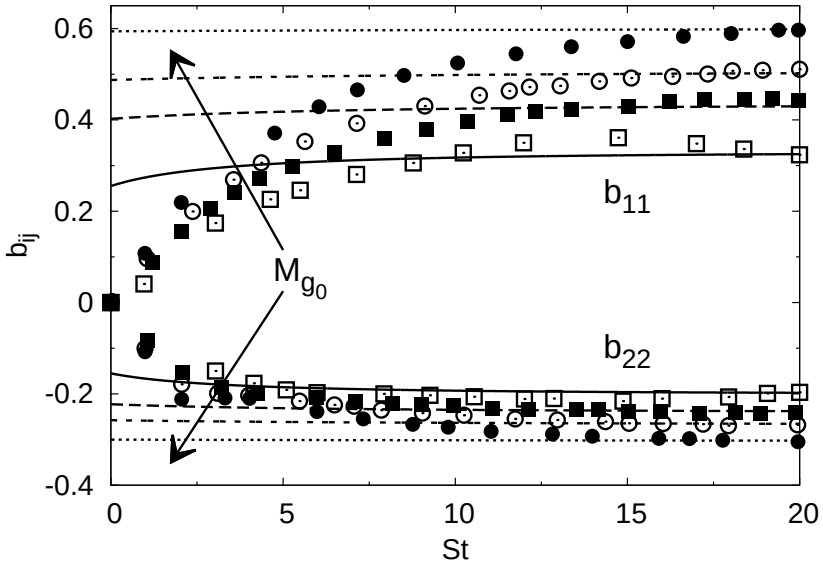

(a)

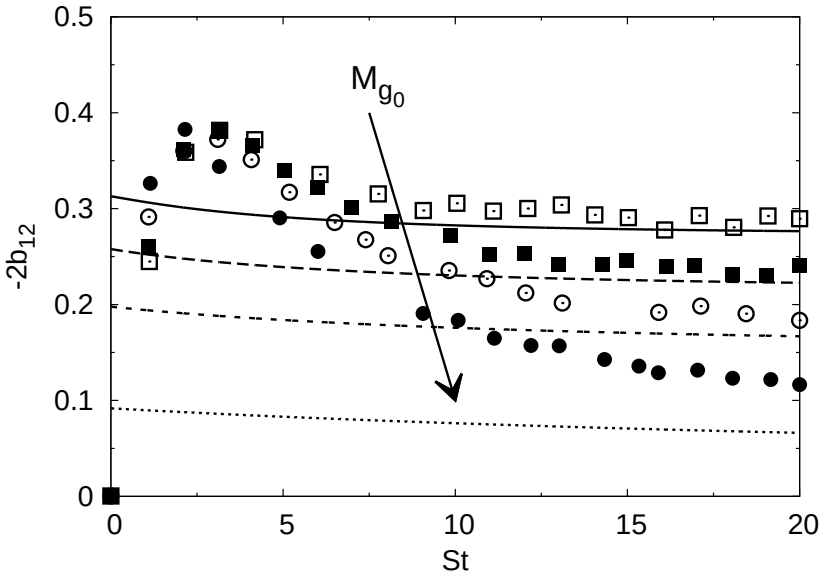

(b)

Figure 3.13: Three term ARSM preliminary validation with the compressible homogeneous shear DNS of Sarkar [71], arrows point towards increasing initial gradient Mach number. (a) b_{11} and b_{22}, and (b) b_{12}. For legend see following figure.

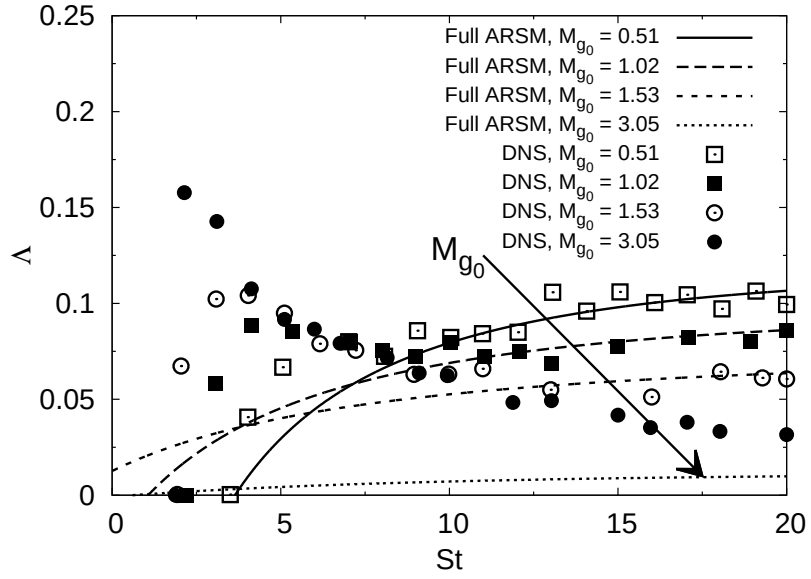

(a)

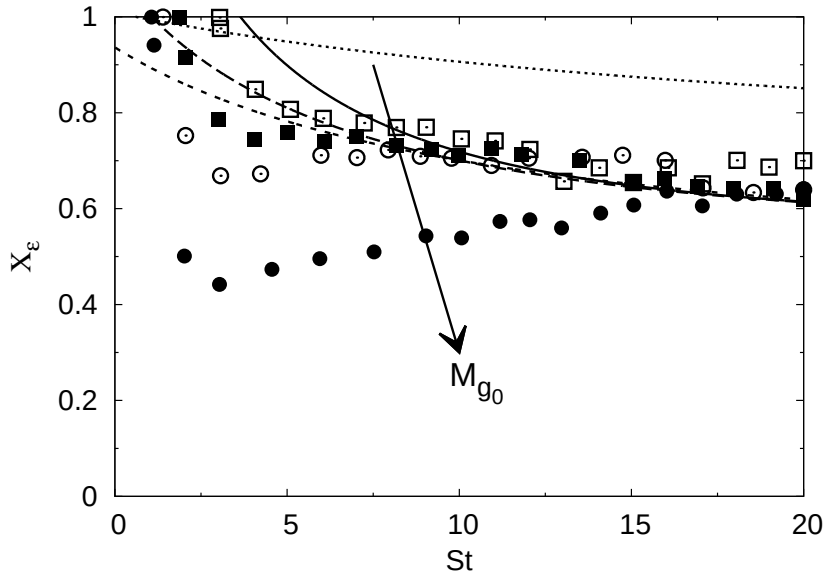

(b)

Figure 3.14: Three term ARSM preliminary validation with the compressible homogeneous shear DNS of Sarkar [71], arrows point towards increasing initial gradient Mach number. (a) Λ, and (b) X_ε.

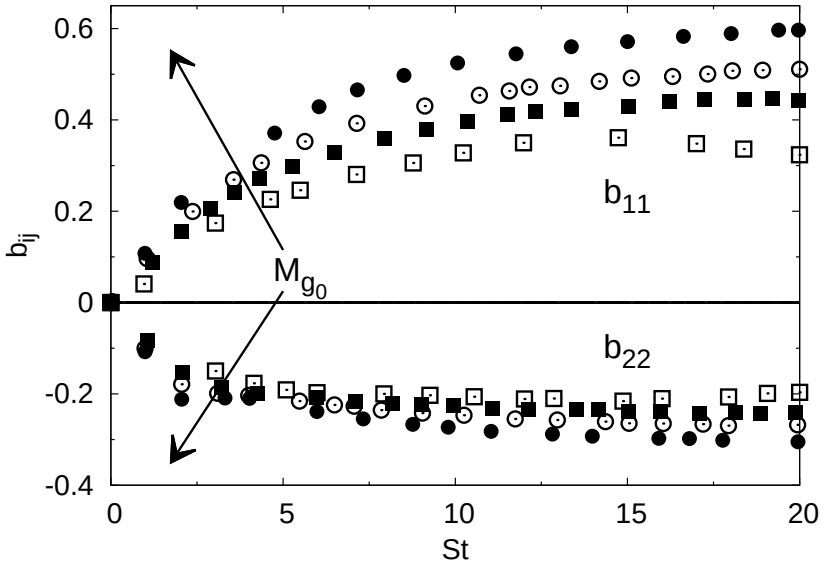

(a)

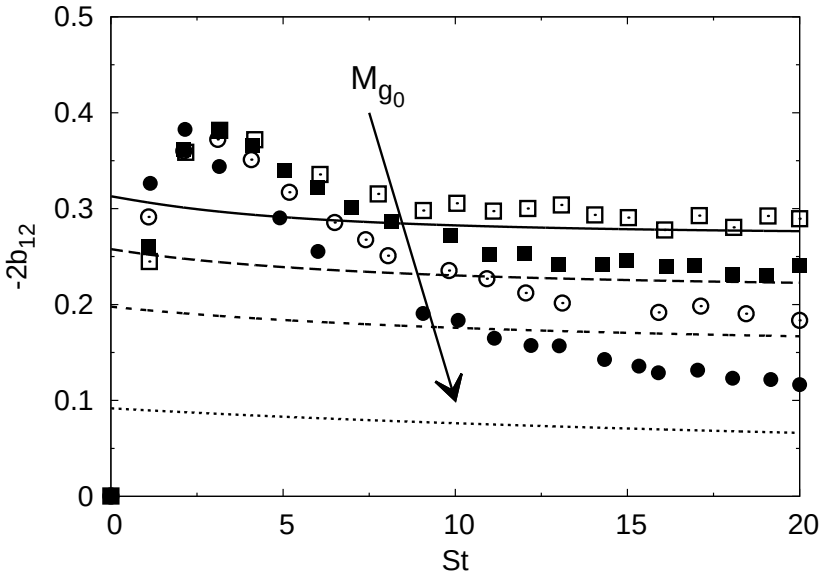

(b)

Figure 3.15: Linear ARSM preliminary validation with the compressible homogeneous shear DNS of Sarkar [71], arrows point towards increasing initial gradient Mach number. (a) b_{11} and b_{22}, and (b) b_{12}. For legend see following figure.

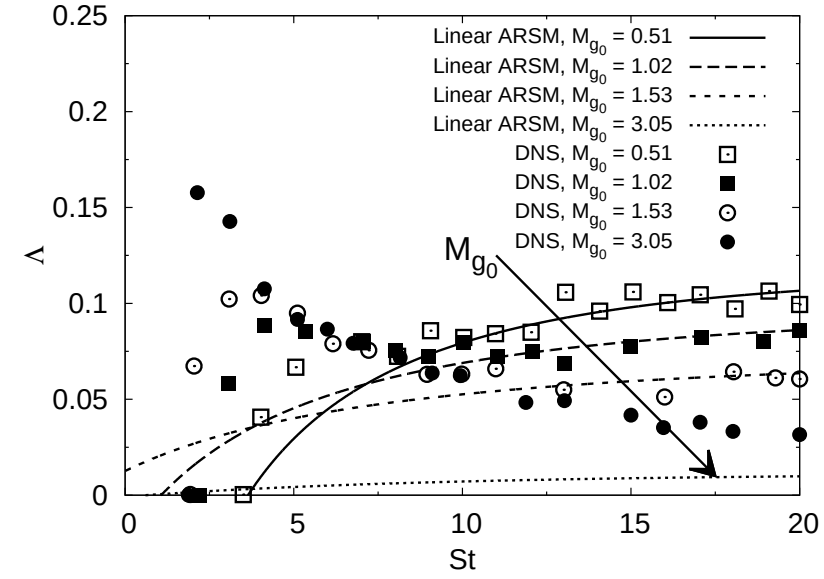

(a)

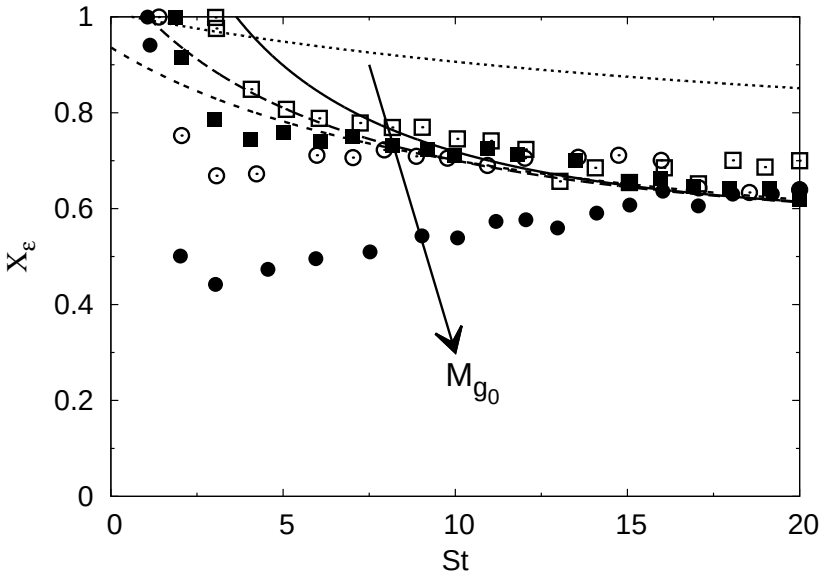

(b)

Figure 3.16: Linear ARSM preliminary validation with the compressible homogeneous shear DNS of Sarkar [71], arrows point towards increasing initial gradient Mach number. (a) Λ, and (b) X_ε.

$$\frac{\partial}{\partial t}(\overline{\rho}\tilde{u}_i) + \frac{\partial}{\partial x_j}(\overline{\rho}\tilde{u}_i\tilde{u}_j) = -\frac{\partial \overline{p}}{\partial x_i} + \frac{\partial}{\partial x_j}\left[\mu\left(\frac{\partial \tilde{u}_i}{\partial x_j} + \frac{\partial \tilde{u}_j}{\partial x_i} - \frac{2}{3}\frac{\partial \tilde{u}_k}{\partial x_k}\delta_{ij}\right)\right] - \frac{\partial}{\partial x_j}\left(\overline{\rho}R_{ij}\right), \tag{3.70}$$

$$\frac{\partial}{\partial t}(\overline{\rho}E) + \frac{\partial}{\partial x_i}\left[\tilde{u}_i\left(\overline{\rho}E + \overline{p}\right)\right] = \frac{\partial}{\partial x_j}\left[\left(\kappa + \frac{c_p\mu_t}{Pr_t}\right)\frac{\partial \tilde{T}}{\partial x_j} + \tilde{u}_i\left(\tau_{ij}\right)_{\text{eff}}\right], \quad E = \tilde{h} - \frac{\overline{p}}{\overline{\rho}} + \frac{\tilde{u}_i\tilde{u}_i}{2}, \tag{3.71}$$

$$\left(\tau_{ij}\right)_{\text{eff}} = \mu_{\text{eff}}\left(\frac{\partial \tilde{u}_i}{\partial x_j} + \frac{\partial \tilde{u}_j}{\partial x_i}\right) - \frac{2}{3}\mu_{\text{eff}}\frac{\partial \tilde{u}_k}{\partial x_k}\delta_{ij}, \tag{3.72}$$

$$\frac{\partial}{\partial t}(\overline{\rho}k) + \frac{\partial}{\partial x_i}(\overline{\rho}k\tilde{u}_i) = \frac{\partial}{\partial x_j}\left[\left(\mu + \frac{\mu_t}{\sigma_k}\right)\frac{\partial k}{\partial x_j}\right] + \overline{\rho}P\left(1 - C_P\right) - \overline{\rho}\varepsilon, \tag{3.73}$$

$$\frac{\partial}{\partial t}(\overline{\rho}\varepsilon) + \frac{\partial}{\partial x_i}(\overline{\rho}\varepsilon\tilde{u}_i) = \frac{\partial}{\partial x_j}\left[\left(\mu + \frac{\mu_t}{\sigma_\varepsilon}\right)\frac{\partial \varepsilon}{\partial x_j}\right] + C_{\varepsilon_1}\overline{\rho}\frac{\varepsilon}{k}P - C_{\varepsilon_2}\overline{\rho}\frac{\varepsilon^2}{k}, \tag{3.74}$$

$$\mu_t = \frac{\overline{\rho}C_\mu k^2}{\varepsilon} = \frac{-\overline{\rho}\beta_1 k^2}{\varepsilon}, \quad \mu_{\text{eff}} = \mu + \mu_t, \tag{3.75}$$

$$\mu = \mu_0\left(\frac{\tilde{T}}{T_0}\right)^{3/2}\left(\frac{T_0 + S_0}{\tilde{T} + S_0}\right), \tag{3.76}$$

$$\mu_0 = 1.716\text{e-}5\ [\text{kg/(m-s)}], \quad T_0 = 273.11\ [\text{K}], \quad S_0 = 110.56\ [\text{K}], \tag{3.77}$$

$$R_{ij} = 2k\left(\beta_1 S_{ij} + \frac{1}{3}\delta_{ij}\right), \tag{3.78}$$

$$C_{\varepsilon_1} = 1.44, \quad C_{\varepsilon_2} = 1.83, \quad \sigma_k = 0.82, \quad \sigma_\varepsilon = 1.0, \quad Pr_t = 0.85. \tag{3.79}$$

Standard $k-\varepsilon$ models employ the Boussinesq approximation to calculate the Reynolds stresses

$$R_{ij} = 2k\left(-C_\mu S_{ij} + \frac{1}{3}\delta_{ij}\right), \quad C_\mu = 0.09. \tag{3.80}$$

3.6.2 Mixing-layer simulation

One of the biggest challenges in compressible turbulence closure modeling is the ability to capture the reduced mixing-layer growth rates observed experimentally by

Papamoschou & Roshko [58], Goebel & Dutton [33], Clemens & Mungal [11], and many others [10, 35, 42, 69].

To assess the relative performance of the compressible ARSM (C – ARSM) against standard models calculations are performed with the following four turbulence models:

1. C – ARSM: The present compressible algebraic model using only the linear term β_1.

2. I – ARSM: The incompressible algebraic model of Girimaji [25] using only the linear term β_1. This model is obtained by setting $C_k = C_{k_0}$, and $C_P = 0$.

3. $k-\varepsilon$: Standard two-equation model without the Sarkar et al. [72] compressibility correction.

4. $k-\varepsilon-S$: Standard two-equation model with the Sarkar et al. [72] compressibility correction.

The boundary conditions of the experiments of Goebel & Dutton [33] are matched as closely as possible to compare similarity profiles, mixing-layer spreading rates, and Reynolds stresses. Three grids are studied to ensure grid convergence. The coarse grid has 24,000 cells (300 by 80), the medium grid 48,000 cells (400 by 120), and the fine grid 96,000 cells (600 by 160). Figures 3.17 and 3.18 show representative results from the grid study. The mean square error is plotted in figure 3.19 and is computed by using

$$MSE = \frac{1}{n}\sum_{i=1}^{n}\left(\tilde{u}_{1_i} - \tilde{u}^*_{1_i}\right)^2, \tag{3.81}$$

where $\tilde{u}^*_1$ is the streamwise velocity of the finest grid. The medium grid is found to provide adequate resolution due to the negligible difference between the medium and fine grid results.

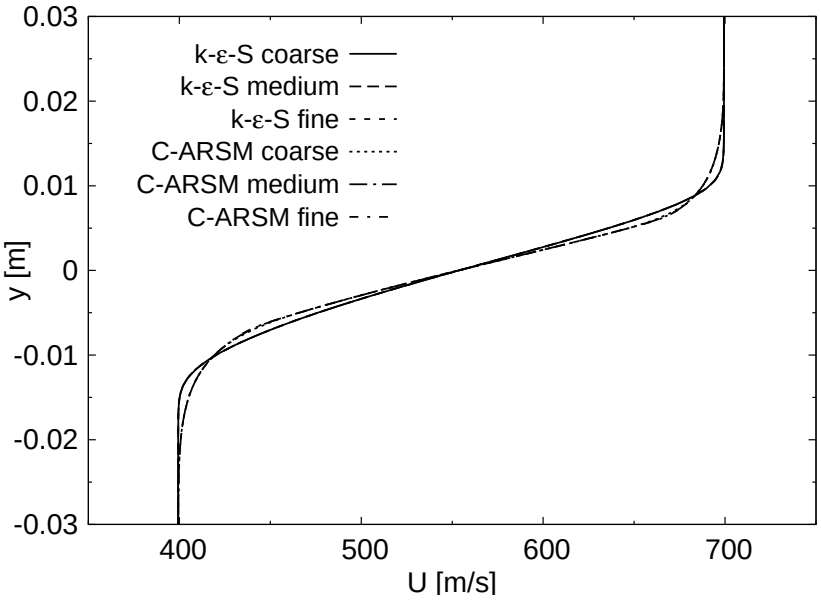

(a) Streamwise velocity profile.

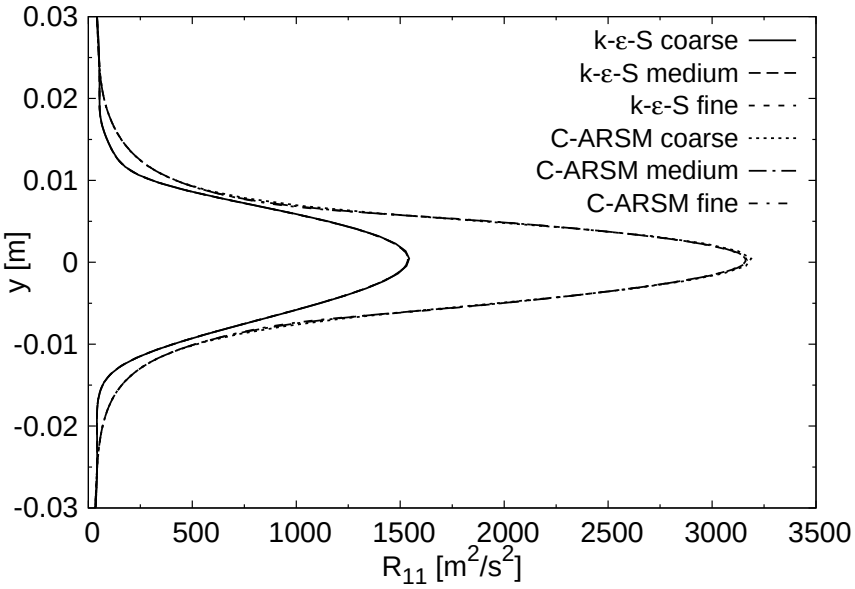

(b) Streamwise Reynolds stress.

Figure 3.17: ARSM mixing-layer grid convergence study. (a) Streamwise velocity profile, and (b) streamwise Reynolds stress.

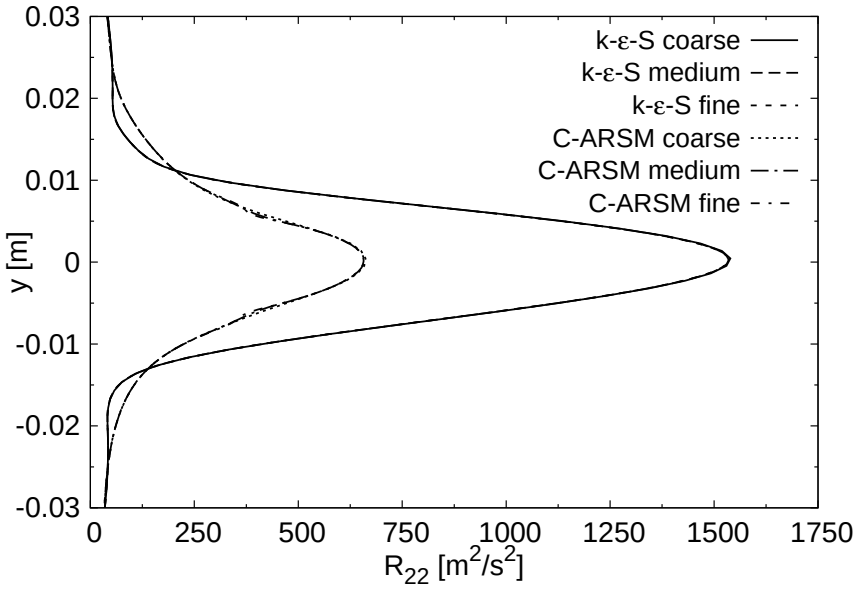

(a) Cross-stream Reynolds stress.

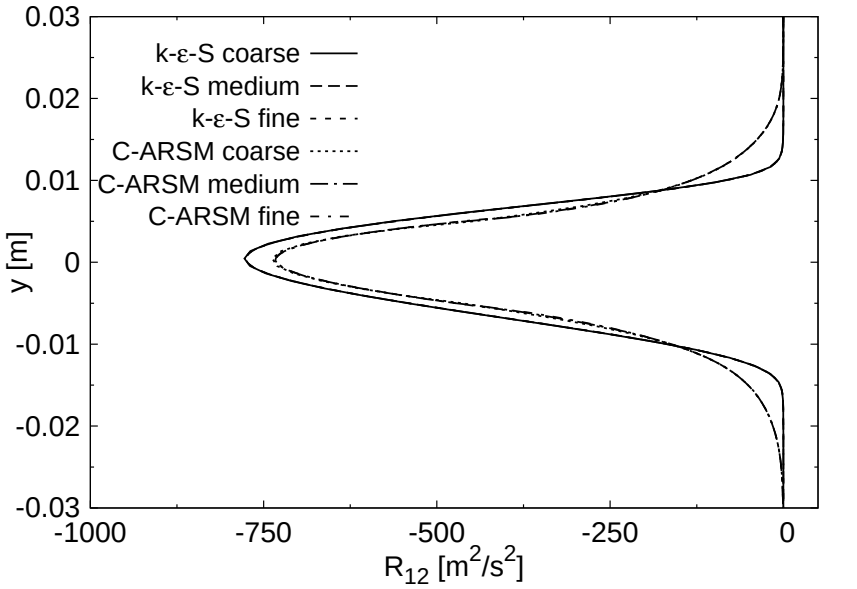

(b) Shear Reynolds stress.

Figure 3.18: ARSM mixing-layer grid convergence study. (a) Cross-stream Reynolds stress, and (b) shear Reynolds stress.

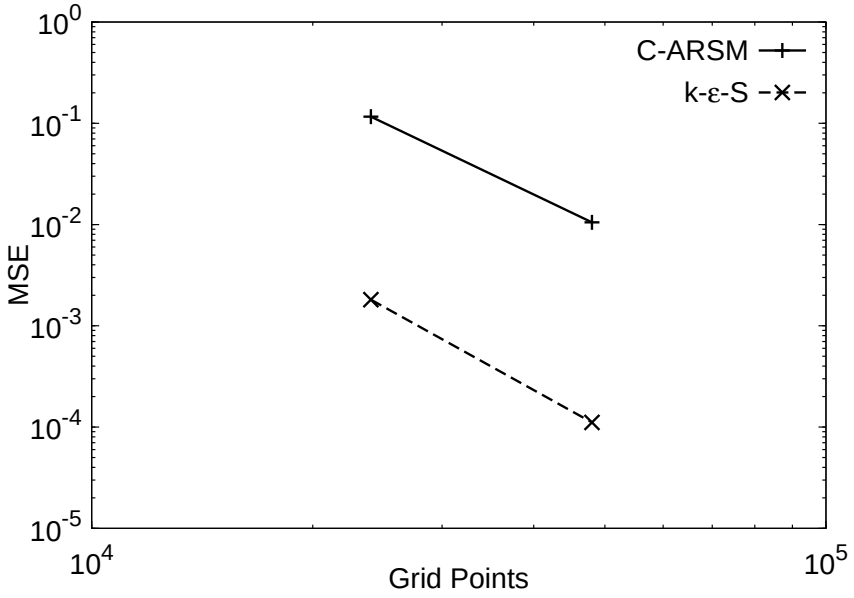

Figure 3.19: Mean square error of $\tilde{u}_1$ velocity.

The experimental setup of a two-dimensional mixing-layer consists of a channel with two incoming streams separated by a splitter plate. The top stream is labeled as primary and the lower as secondary. It is customary to choose the primary stream as the high-speed inlet. For the computations a rectangular domain downstream of the splitter plate is used to avoid any wall and sudden expansion effects. A schematic of the computational domain along with the boundary conditions is shown in figure 3.20. The grid is 0.3 meters long in the streamwise direction and 0.1 meters high in the cross-stream direction. Hyperbolic tangent and piecewise cubic polynomial functions are used to set the boundary conditions at the inlet to avoid sharp gradients and promote a fully developed self similar flow. The flow becomes self similar between 0.1 and 0.2 meters for all cases.

Goebel & Dutton [33] characterize the supersonic mixing-layer with relative Mach number, defined as

$$M_r \equiv \frac{U_1 - U_2}{(a_1 + a_2)/2} = \frac{\Delta U}{\bar{a}}, \tag{3.82}$$

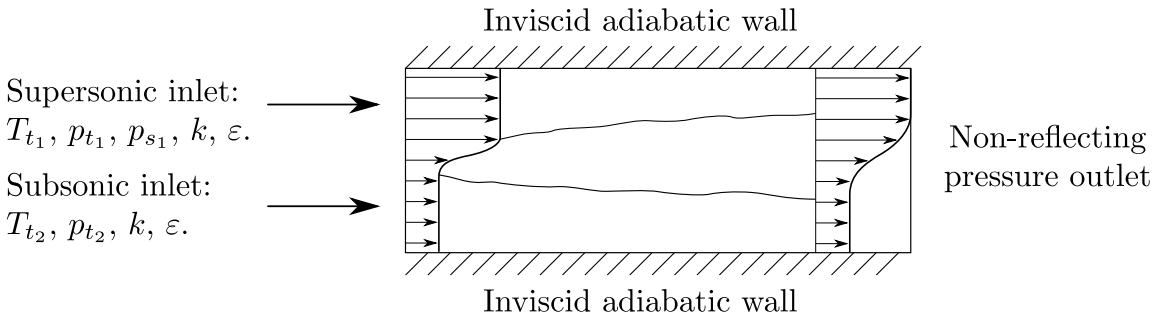

Figure 3.20: Two dimensional supersonic mixing-layer boundary conditions.

Case	M_r	M_1	M_2	U_1	U_2	T_{t_1}	T_{t_2}	p_{t_1}	p_{t_2}	p_{s_1}
C1	0.40	2.01	1.38	515	404	295	295	365.6	142.3	46
C2	0.91	1.91	1.36	700	399	578	295	333.4	147.4	49
C3	1.37	1.96	0.27	499	92	285	285	389.7	55.8	53
C4	1.73	2.35	0.30	616	100	360	290	486.8	38.3	36
C5	1.97	2.27	0.38	830	131	675	300	381.8	35.4	32

Table 3.2: Supersonic mixing-layer inlet conditions. Dimensional quantities are in [m/s], [K], and [kPa] for velocity, temperature, and pressure respectively.

where the subscripts 1 and 2 refer to the primary and secondary streams respectively, U is the mean inlet velocity, and $\bar{a}$ is the average inlet speed of sound. Papamoschou & Roshko [58] observed that overall compressibility effects are found mainly between $0.5 \leq M_r \leq 2.0$. Goebel & Dutton's experiments span this relative Mach number range going from 0.4 to 1.97. Here results are presented for five of their cases: $M_r = 0.40, 0.91, 1.37, 1.73,$ and 1.97, which in the following will be referred to as C1, C2, C3, C4, and C5 respectively. The inlet boundary conditions for each case are given in table 3.2, where T_t is total temperature, p_t total pressure, and p_s static pressure. Every attempt was made to match as best as possible the boundary conditions reported by Goebel & Dutton [33]. Experience indicates that for the parameter range in this study, there is no significant change in spreading rates or peak values of normalized Reynolds stresses when using either far-field or inviscid wall boundary

conditions. The effect of manipulating the angle of the upper and lower walls has been studied by Cottrell and Plesniak [12]. Similar conclusions are reached in that study.

Referring back to figure 3.1 it can be immediately observed that there is a significant spread of experimental mixing-layer spreading rates. The Langley [42] curve appears to mark an upper limit, whereas the experiments of Hall, et al. [35] demark the lower limit. As the experiments of Goebel & Dutton [33] fall in the middle of these two limits they constitute a good data set to benchmark the performance of compressible turbulence models.

Figures 3.21 – 3.30 compare streamwise velocity similarity profiles, normalized streamwise Reynolds stresses σ_u, normalized cross-stream Reynolds stresses σ_v, and normalized shear Reynolds stresses between the $k-\varepsilon$, $k-\varepsilon-S$, I$-$ARSM, and C$-$ARSM models with the experiments of Goebel & Dutton [33]. In these figures b is the mixing-layer thickness defined as the transverse distance between locations where the mean streamwise velocity is $U_1 - 0.1\Delta U$ and $U_2 + 0.1\Delta U$, where $\Delta U = U_1 - U_2$. The y coordinate of the mixing-layer centerline is y_0. The standard deviations of the Reynolds stresses are defined as

$$\sigma_u = \sqrt{R_{11}}, \qquad \sigma_v = \sqrt{R_{22}}. \tag{3.83}$$

Table 3.3 shows a representative value for the Reynolds number at the self-similar locations where data is taken from the computations. This Reynolds number is based on velocity difference and mixing-layer thickness

$$Re_b = \frac{\overline{\rho}\Delta U b}{\overline{\mu}}. \tag{3.84}$$

	C1	C2	C3	C4	C5
Re_b (10^5)	1.0	1.7	4.0	3.6	2.0

Table 3.3: Reynolds number based on mixing-layer thickness at self-similar locations.

3.6.3 Similarity profiles

Figures 3.21(a), 3.23(a), 3.25(a), 3.27(a), and 3.29(a) compare the mean streamwise velocity similarity profiles of the four turbulence models. Although not shown here, cross sections at multiple streamwise locations were plotted to ensure that the computed flows were fully self similar. All models adequately capture the experimental similarity profile in all five cases.

3.6.4 Normal Reynolds stresses

Figures 3.21(b), 3.23(b), 3.25(b), 3.27(b), and 3.29(b) compare the normalized streamwise Reynolds stresses while figures 3.22(a), 3.24(a), 3.26(a), 3.28(a), and 3.30(a) compare the normalized cross-stream Reynolds stresses. For case C1, the C – ARSM and I – ARSM computations yield almost identical results. This behavior is expected since for this case compressibility effects are only incipient. At this low relative Mach number the incompressible models perform reasonably well and offer good estimates of the mixing-layer spreading rates as seen in table 3.4. On the other hand for C3, C4, and C5 compressibility effects become apparent and the compressible and incompressible turbulence model predictions are no longer identical. The anisotropy σ_u/σ_v computed by each model is shown in figure 3.31. This figure shows how the C – ARSM is capable of capturing the trend of increasing anisotropy as the relative Mach number of the mixing-layer increases. In contrast the $k-\varepsilon$ and

$k-\varepsilon-S$, models employ an isotropic eddy viscosity and predict an anisotropy close to unity regardless of relative Mach number. The I – ARSM is in better agreement with experiments compared to the standard $k-\varepsilon$ models, however it too predicts an almost constant value of anisotropy.

3.6.5 Shear Reynolds stress

The computed Reynolds shear stresses are compared in figures 3.22(b), 3.24(b), 3.26(b), 3.28(b), and 3.30(b). For the same reasons discussed above, figure 3.22(b) shows that all four turbulence models yield nearly identical results at low relative Mach number. In contrast for C3, C4, and C5, figures 3.26(b), 3.28(b), and 3.30(b) show that the present C – ARSM and $k-\varepsilon-S$ on average agree better than their incompressible counterparts with the experimental Reynolds shear stress. The computed I – ARSM and $k-\varepsilon$ shear stress are consistently higher than those predicted by the C – ARSM and $k-\varepsilon-S$ models respectively. This result is to be expected due to the fact that both C – ARSM and $k-\varepsilon-S$ include compressibility effects, whereas I – ARSM and $k-\varepsilon$ are incompressible models. Capturing the reduction of Reynolds shear-stress at high relative Mach number is of paramount importance to be able to predict the reduced spreading rates observed in compressible mixing-layers.

3.6.6 Spreading rates

The mixing-layer spreading rates predicted by the different models are shown in table 3.4. Clearly the models differ substantially in this regard although their streamwise velocity similarity profiles are almost identical. It is seen that the C – ARSM and $k-\varepsilon-S$ perform best whereas the $k-\varepsilon$ model which does not include the Sarkar [72] correction performs worst. On the other hand, I – ARSM provides reasonable estimates of the mixing-layer spreading rates at low relative Mach number (C1 and C2), but falls well short of the mark at high relative Mach number (C3, C4,

Case	$k-\varepsilon$	$k-\varepsilon-S$	I$-$ARSM	C$-$ARSM	Experimental
C1	0.021	0.020	0.021	0.021	0.020
C2	0.037	0.033	0.035	0.031	0.038
C3	0.080	0.059	0.073	0.060	0.059
C4	0.072	0.053	0.072	0.055	0.050
C5	0.080	0.054	0.068	0.052	0.049

Table 3.4: Computed mixing-layer spreading rates, db/dx.

and C5). It is important to note that the stabilizing effect in C$-$ARSM comes from the present compressible pressure-strain correlation model whereas in the $k-\varepsilon-S$ model the mixing inhibition is due to dilatational dissipation. Figure 3.32 shows the normalized spreading rates of the ARSM calculations, where the incompressible spreading rates are estimated as [33, 58]

$$\left(\frac{db}{dx}\right)_i = 0.0825\frac{\left(1-r\right)\left(1+s^{1/2}\right)}{1+rs^{1/2}}, \quad r=\frac{U_2}{U_1}, \quad s=\frac{\rho_2}{\rho_1}. \tag{3.85}$$

C$-$ARSM and $k-\varepsilon-S$ capture the experimental trend the best. I$-$ARSM is adequate only for low relative Mach number. The $k-\varepsilon$ model fails even at moderate relative Mach number.

Overall, it is evident that C$-$ARSM captures the observed experimental behavior reasonably well. Importantly, the stabilizing effect in the closure is due to a high fidelity pressure-strain correlation model. A noteworthy feature of the present C$-$ARSM is that the compressible pressure-strain correlation model applied in the model derivation is obtained from calibration against homogeneous shear flow DNS calculations without modification, as can be seen in figure 3.2.

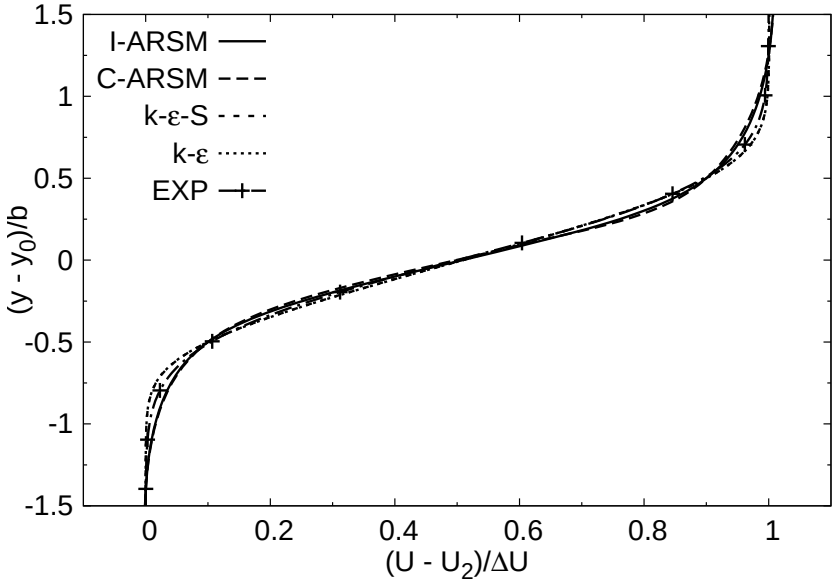

(a) Streamwise velocity similarity profile.

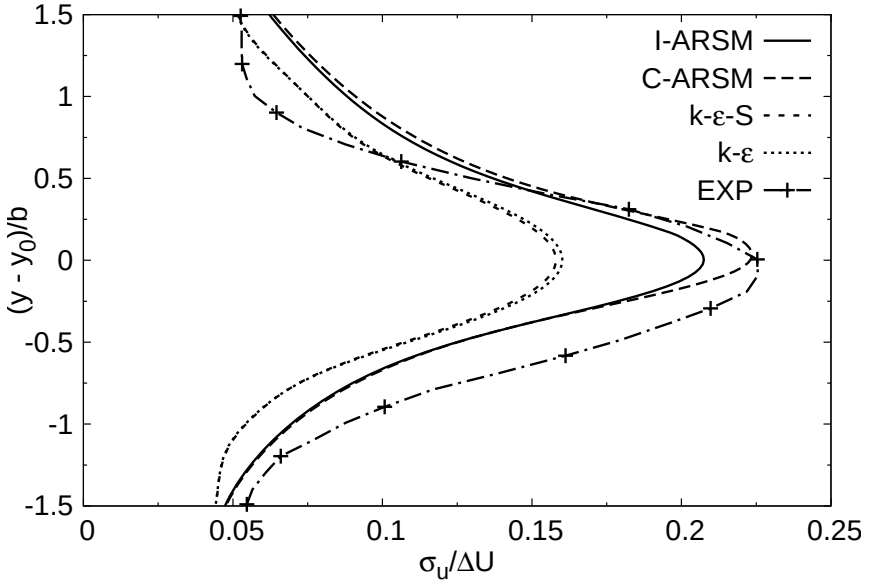

(b) Normalized streamwise Reynolds stress.

Figure 3.21: Plane mixing-layer results for C1, $M_r = 0.40$. (a) Normalized velocity profile, and (b) normalized streamwise Reynolds stress.

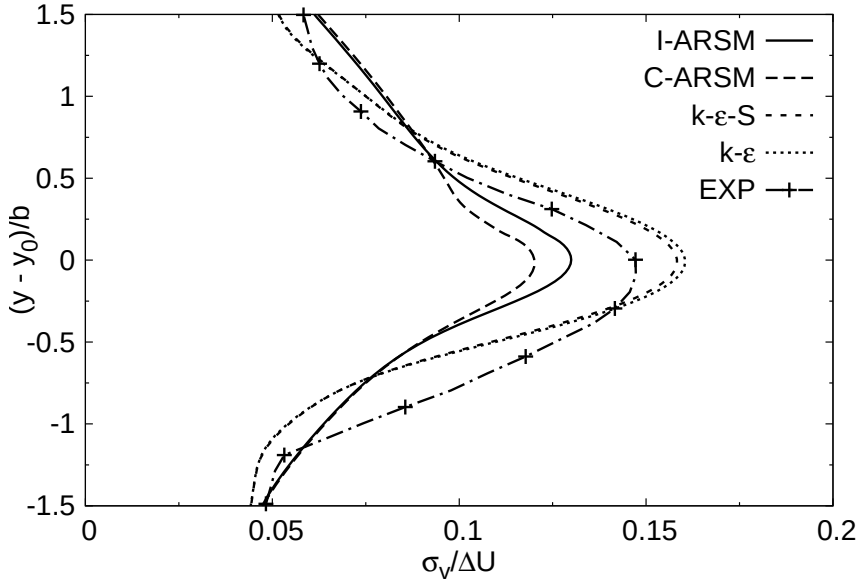

(a) Normalized cross-stream Reynolds stress.

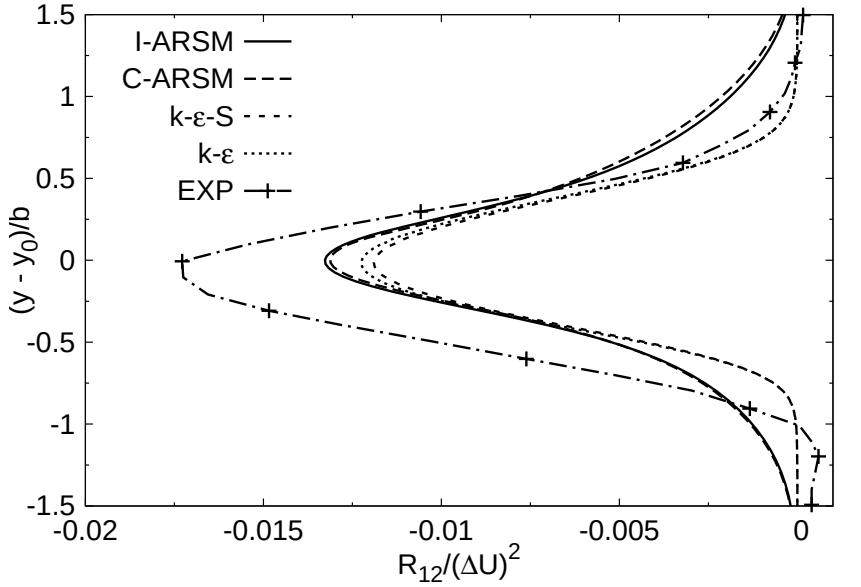

(b) Normalized shear Reynolds stress.

Figure 3.22: Plane mixing-layer results for C1, $M_r = 0.40$. (a) Normalized cross-stream Reynolds stress, and (b) normalized shear Reynolds stress.

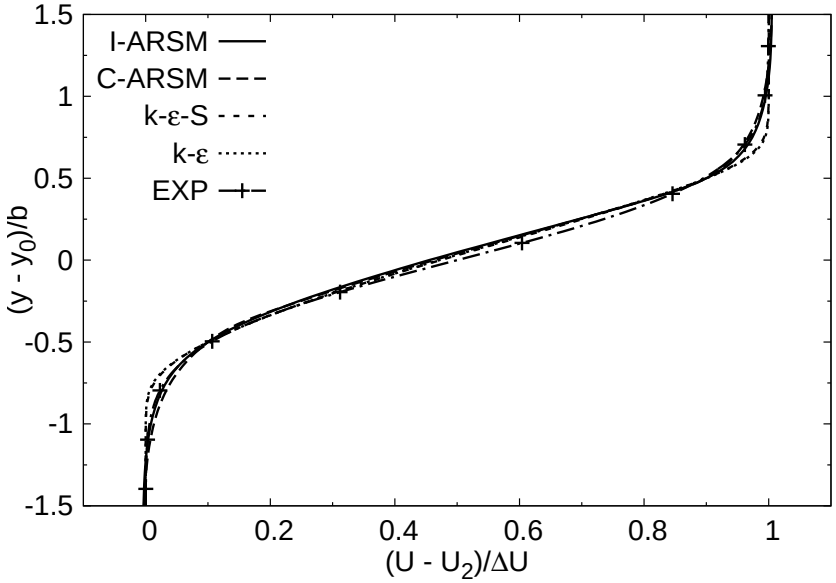

(a) Streamwise velocity similarity profile.

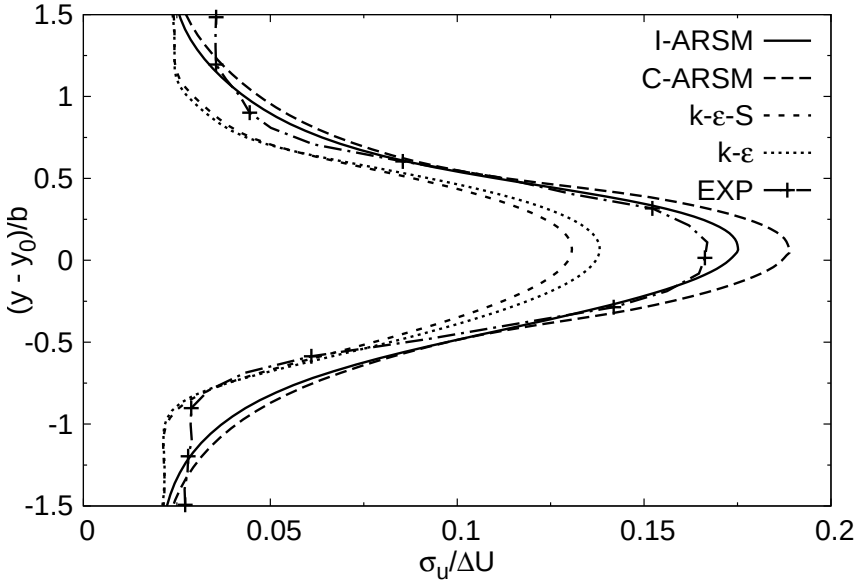

(b) Normalized streamwise Reynolds stress.

Figure 3.23: Plane mixing-layer results for C2, $M_r = 0.91$. (a) Normalized velocity profile, and (b) normalized streamwise Reynolds stress.

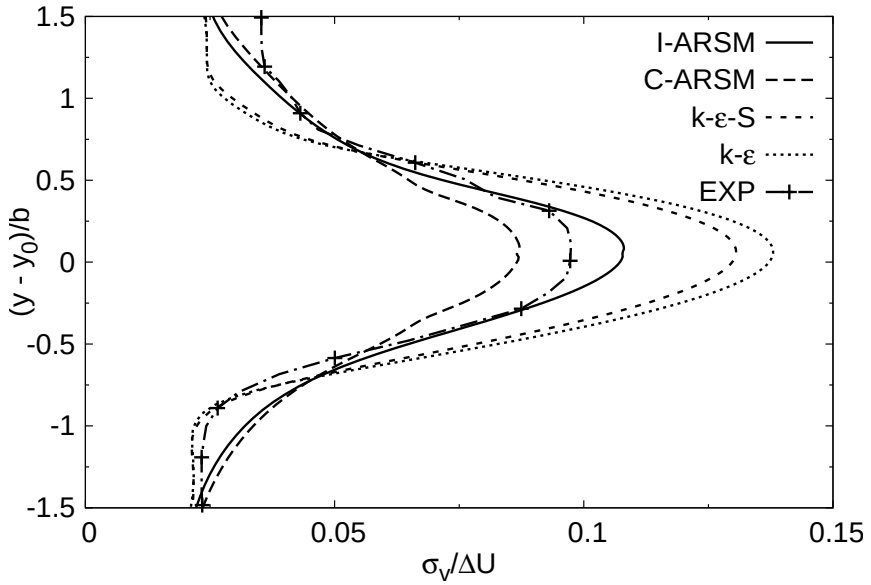

(a) Normalized cross-stream Reynolds stress.

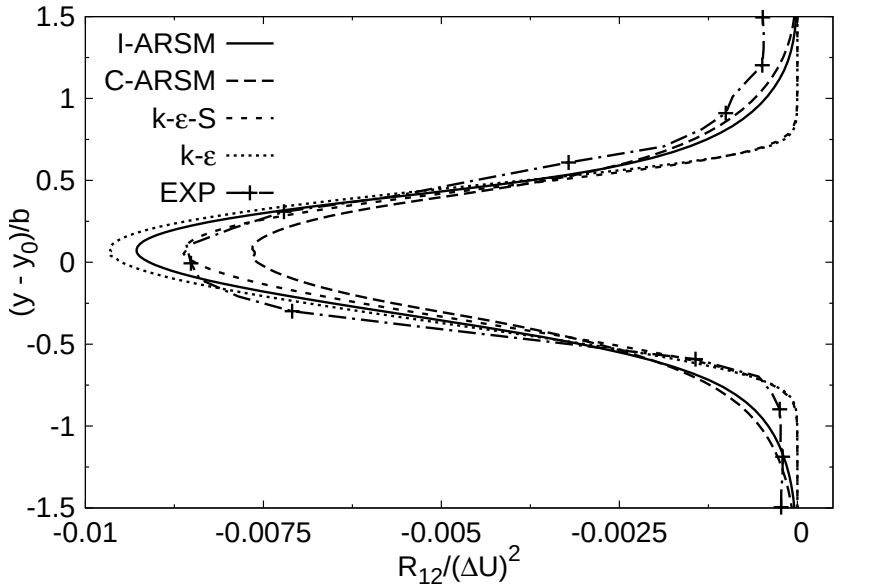

(b) Normalized shear Reynolds stress.

Figure 3.24: Plane mixing-layer results for C2, $M_r = 0.91$. (a) Normalized cross-stream Reynolds stress, and (b) normalized shear Reynolds stress.

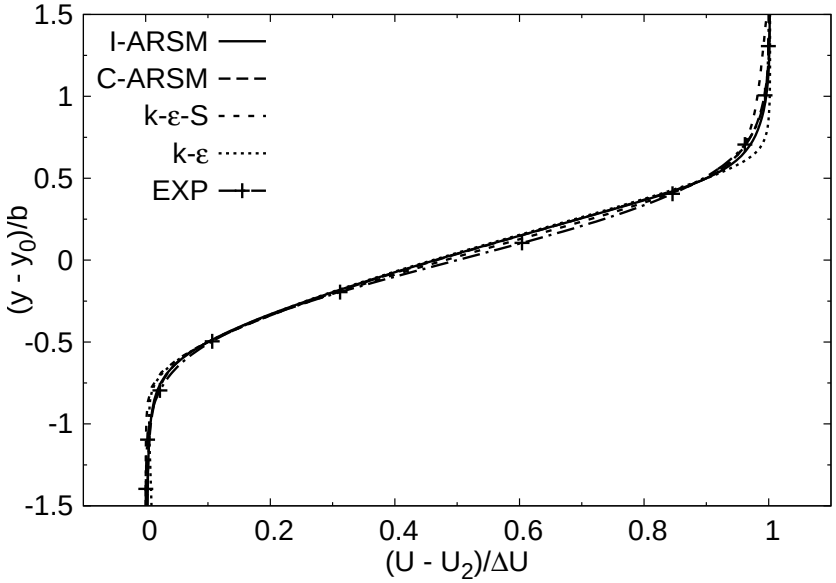

(a) Streamwise velocity similarity profile.

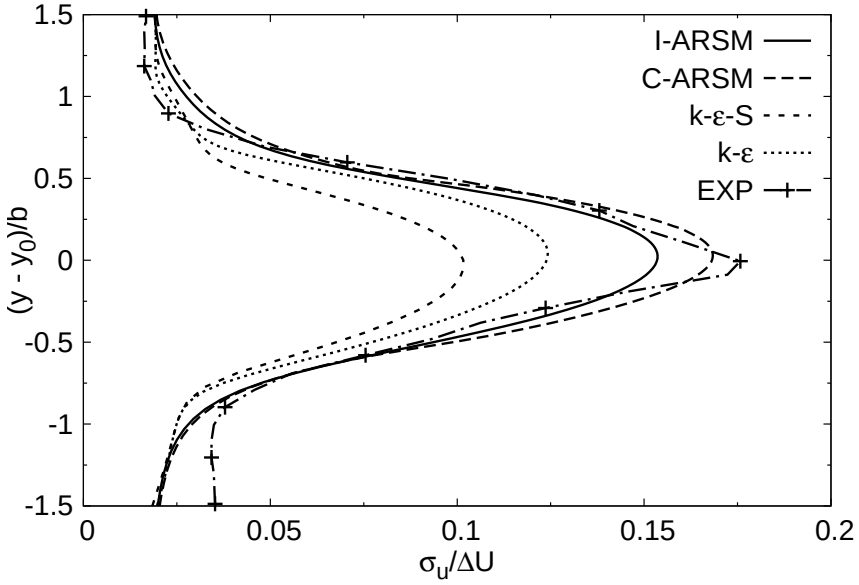

(b) Normalized streamwise Reynolds stress.

Figure 3.25: Plane mixing-layer results for C3, $M_r = 1.37$. (a) Normalized velocity profile, and (b) normalized streamwise Reynolds stress.

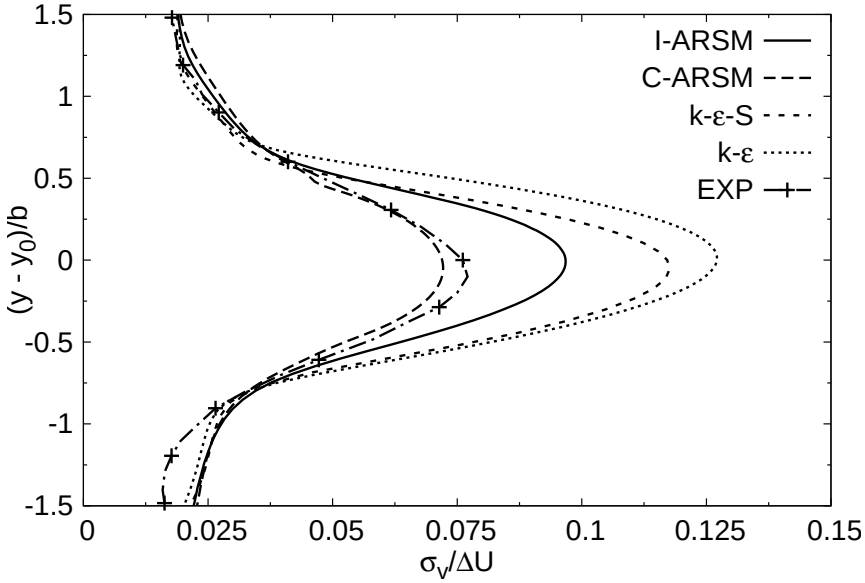

(a) Normalized cross-stream Reynolds stress.

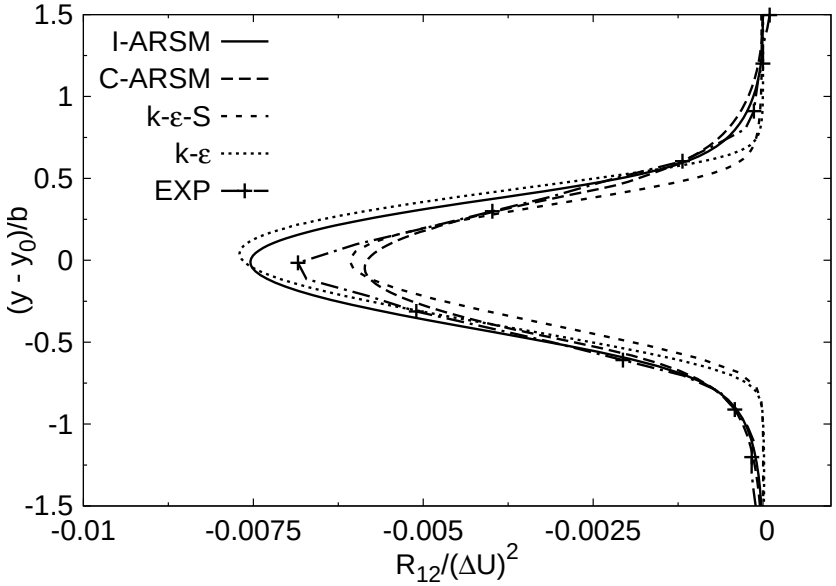

(b) Normalized shear Reynolds stress.

Figure 3.26: Plane mixing-layer results for C3, $M_r = 1.37$. (a) Normalized cross-stream Reynolds stress, and (b) normalized shear Reynolds stress.

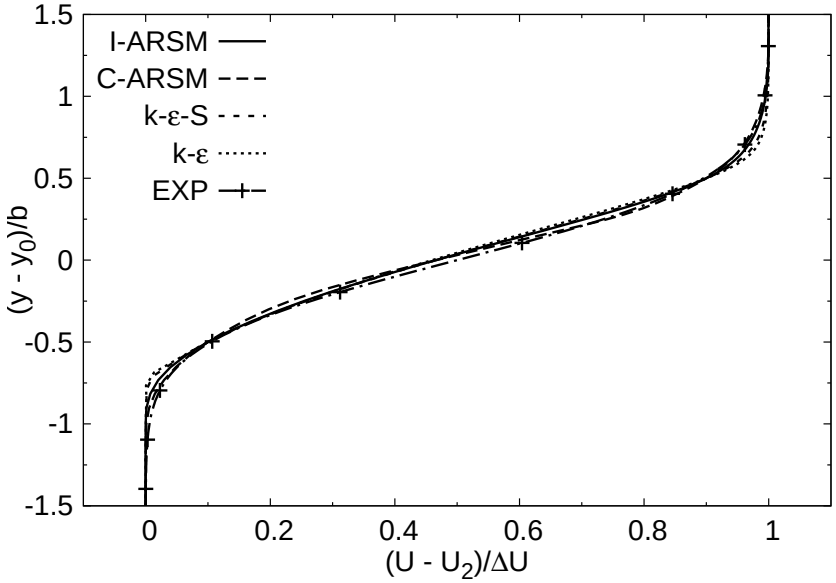

(a) Streamwise velocity similarity profile.

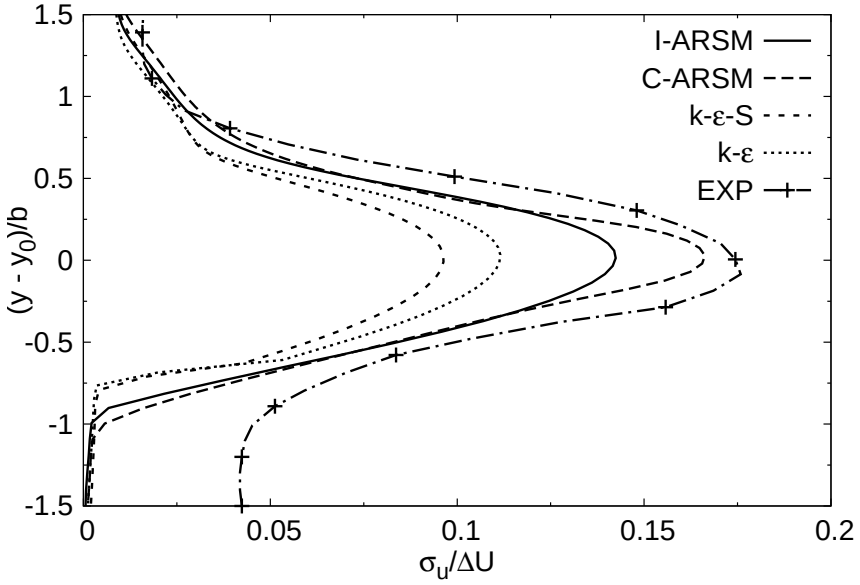

(b) Normalized streamwise Reynolds stress.

Figure 3.27: Plane mixing-layer results for C4, $M_r = 1.73$. (a) Normalized velocity profile, and (b) normalized streamwise Reynolds stress.

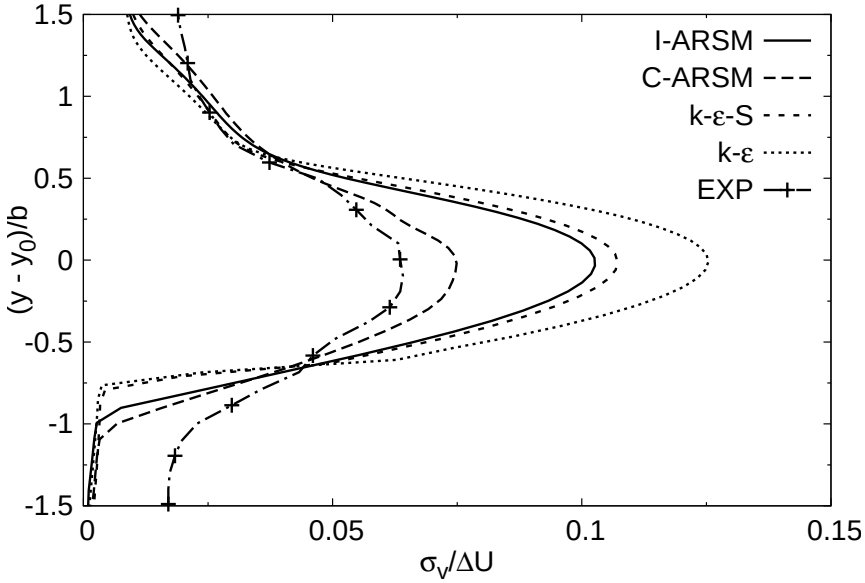

(a) Normalized cross-stream Reynolds stress.

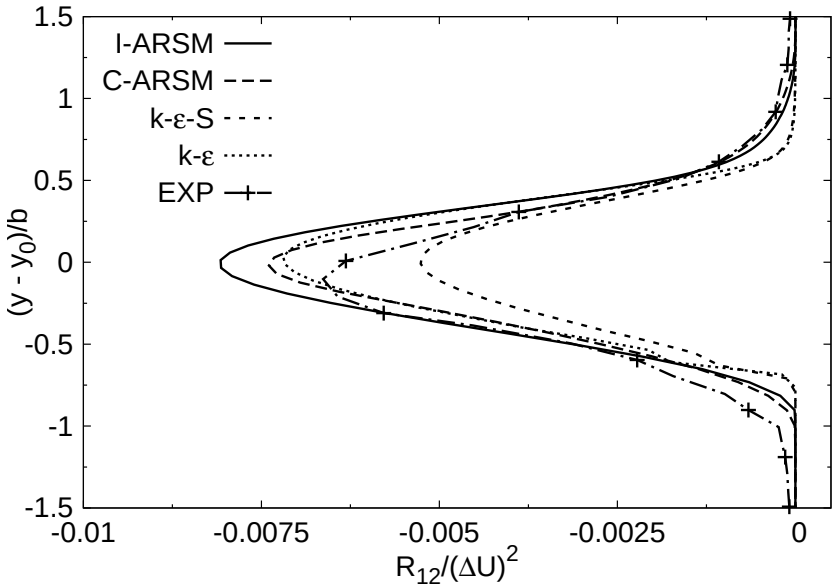

(b) Normalized shear Reynolds stress.

Figure 3.28: Plane mixing-layer results for C4, $M_r = 1.73$. (a) Normalized cross-stream Reynolds stress, and (b) normalized shear Reynolds stress.

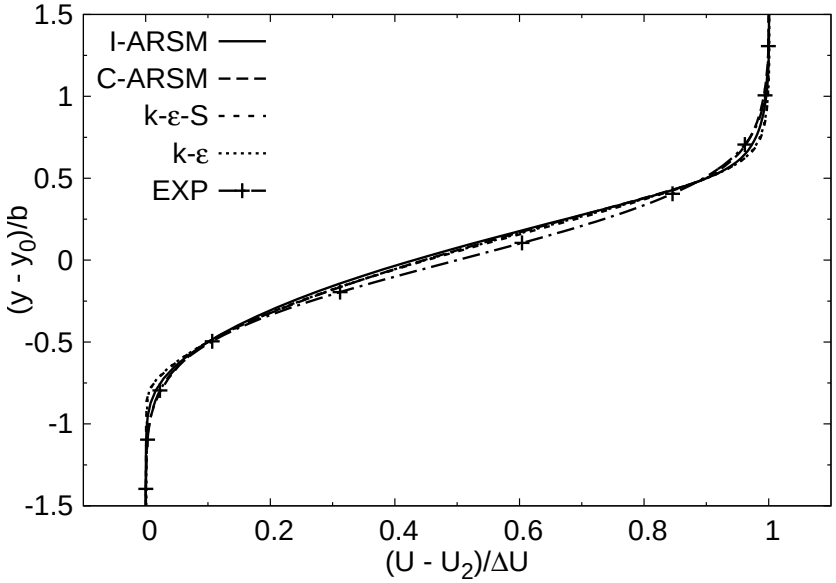

(a) Streamwise velocity similarity profile.

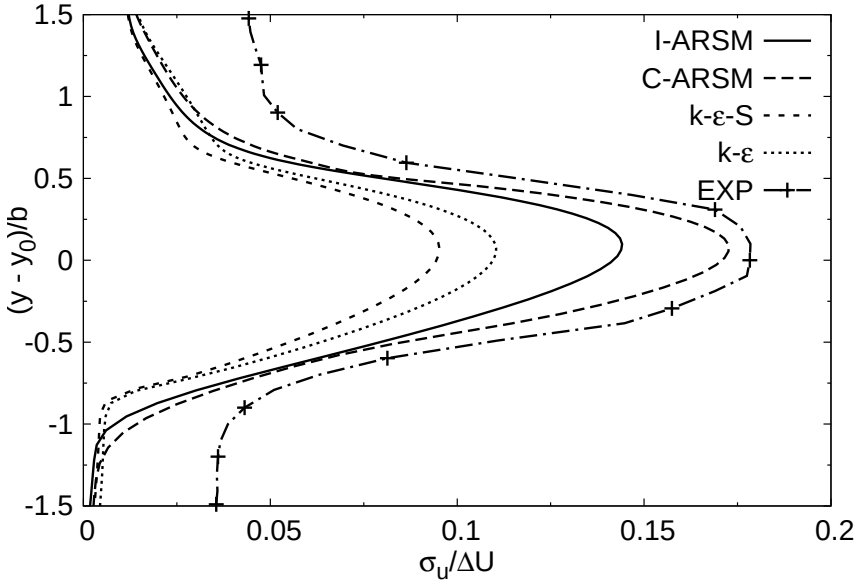

(b) Normalized streamwise Reynolds stress.

Figure 3.29: Plane mixing-layer results for C5, $M_r = 1.97$. (a) Normalized velocity profile, and (b) normalized streamwise Reynolds stress.

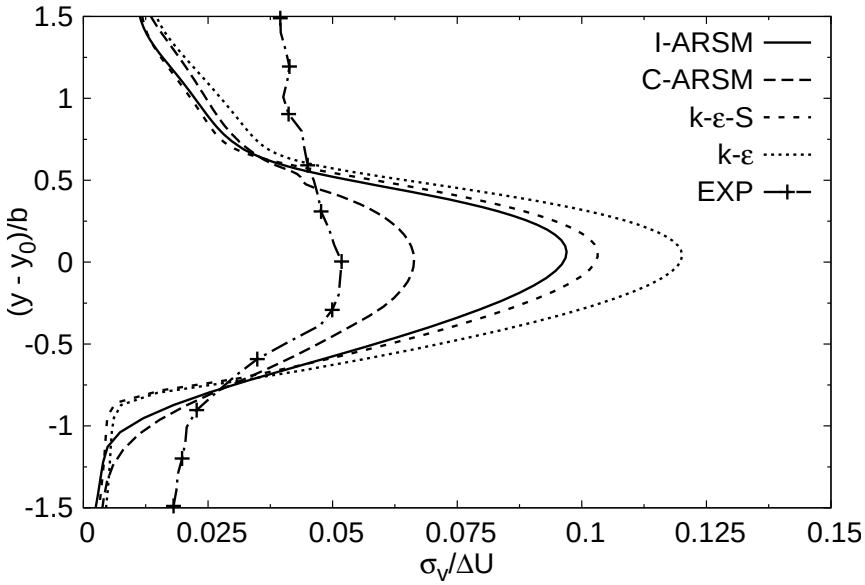

(a) Normalized cross-stream Reynolds stress.

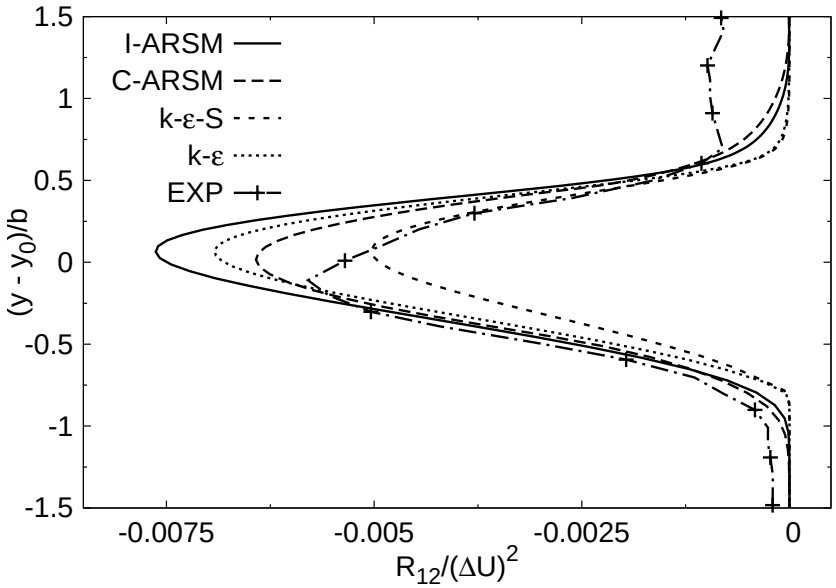

(b) Normalized shear Reynolds stress.

Figure 3.30: Plane mixing-layer results for C5, $M_r = 1.97$. (a) Normalized cross-stream Reynolds stress, and (b) normalized shear Reynolds stress.

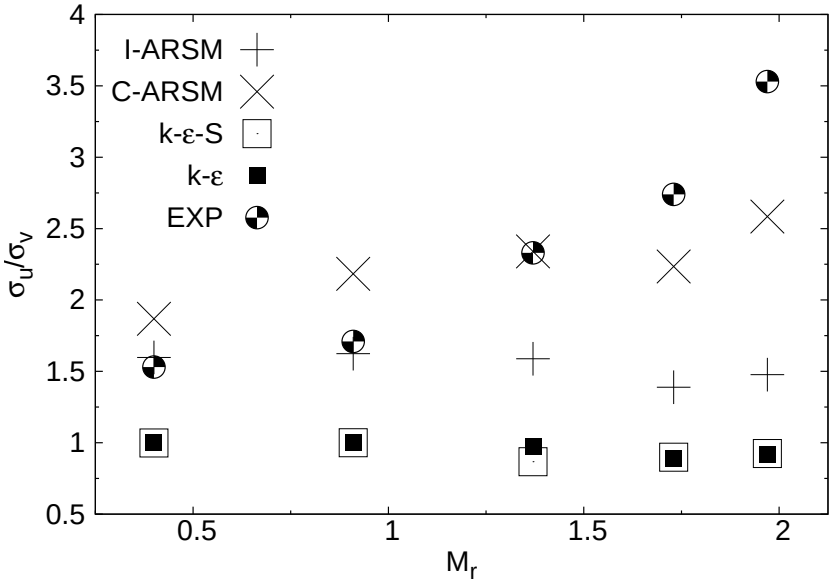

Figure 3.31: Computed mixing-layer anisotropy.

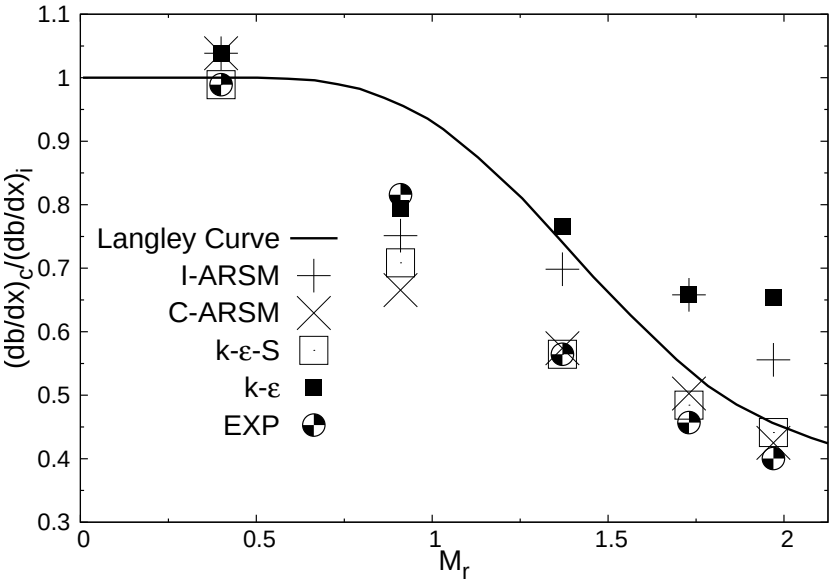

Figure 3.32: Computed normalized mixing-layer spreading rates.

3.7 Conclusions

In this work a fully explicit algebraic Reynolds stress model is developed that is capable of capturing compressibility effects based on the role of pressure at different gradient Mach number regimes. By following an analysis similar to that of Durbin [15], it is demonstrated that the present algebraic Reynolds stress model is fully realizable. Realizability is of paramount importance in eliminating the unphysical behavior that can be exhibited by turbulence closure models models near stagnation points in bluff body and impinging jet flows [4,86].

The new C – ARSM is employed to compute the evolution of homogeneous shear flow and high-speed plane mixing-layers. Comparisons are made with the compressible homogeneous shear DNS of Sarkar [71] and the experimental data of Goebel & Dutton [33], as well as three standard turbulence models. The main findings are:

1. The present C – ARSM captures the asymptotic behavior of compressible homogeneous shear DNS.

2. The present C – ARSM yields reduced mixing-layer spreading rates at high relative Mach number, consistent with the experimental data of Goebel & Dutton [33]. Incompressible models do not capture the mixing inhibition.

3. The Reynolds shear stress obtained from the present C – ARSM is in adequate agreement with data. The incompressible models overpredict the magnitude of shear stress at high relative Mach number.

4. The streamwise velocity similarity profiles from all models are near identical and agree well with data.

4. SECOND-MOMENT COMPUTATIONS OF SUPERSONIC BOUNDARY LAYERS

4.1 Introduction

High-speed boundary layers pose additional modeling challenges pertaining to near-wall phenomena not encountered in mixing-layers and other free shear flows. For example, the thermal boundary condition at the wall – adiabatic vs. constant temperature, cold vs. heated – can have a major influence on the velocity field. The closure model for turbulent heat flux (or equivalently turbulent Prandtl number) plays a critical role [7]. Furthermore, low-Reynolds number and wall-reflection physics which are important in subsonic boundary layers may also play a vital role. All these closures introduce further model coefficients. Accurate calibration of those terms goes outside the scope of this work. Here established low-speed models are used for those effects. Thus the purpose of the present computations is not to achieve perfect comparison with data, but to demonstrate that the novel pressure closures developed in chapter 2 lead to reasonable results.

4.2 Numerical implementation

Model computations are performed of a hypersonic boundary layer with freestream Mach number of 7.2, and compared with the experimental data of Owen & Horstman [56]. Computations are also performed of a supersonic boundary layer with freestream Mach number of 3.0, comparisons for this case are made with the DNS data of Duan et al. [14] Comparisons are shown between proposed near-wall corrections to the GG-I pressure strain correlation model and the standard SSG-S model. All models are tested using a standard turbulent heat flux model, constant turbulent Prandtl number and no wall-reflection terms. For these computations the well-established EDGE

Set	γ^*	β	σ_ω	σ_d
1	0.518	0.0747	0.53 (1.0)	1.0
2	0.44	0.0828	1.0	0.4

Table 4.1: Model coefficients used in the Hellsten [36] ω equation. Modified values are noted between parenthesis.

code (`http://www.foi.se/edge/`) is used, which has been extensively validated in both internal and external flows [18, 19]. For better near-wall characteristics, the ω rather than the ε equation is used. The ω equation developed by Hellsten [36] is employed

$$\frac{\partial}{\partial t}(\overline{\rho}\omega)+\frac{\partial}{\partial x_i}(\overline{\rho}\omega\tilde{u}_i) = \frac{\partial}{\partial x_j}\left[(\mu+\mu_t\sigma_\omega)\,\frac{\partial\omega}{\partial x_j}\right]+\overline{\rho}\gamma^*\frac{\omega}{k}P-\overline{\rho}\beta\omega^2+\frac{\overline{\rho}\sigma_d}{\omega}\max\left(\frac{\partial k}{\partial x_j}\frac{\partial\omega}{\partial x_j};0\right). \tag{4.1}$$

Dissipation is found by using

$$\varepsilon = \beta^* k\omega, \quad \beta^* = 0.09. \tag{4.2}$$

The constants γ^*, β, σ_ω, and σ_d vary according to

$$x = f_{mix}x_1 + (1-f_{mix})\,x_2, \tag{4.3}$$

where the mixing function f_{mix} is similar to that of Menter [54], for details please see Hellsten [36]. The model coefficients are provided in table 4.1.

4.3 Boundary conditions

The boundary conditions are shown schematically in figure 4.1. Table 4.2 shows the values for each boundary condition as well as the Reynolds number per unit

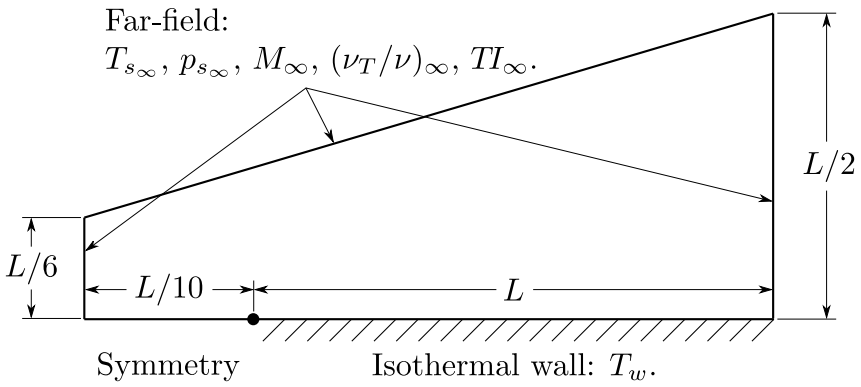

Figure 4.1: Two dimensional supersonic boundary layer boundary conditions.

Case	T_{s_∞} [K]	p_{s_∞} [kPa]	M_∞	$(\nu_T/\nu)_\infty$	TI_∞ [%]	T_w [K]	L [m]	Re_x [1/m]
M3	219.9	5.743	3.0	0.1	0.1	552	3.0	5.58×10^6
M7	58.67	0.681	7.2	0.1	0.1	310	3.0	11.6×10^6

Table 4.2: Supersonic boundary layer boundary conditions.

length defined as

$$Re_x = \frac{\overline{\rho}_\infty U_\infty}{\mu_\infty}. \tag{4.4}$$

For the M7 case, the boundary conditions match the experiments of Owen & Horstman [56], whereas for the M3 case they match the DNS data of Duan et al. [14].

4.4 Grid independence study

Three grids are used to ensure grid independence. The coarse grid consists of 14,700 cells (105 by 140), the medium grid 30,000 cells (150 by 200), and the fine grid 58,800 cells (210 by 280). The results are given in figures 4.2 and 4.3. The mean square error is plotted in figure 4.4 and is computed by using

$$MSE = \frac{1}{n}\sum_{i=1}^{n}\left(\tilde{u}_{1_i} - \tilde{u}^*_{1_i}\right)^2, \tag{4.5}$$

where $\tilde{u}_1^*$ is the streamwise velocity of the finest grid. The agreement between medium and fine grids is adequate indicating grid independence.

4.5 Objective of study

As mentioned in the introduction, the objective of this study is to show that with simple near-wall modifications, the pressure-related closures can achieve acceptable agreement with experimental data. A comprehensive recalibration of the various ω equation coefficients, which may depend on Mach number, is beyond the scope of this work. Towards the present objective, the following near-wall modifications are used in the compressible pressure-strain correlation model developed in chapter 2.

1. The ω equation coefficients can have a dramatic effect on the near-wall behavior. The σ_ω closure coefficient controls the turbulent transport of specific dissipation rate. In standard models, this coefficient is typically varied between 0.5 and 1.0 [36, 54, 93]. To test the effect of modifying this term, computations are performed with both the blending function given by Hellsten [36], as well as a constant value of $\sigma_\omega = 1.0$. The values used in the Hellsten ω equation are provided in table 4.1.

2. The lengthscale in the gradient Mach number definition may need to be adjusted for flow regions inside a boundary layer. Standard arguments for near-wall behavior [74] lead to the lengthscale scaling as $\ell \sim d$, where d is the wall distance. In this study, the following three lengthscales are tested

$$\ell = \frac{k^{3/2}}{\varepsilon} = \frac{k^{1/2}}{\beta^* \omega}, \tag{4.6a}$$

$$\ell = d, \tag{4.6b}$$

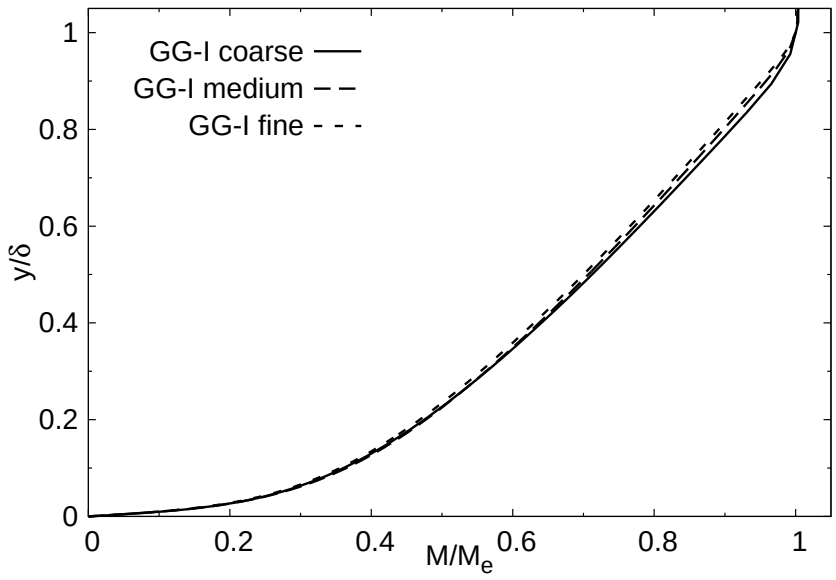

(a) Normalized Mach number.

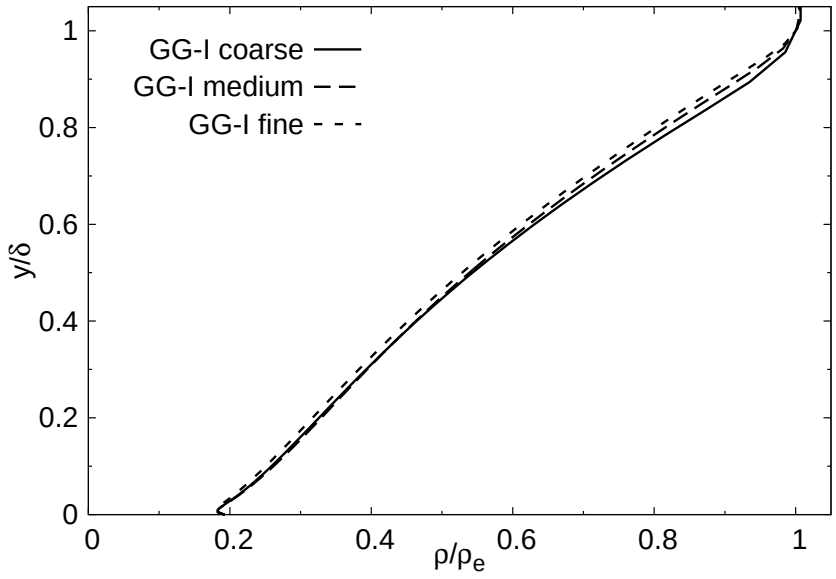

(b) Normalized density.

Figure 4.2: Flat plate boundary layer grid study, $M_\infty = 7.2$. (a) Normalized Mach number, and (b) normalized density.

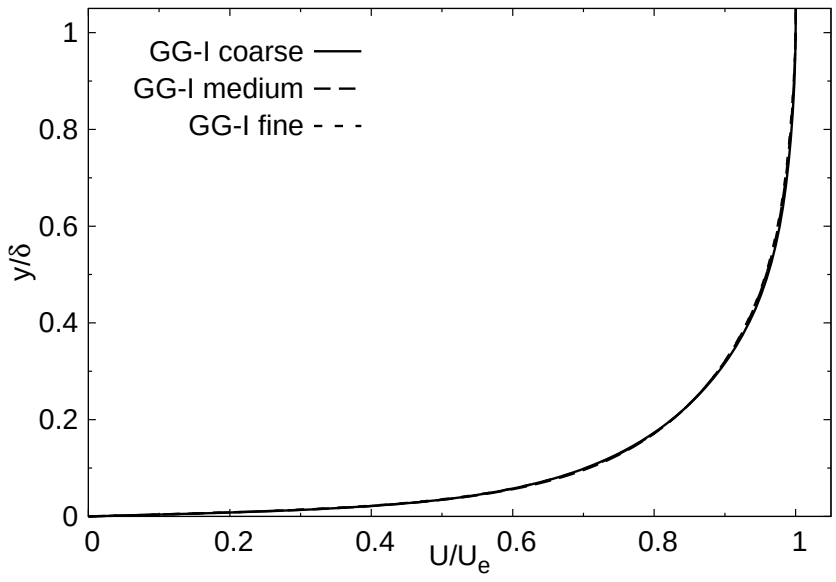

Figure 4.3: Flat plate boundary layer grid study, $M_\infty = 7.2$, normalized streamwise velocity.

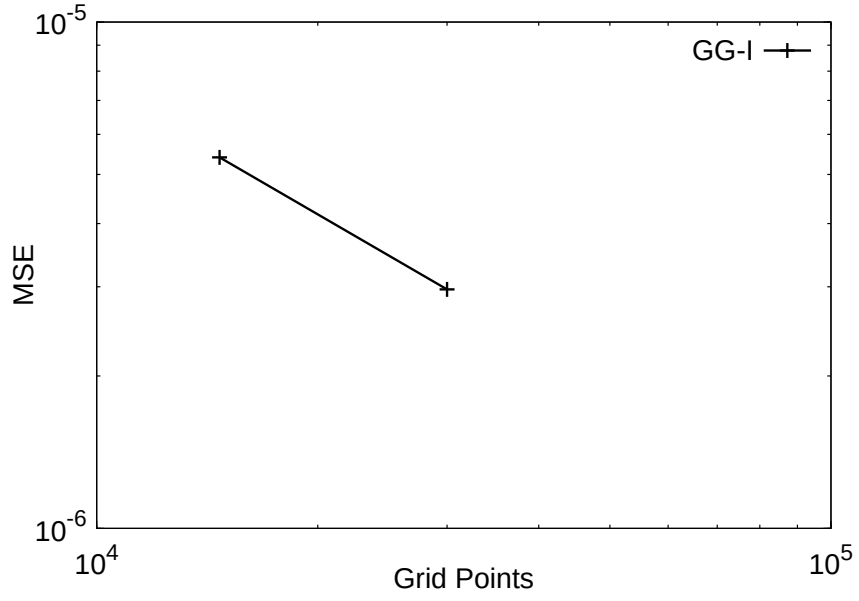

Figure 4.4: Mean square error of $\tilde{u}_1$ velocity.

$$\ell = \min\left(d, \frac{k^{1/2}}{\beta^* \omega}\right). \tag{4.6c}$$

4.6 Results

4.6.1 Modification of σ_ω

The first results presented highlight the effect of modifying the σ_ω coefficient. Figures 4.5 – 4.6 compare model computations with the experimental data of Owen & Horstman [56]. In these figures δ is the boundary layer thickness, and the subscript $(\cdot)_e$ refers to a value at the edge of the boundary layer. As is customary for compressible boundary layers, the van Driest transformation is used to compute u^+, for details see White [92]

$$u^+ = \frac{1}{\overline{u}_\tau}\int_0^{\tilde{u}} \left(\frac{\overline{\rho}}{\rho_w}\right)^{1/2} d\tilde{u}, \quad \overline{u}_\tau = \left(\frac{\tau_w}{\rho_w}\right)^{1/2}, \quad \tau_w = \mu_w \left.\frac{\partial \tilde{u}}{\partial y}\right|_{y=0}, \quad y^+ = \frac{y\overline{u}_\tau}{\nu_w}. \tag{4.7}$$

The friction velocity is given by $\overline{u}_\tau$, and quantities evaluated at the wall are denoted by $(\cdot)_w$. Data is compared at the streamwise location $x = 2.37$ m. Figures 4.5(a) – 4.6(a) show a significant improvement in mean quantities by modifying the σ_ω coefficient. On the other hand, figure 4.6(b) shows mixed results. In van Driest coordinates, the modification of σ_ω has a negligible effect on the GG-I model, but provides a substantial improvement in the SSG-S model. Nonetheless, it is quite clear that overall better results are obtained by modifying the σ_ω coefficient to a constant value of unity for both models. In the following, only models using a constant σ_ω coefficient are considered.

4.6.2 Near-wall lengthscale modification

Figures 4.7 – 4.8 compare GG-I model computations using the three proposed lengthscale definitions with the data of Owen & Horstman [56]. The GG-I INT, GG-I

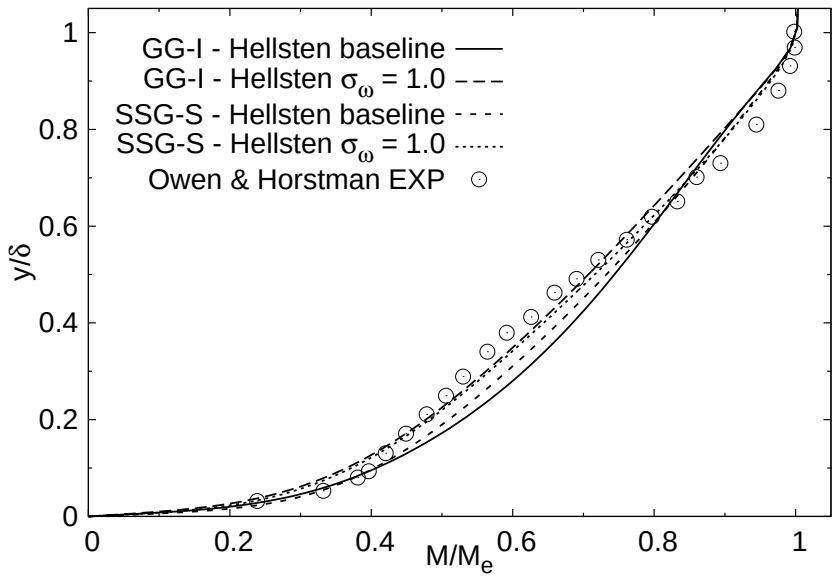

(a) Normalized Mach number.

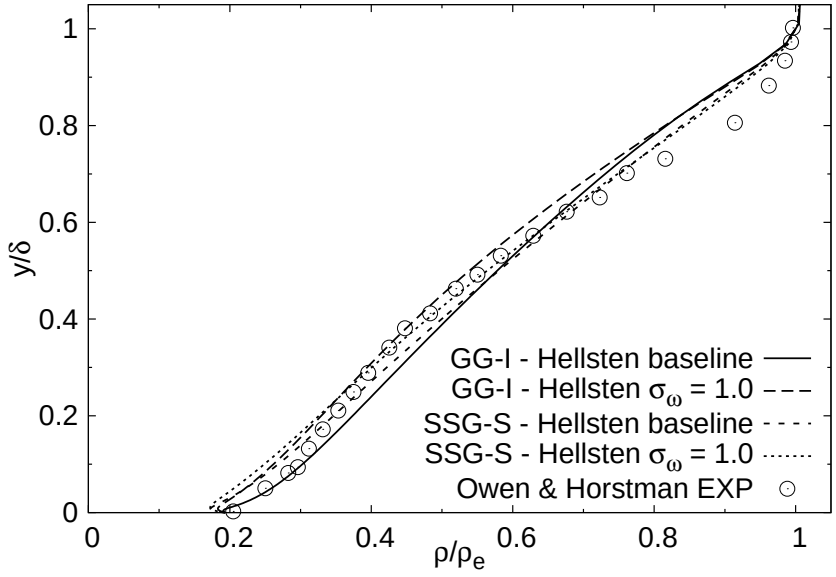

(b) Normalized density.

Figure 4.5: Flat plate boundary layer, $M_\infty = 7.2$, effect of modifying σ_ω. (a) Normalized Mach number, and (b) normalized density.

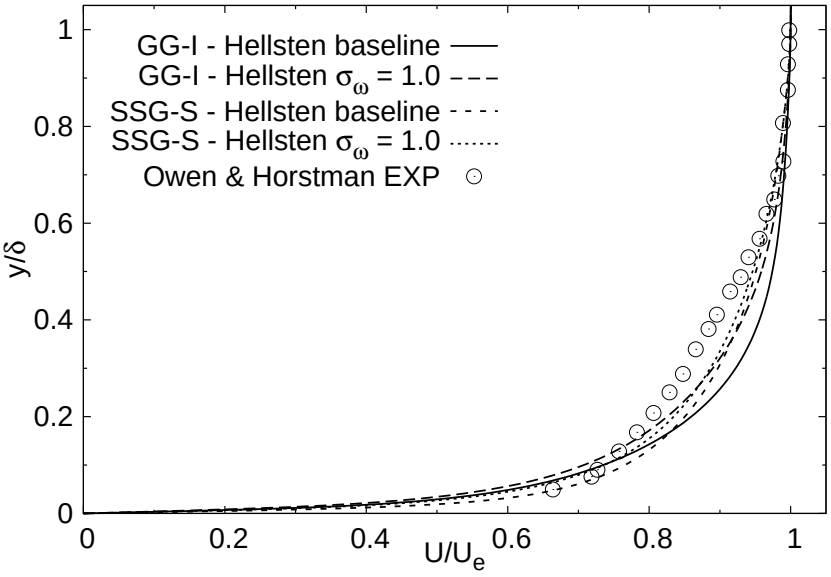

(a) Normalized streamwise velocity.

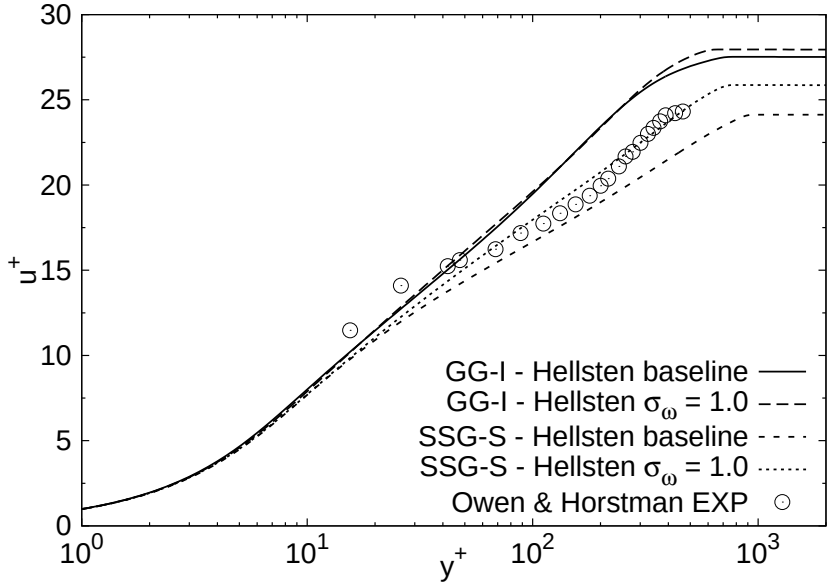

(b) Streamwise velocity in van Driest coordinates.

Figure 4.6: Flat plate boundary layer, $M_\infty = 7.2$, effect of modifying σ_ω. (a) Normalized streamwise velocity, and (b) streamwise velocity in van Driest coordinates.

WALL, and GG-I MIN models use the lengthscales defined in equations (4.6a), (4.6b), and (4.6c) respectively. From these figures it is evident that a modification to the lengthscale is required for the GG-I model to achieve satisfactory log-law behavior. It can be seen that the GG-I MIN model achieves marginally better performance in van Driest coordinates. Therefore equation (4.6c) is chosen to be an adequate lengthscale for near-wall flow regions.

4.6.3 Mach 3 comparison with DNS

The GG-I MIN and SSG-S model computations are compared with the direct numerical simulation data of Duan et al. [14]. Boundary layers with freestream Mach number less than 5 typically exhibit negligible compressibility effects [80]. Thus, for these computations it is expected that both models perform satisfactorily. Figure 4.9(a) compares normalized mean temperature profiles. The DNS data for mean temperature is taken to be the Crocco relation [91], which Duan et al. [14] found to be in excellent agreement with their simulations up to a freestream Mach number of 12.0. It can be seen that both models closely follow the DNS data of normalized mean temperature profile. Figure 4.9(b) shows the normalized streamwise velocity profiles in van Driest coordinates. It is clear that both models are capable of reproducing the behavior of the DNS data fairly well, especially in the log-law region.

4.7 Conclusions

In this work it is shown that by using simple near-wall corrections, the compressible pressure-strain correlation model developed in chapter 2 agrees well with both experimental [56] and direct numerical simulation [14] data of supersonic boundary layers. Two simple near-wall corrections are proposed: the first is to modify one of the parameters in the ω equation, and the second is to redefine the lengthscale in the gradient Mach number definition to be more consistent with traditional boundary

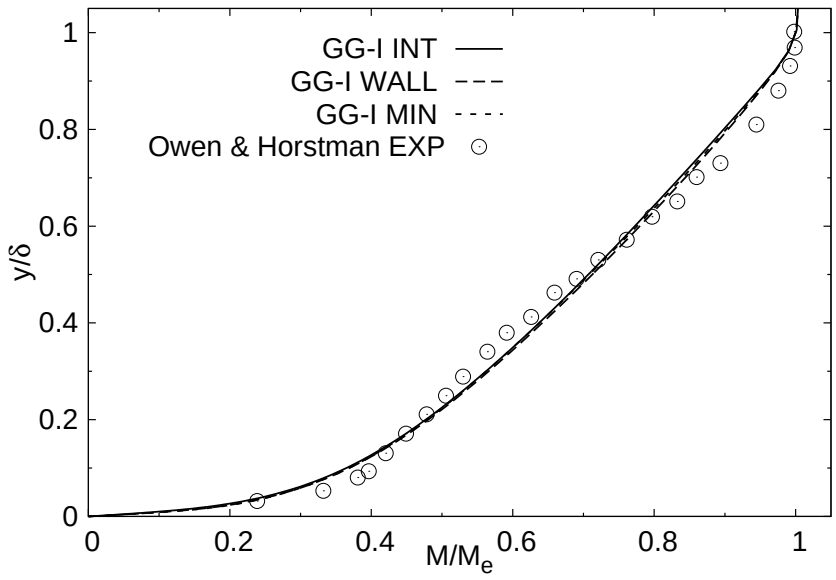

(a) Normalized Mach number.

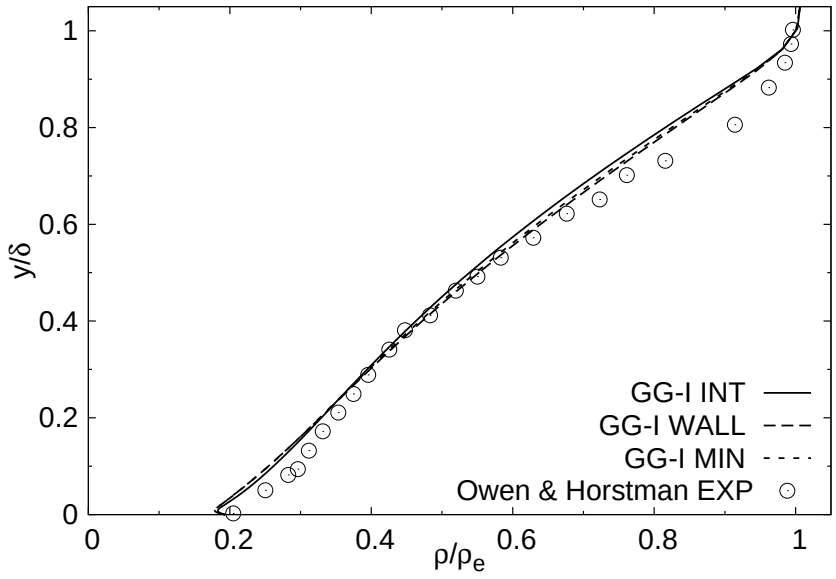

(b) Normalized density.

Figure 4.7: Flat plate boundary layer, $M_\infty = 7.2$, effect of modifying ℓ. (a) Normalized Mach number, and (b) normalized density.

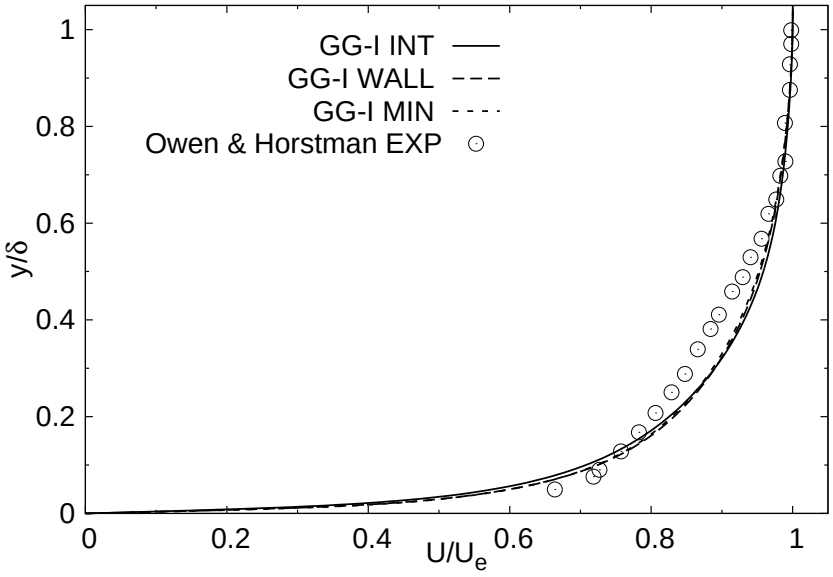

(a) Normalized streamwise velocity.

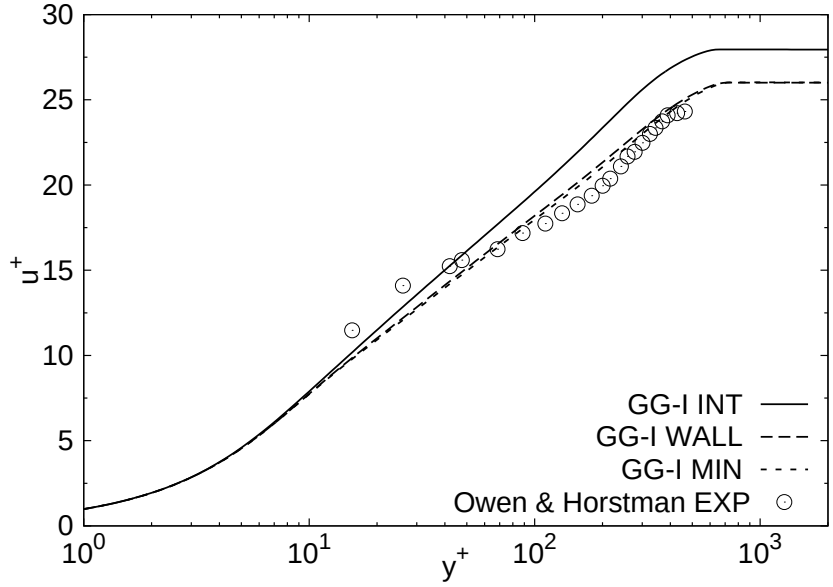

(b) Streamwise velocity in van Driest coordinates.

Figure 4.8: Flat plate boundary layer, $M_\infty = 7.2$, effect of modifying ℓ. (a) Normalized streamwise velocity, and (b) streamwise velocity in van Driest coordinates.

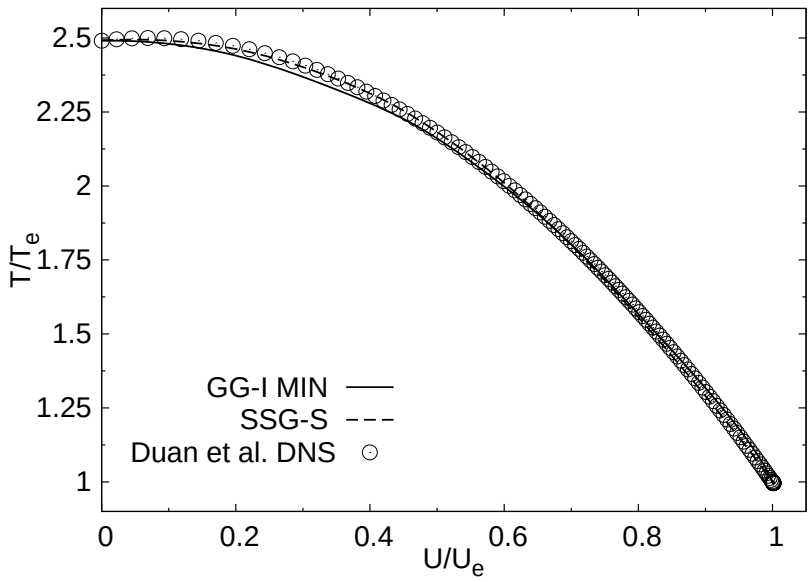

(a) Normalized mean temperature.

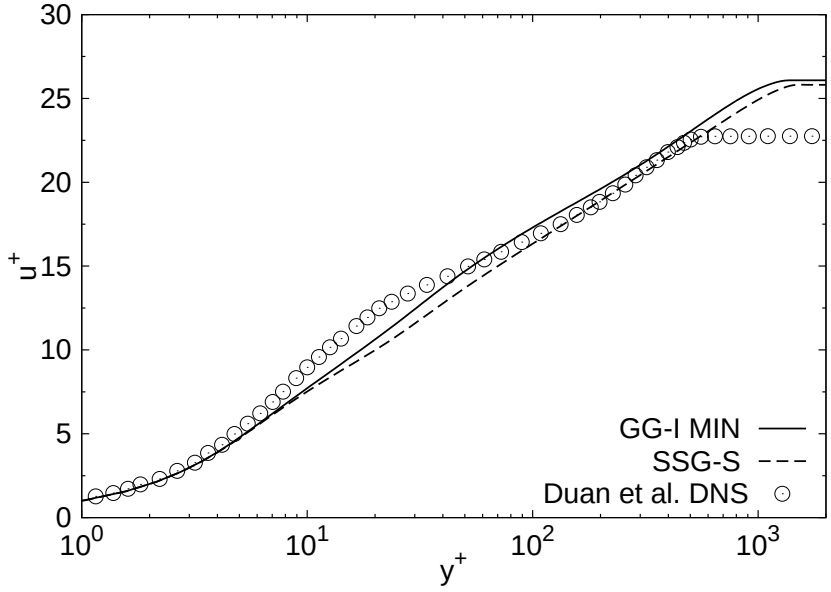

(b) Streamwise velocity in van Driest coordinates.

Figure 4.9: Flat plate boundary layer, $M_\infty = 3.0$. (a) Normalized mean temperature, and (b) streamwise velocity in van Driest coordinates.

layer theory. The present results show that with these two simple modifications, the proposed pressure-strain correlation model can achieve adequate agreement with super and hypersonic boundary layers.

5. CONCLUSIONS

5.1 Conclusions for study #1

The first work of this thesis develops a new compressible pressure-strain correlation model for shear flows that builds on well established incompressible forms [43]. A reduction of the pressure-strain correlation at high gradient Mach number is proposed based on observations from direct numerical simulations [20, 57, 71] and rapid distortion theory [6, 8]. The pressure-strain correlation model coefficients are functions of gradient Mach number and are calibrated by analyzing the fixed points of homogeneous shear in conjunction with the long time behavior of compressible homogeneous shear DNS data [71]. To be consistent with the effect pressure-dilatation has on turbulent kinetic and internal energies, a minor modification to the standard dissipation rate equation is proposed, and found to cause no adverse effects in the performance of the present compressible pressure-strain correlation model. The model agreement with compressible homogeneous shear DNS for long shear time is excellent. Without any modification to the model coefficients, second-moment modeling calculations of supersonic mixing-layers are performed and compared against the experimental data of Goebel & Dutton [33]. As the relative Mach number of the mixing-layer increases, it is found that the present model:

1. Captures an increase in Reynolds stress anisotropy.

2. Predicts a decrease in Reynolds shear stress, and consequently a decrease in production.

3. Predicts a decrease in mixing-layer spreading rates, thus capturing the Langley curve trend [42].

These three features of the present model enable excellent agreement with experimental data of supersonic mixing-layers. Model implementation into existing RSM solvers is straightforward and causes a negligible increase in CPU time compared to standard incompressible models.

5.2 Conclusions for study #2

In the second study of this thesis the compressible pressure-strain correlation model developed in chapter 2 is incorporated into the algebraic modeling framework to obtain a fully explicit algebraic Reynolds stress model. The resulting model is shown to be able to replicate high-speed mixing-layer experimental behavior [33], as well as the long time behavior of compressible homogeneous DNS [71]. As the model is parameterized by gradient Mach number, in the incompressible limit the behavior reverts to that of the Girimaji [25] ARSM. Thus the model can be successfully applied to both compressible and incompressible flows.

The present model has the following four salient features:

1. C−ARSM is fully realizable, whereas the standard $k-\varepsilon$ model violates realizability for large dimensionless strain rates.

2. C−ARSM is able to capture the reduction of normalized mixing-layer spreading rates at high relative Mach number, thus replicating the Langley curve trend [42]. The $k-\varepsilon$ model requires the now known to be unphysical Sarkar compressibility correction to achieve comparable performance [71, 72].

3. C−ARSM closely captures the reduction of Reynolds shear stress at high relative Mach number, a requirement for high-speed mixing applications.

4. C−ARSM captures the overall trend of increasing Reynolds stress anisotropy at high relative Mach number. None of the other models tested is able to

replicate this behavior.

The computational effort of the C – ARSM is approximately 15% more than standard two-equation models. This is a very reasonable price to pay for the additional physics that the present model can capture, especially when compared against the cost of a full differential Reynolds stress modeling approach, which is typically twice as expensive as standard two-equation models.

5.3 Conclusions for study #3

The final study of this thesis validates the new pressure-strain correlation model in the context of supersonic boundary layers. It is shown that with two simple near-wall modifications the present model is able to adequately replicate high-speed boundary layer behavior of both experimental [56] and direct numerical simulation [14] data. The agreement with mean velocity, density, temperature, and Mach profiles is quite acceptable, even without the use of wall-reflection terms or sophisticated thermal-flux models.

REFERENCES

[1] V. Adumitroaie, J. R. Ristorcelli, and D. B. Taulbee. Progress in Favré–Reynolds stress closures for compressible flows. *Physics of Fluids*, 11(9):2696–2719, September 1999.

[2] ANSYS®, Inc., Southpointe 275 Technology Drive Canonsburg, PA 15317. *ANSYS® FLUENT Theory Guide*, November 2010. Release 13.0.

[3] B. Aupoix. Modelling of compressibility effects in mixing layers. *Journal of Turbulence*, 5:1–17, 2004.

[4] M. Behnia, S. Parneix, and P. A. Durbin. Prediction of heat transfer in an axisymmetric turbulent jet impinging on a flat plate. *International Journal of Heat and Mass Transfer*, 41(12):1845–1855, 1998.

[5] R. Bertsch. Rapidly sheared compressible turbulence: Characterization of different pressure regimes and effect of thermodynamic fluctuations. Master's thesis, Texas A&M University, College Station, 2010.

[6] R. L. Bertsch, S. Suman, and S. S. Girimaji. Rapid distortion analysis of high Mach number homogeneous shear flows: characterization of flow-thermodynamics interaction regimes. Submitted to Physics of Fluids, 2012.

[7] R. D. W. Bowersox. Extension of equilibrium turbulent heat flux models to high-speed shear flows. *Journal of Fluid Mechanics*, 633:61–70, 2009.

[8] C. Cambon, G. N. Coleman, and N. N. Mansour. Rapid distortion analysis and direct simulation of compressible homogeneous turbulence at finite Mach number. *Journal of Fluid Mechanics*, 257:641–665, 1993.

[9] B. Chaouat and R. Schiestel. A new partially integrated transport model for subgrid-scale stresses and dissipation rate for turbulent developing flows. *Physics of Fluids*, 17(6):065106, 2005.

[10] N. Chinzei, G. Masuya, T. Komuro, A. Murakami, and K. Kudou. Spreading of two-stream supersonic turbulent mixing layers. *Physics of Fluids*, 29(5):1345–1347, 1986.

[11] N. T. Clemens and M. G. Mungal. Large-scale structure and entrainment in the supersonic mixing layer. *Journal of Fluid Mechanics*, 284:171–216, 1995.

[12] D. C. Cottrell III and M. W. Plesniak. Sensitivity of mixed subsonic-supersonic turbulent mixing layers. *Journal of Propulsion and Power*, 17(4):823–835, 2001.

[13] S. C. Crow. Viscoelastic properties of fine-grained incompressible turbulence. *Journal of Fluid Mechanics*, 33:1–20, 1968.

[14] L. Duan, I. Beekman, and M. P. Martín. Direct numerical simulation of hypersonic turbulent boundary layers. Part 3. Effect of Mach number. *Journal of Fluid Mechanics*, 672:245–267, 2011.

[15] P. A. Durbin. On the $k - \varepsilon$ stagnation point anomaly. *International Journal of Heat and Fluid Flow*, 17:89–90, 1996.

[16] P. A. Durbin and C. G. Speziale. Realizability of second-moment closure via stochastic analysis. *Journal of Fluid Mechanics*, 280:395–407, 1994.

[17] P. A. Durbin and O. Zeman. Rapid distortion theory for homogeneous compressed turbulence with application to modelling. *Journal of Fluid Mechanics*, 242:349–370, 1992.

[18] P. Eliasson. EDGE, a Navier-Stokes solver for unstructured grids. Technical Report FOI-R-0298-SE, FOI, Sweden, 2005.

[19] P. Eliasson and S.-H. Peng. Drag prediction for the DLR-F6 wing-body configuration using the EDGE solver. *Journal of Aircraft*, 45(3):837–847, 2008.

[20] J. B. Freund, S. K. Lele, and P. Moin. Compressibility effects in a turbulent annular mixing layer. Part 1. Turbulence and growth rate. *Journal of Fluid Mechanics*, 421:229–267, 2000.

[21] H. Fujiwara, Y. Matsuo, and Arakawa C. A turbulence model for the pressure-strain correlation term accounting for compressibility effects. *International Journal of Heat and Fluid Flow*, 21(3):354–358, 2000.

[22] T. B. Gatski and T. Jongen. Nonlinear eddy viscosity and algebraic stress models for solving complex turbulent flows. *Progress in Aerospace Sciences*, 36:655–682, 2000.

[23] T. B. Gatski and C. G. Speziale. On explicit algebraic stress models for complex turbulent flows. *Journal of Fluid Mechanics*, 254:59–78, 1993.

[24] M. Germano. Turbulence: the filtering approach. *Journal of Fluid Mechanics*, 238:325–336, 1992.

[25] S. S. Girimaji. Fully explicit and self-consistent algebraic Reynolds stress model. *Theoretical and Computational Fluid Dynamics*, 8:387–402, 1996.

[26] S. S. Girimaji. A Galilean invariant explicit algebraic Reynolds stress model for turbulent curved flows. *Physics of Fluids*, 9(4):1067–1077, 1997.

[27] S. S. Girimaji. Pressure-strain correlation modelling of complex turbulent flows. *Journal of Fluid Mechanics*, 422:91–123, 2000.

[28] S. S. Girimaji. Lower-dimensional manifold (algebraic) representation of Reynolds stress closure equations. *Theoretical and Computational Fluid Dynamics*, 14(4):259–281, 2001.

[29] S. S. Girimaji. A new perspective on realizability of turbulence models. *Journal of Fluid Mechanics*, 512:191–210, 2004.

[30] S. S. Girimaji. Partially-averaged Navier-Stokes model for turbulence: A Reynolds-averaged Navier-Stokes to direct numerical simulation bridging method. *Journal of Applied Mechanics*, 73(3):413–421, 2006.

[31] S. S. Girimaji and S. Balachandar. Analysis and modeling of buoyancy-generated turbulence using numerical data. *International Journal of Heat and Mass Transfer*, 41:915–929, 1998.

[32] S. S. Girimaji, E. Jeong, and R. Srinivasan. Partially-averaged Navier-Stokes method for turbulence: Fixed point analysis and comparison with unsteady partially averaged Navier-Stokes. *Journal of Applied Mechanics*, 73(3):422–429, 2006.

[33] S. G. Goebel and J. C. Dutton. Experimental study of compressible turbulent mixing layers. *AIAA Journal*, 29(4):538–546, 1991.

[34] C. A. Gomez and S. S. Girimaji. Toward second-moment closure modelling of compressible shear flows. Submitted to Journal of Fluid Mechanics, 2012.

[35] J. L. Hall, P. E. Dimotakis, and H. Rosemann. Experiments in nonreacting compressible shear layers. *AIAA Journal*, 31(12):2247–2254, 1993.

[36] A. Hellsten. New advanced k–ω turbulence model for high-lift aerodynamics. *AIAA Journal*, 43(9):1857–1869, September 2005.

[37] S. Huang and S. Fu. Modelling of pressure-strain correlation in compressible turbulent flow. *Acta Mechanica Sinica*, 24(1):37–43, 2008.

[38] A. V. Johansson and M. Hallbäck. Modelling of rapid pressure-strain in Reynolds-stress closures. *Journal of Fluid Mechanics*, 269:143–168, 1994.

[39] W. P. Jones and P. Musonge. Closure of the Reynolds stress and scalar flux equations. *Physics of Fluids*, 31(12):3589–3604, 1988.

[40] H. Khlifi, J. Abdallah, H. Aïcha, and L. Taïeb. A priori evaluation of the Pantano and Sarkar model in compressible homogeneous shear flows. *Comptes Rendus Mecanique*, 339:27–34, 2011.

[41] J. Kim and S. O. Park. New compressible turbulence model for free and wall-bounded shear layers. *Journal of Turbulence*, 11(10):1–20, 2010.

[42] S. J. Kline, B. J. Cantwell, and G. M. Lilley. Proc. 1980-81-AFOSR-HTTM-Stanford-Conf. on complex turbulent flows. Technical Report Vol. 1, Stanford University, California, 1982.

[43] B. E. Launder, G. J. Reece, and W. Rodi. Progress in the development of a Reynolds-stress turbulence closure. *Journal of Fluid Mechanics*, 68:537–566, 1975.

[44] T. A. Lavin. Reynolds and Favre-averaged rapid distortion theory for compressible, ideal-gas turbulence. Master's thesis, Texas A&M University, College Station, 2007.

[45] T. A. Lavin, S. S. Girimaji, S. Suman, and H. Yu. Flow-thermodynamics interactions in rapidly-sheared compressible turbulence. *Theoretical and Computational Fluid Dynamics*, 26(6):501–522, 2012. 10.1007/s00162-011-0243-9.

[46] K. Lee and S. S. Girimaji. Flow-thermodynamics interactions in decaying anisotropic compressible turbulence with imposed temperature fluctuations. *Theoretical and Computational Fluid Dynamics*, pages 1–17, 2011. 10.1007/s00162-011-0249-3.

[47] K. Lee, S. S. Girimaji, and J. Kerimo. Validity of Taylor's dissipation-viscosity independence postulate in variable-viscosity turbulent fluid mixtures. *Physical Review Letters*, 101(7):074501, August 2008.

[48] F. S. Lien and M. A. Leschziner. Assessment of turbulent-transport models including non-linear RNG eddy-viscosity formulation and second-moment closure for flow over a backward-facing step. *Computers & Fluids*, 23(8):983–1004, 1994.

[49] D. Livescu, F. A. Jaberi, and C. K. Madnia. The effects of heat release on the energy exchange in reacting turbulent shear flow. *Journal of Fluid Mechanics*, 450:35–66, 2002.

[50] D. Livescu and C. K. Madnia. Small scale structure of homogeneous turbulent shear flow. *Physics of Fluids*, 16(8):2864–2876, August 2004.

[51] D. Livescu and J. R. Ristorcelli. Buoyancy-driven variable-density turbulence. *Journal of Fluid Mechanics*, 591:43–71, 2007.

[52] D. Livescu and J. R. Ristorcelli. Variable-density mixing in bouyancy-driven turbulence. *Journal of Fluid Mechanics*, 605:145–180, 2008.

[53] H. Marzougui, H. Khlifi, and T. Lili. Extension of the Launder, Reece and Rodi model on compressible homogeneous shear flow. *The European Physical Journal B*, 45:147–154, 2005.

[54] F. R. Menter. Two-equation eddy-viscosity turbulence models for engineering applications. *AIAA Journal*, 32(8):1598–1605, 1994.

[55] A. A. Mishra and S. S. Girimaji. Pressure-strain correlation modeling: towards achieving consistency with rapid distortion theory. *Flow, Turbulence and Combustion*, 85:593–619, 2010.

[56] F. K. Owen and C. C. Horstman. On the structure of hypersonic turbulent boundary layers. *Journal of Fluid Mechanics*, 53:611–636, 1972.

[57] C. Pantano and S. Sarkar. A study of compressibility effects in the high-speed turbulent shear layer using direct simulation. *Journal of Fluid Mechanics*, 451:329–371, 2002.

[58] D. Papamoschou and A. Roshko. The compressible turbulent shear layer: an experimental study. *Journal of Fluid Mechanics*, 197:453–477, 1988.

[59] C. H. Park and S. O. Park. A compressible turbulence model for the pressure-strain correlation. *Journal of Turbulence*, 6(2):1–25, 2005.

[60] S. Pennisi and M. Trovato. On the irreducibility of Professor G.F. Smith's representations for isotropic functions. *International Journal of Engineering Science*, 25:1059–1065, 1987.

[61] S. B. Pope. A more general effective-viscosity hypothesis. *Journal of Fluid Mechanics*, 72(2):331–340, 1975.

[62] S. B. Pope. Lagrangian PDF methods for turbulent flows. *Annual Review of Fluid Mechanics*, 26:23–63, 1994.

[63] S. B. Pope. *Turbulent flows*. Cambridge University Press, UK, 1st edition, 2000.

[64] W. C. Reynolds. Computation of turbulent flows. *Annual Review of Fluid Mechanics*, 8:183–208, 1976.

[65] J. R. Ristorcelli. A representation for the turbulent mass flux contribution to Reynolds-stress and two-equation closure for compressible turbulence. ICASE Report 93-88, NASA Langley Research Center, Hampton, VA, 1993.

[66] J. R. Ristorcelli, J. L. Lumley, and R. Abid. A rapid-pressure covariance representation consistent with the Taylor-Proudman theorem materially frame indifferent in the two-dimensional limit. *Journal of Fluid Mechanics*, 292:111–152, 1995.

[67] W. Rodi. A new algebraic relation for calculating the Reynolds stresses. *ZAMM, Journal of Applied Mathematics and Mechanics*, 56:T219–T221, 1976.

[68] J. C. Rotta. Statistiche theorie nichthomogener turbulenz. *Z. Phys.*, 129:547–572, 1951.

[69] M. Samimy and G. S. Elliot. Effects of compressibility on the characteristics of free shear layers. *AIAA Journal*, 28(3):439–445, 1990.

[70] S. Sarkar. The pressure-dilatation correlation in compressible flows. *Physics of Fluids*, 4(12):2674–2682, 1992.

[71] S. Sarkar. The stabilizing effect of compressibility in turbulent shear flow. *Journal of Fluid Mechanics*, 282:163–186, 1995.

[72] S. Sarkar, G. Erlebacher, and M. Y. Hussaini. The analysis and modelling of dilatational terms in compressible turbulence. *Journal of Fluid Mechanics*, 227:473–493, 1991.

[73] S. Sarkar, G. Erlebacher, and M. Y. Hussaini. Direct simulation of compressible turbulence in a shear flow. *Theoretical and Computational Fluid Dynamics*, 2:291–305, 1991.

[74] H. Schlichting and K. Gersten. *Boundary layer theory.* Springer-Verlag Berlin Heidelberg, Germany, 8$^{\text{th}}$ edition, 2000.

[75] U. Schumann. Realizability of Reynolds-stress turbulence models. *Physics of Fluids*, 20(5):721–725, 1977.

[76] T. H. Shih and J. L. Lumley. Remarks on turbulent constitutive relations. *Mathematical and Computer Modelling*, 18(2):9–16, 1993.

[77] A. Simone, G. N. Coleman, and C. Cambon. The effect of compressibility on turbulent shear flow: a rapid-distortion-theory and direct-numerical-simulation study. *Journal of Fluid Mechanics*, 330:307–338, 1997.

[78] T. Sjögren and A. V. Johansson. Development and calibration of algebraic nonlinear models for terms in the Reynolds stress transport equations. *Physics of Fluids*, 12(6):1554–1572, June 2000.

[79] G. F. Smith. On isotropic funcions of symmetric tensors, skew-symmetric tensors and vectors. *International Journal of Engineering Science*, 9:899–916, 1971.

[80] A. J. Smits and J.-P. Dussauge. *Turbulent shear layers in supersonic flow.* Springer Science+Business Media, Inc., USA, 2$^{\text{nd}}$ edition, 2006.

[81] C. G. Speziale. Analytical methods for the development of Reynolds-stress closures in turbulence. *Annual Review of Fluid Mechanics*, 23:107–157, 1991.

[82] C. G. Speziale, T. B. Gatski, and S. Sarkar. On testing models for the pressure-strain correlation of turbulence using direct simulations. *Physics of Fluids*, 4(12):2887–2899, 1992.

[83] C. G. Speziale, S. Sarkar, and T. B. Gatski. Modelling the pressure-strain correlation of turbulence: an invariant dynamical systems approach. *Journal of Fluid Mechanics*, 227:245–272, 1991.

[84] S. Suman and S. S. Girimaji. On the invariance of compressible Navier-Stokes and energy equations subject to density-weighted filtering. *Flow, Turbulence and Combustion*, 85(3):383–396, 2010.

[85] W. Sutherland. The viscosity of gases and molecular force. *Philosophical Magazine, Series 5*, 36(223):507–531, December 1893.

[86] A. Sveningsson and L. Davidson. Assessment of realizability constraints in $\overline{v^2} - f$ turbulence models. *International Journal of Heat and Fluid Flow*, 25:785–794, 2004.

[87] S. Tavoularis and S. Corrsin. Experiments in nearly homogeneous shear flow with a uniform mean temperature gradient. Part 1. *Journal of Fluid Mechanics*, 104:311–347, 1981.

[88] W. D. Thacker, S. Sarkar, and T. B. Gatski. Analyzing the influence of compressibility on the rapid pressure-strain rate correlation in turbulent shear flows. *Theoretical and Computational Fluid Dynamics*, 21(3):171–199, 2007.

[89] S. Wallin and A. V. Johansson. An explicit algebraic Reynolds stress model for incompressible and compressible turbulent flows. *Journal of Fluid Mechanics*, 403:89–132, 2000.

[90] S. Wallin and A. V. Johansson. Modelling streamline curvature effects in explicit algebraic Reynolds stress turbulence models. *International Journal of Heat and Fluid Flow*, 23(5):721–730, 2002.

[91] A. Walz. *Boundary layers of flow and temperature*. MIT Press, USA, 1st edition, 1969.

[92] F. M. White. *Viscous fluid flow*. McGraw-Hill Inc., USA, 2nd edition, 1991.

[93] D. C. Wilcox. Reassesment of the scale-determining equation for advanced turbulence models. *AIAA Journal*, 26(11):1299–1310, November 1988.

[94] D. C. Wilcox. *Turbulence modeling for CFD*. DCW Industries, Inc., USA, 1st edition, 1993.

APPENDIX A

CALIBRATED PRESSURE-STRAIN CORRELATION COEFFICIENTS

Three types of functions are used to find the least squares curve fits of the calibrated pressure-strain correlation model coefficients shown in figure 2.6

$$f_1 = a_1 \exp\left(a_2 M_g^*\right) + a_3 \exp\left(a_4 M_g^*\right), \tag{A.1}$$

$$f_2 = a_1 \exp\left[-\left(\frac{M_g^* - a_2}{a_3}\right)^2\right], \tag{A.2}$$

and

$$f_3 = \frac{a_1 M_g^* + a_2}{M_g^{*2} + a_3 M_g^* + a_4}, \tag{A.3}$$

where

$$M_g^* = \frac{M_g}{M_{g_{max}}}, \quad M_{g_{max}} = 3.05. \tag{A.4}$$

The fit coefficients a_1–a_4 as well as the coefficient of determination R^2 for each fit are provided in table A.1. The coefficient of determination is computed using

$$R^2 \equiv 1 - \frac{SSE}{SST}, \quad SSE = \sum_{i=1}^{n} \left(y_i - \widehat{y_i}\right)^2, \quad SST = \sum_{i=1}^{n} \left(y_i - \overline{y}\right)^2, \quad \overline{y} = \frac{1}{n} \sum_{i=1}^{n} y_i, \tag{A.5}$$

where y_i and $\widehat{y_i}$ refer to the original and fitted data points respectively. SSE is the residual sum of squares and SST is the total sum of squares.

Model	Coefficient	Type	R^2	a_1	a_2	a_3	a_4
	C_1/C_{1_0}	f_1	0.9981	0.2786	-4.7758	0.7213	-0.0334
	C_3/C_{3_0}	f_1	0.9785	0.9712	-1.4877	—	—
GG-I	C_4/C_{4_0}	f_1	0.9917	1.0232	-2.3907	—	—
	C_5/C_{5_0}	f_1	0.9951	0.9978	-2.2155	—	—
	C_P	f_2	0.9334	0.0342	0.2378	0.0981	—
	C_1/C_{1_0}	f_1	0.9981	0.2786	-4.7758	0.7213	-0.0334
	C_3/C_{3_0}	f_1	0.9575	0.9557	-1.5664	—	—
GG-II	C_4/C_{4_0}	f_1	0.9960	1.0111	-2.5253	—	—
	C_5/C_{5_0}	f_1	0.9904	0.9883	-2.3393	—	—
	C_P	f_3	0.9426	0.0105	1.8e-6	-0.3233	0.0452

Table A.1: Least squares curve fits of compressible pressure-strain correlation coefficients.

APPENDIX B

NUMERICAL IMPLEMENTATION FOR INHOMOGENEOUS FLOW COMPUTATIONS

The compressible pressure-strain correlation models GG-I and GG-II are implemented into the ANSYS® FLUENT Release 13.0 software package. Closure model modifications are incorporated into the solver via user defined functions, UDFs. ANSYS® FLUENT [2] solves evolution equations for mean mass (2.3), momentum (2.4), energy (B.1), Reynolds stresses (2.14), and dissipation rate (2.39), shown as used for GG-II. For GG-I there is no C_P term in equation (2.39). The GG-I and GG-II calculations use their respective pressure-strain correlation coefficients that have been calibrated with DNS shown in figure 2.6. The least squares curve fits for the coefficient calibrations can be found in Appendix A. The production, transport, pressure-strain correlation tensors are defined in equations (2.15), (2.20), and (2.35) respectively. In the calculations, air is used as the working fluid, and the molecular viscosity is computed using Sutherland's Law [85], equation (B.4). Additional closure constants applicable to all models are given in equations (B.5) and (B.6).

$$\frac{\partial}{\partial t}(\overline{\rho}E)+\frac{\partial}{\partial x_i}\left[\tilde{u}_i\left(\overline{\rho}E+\overline{p}\right)\right]=\frac{\partial}{\partial x_j}\left[\left(\kappa+\frac{c_p\mu_t}{Pr_t}\right)\frac{\partial\tilde{T}}{\partial x_j}+\tilde{u}_i\left(\tau_{ij}\right)_{\text{eff}}\right],\quad E=\tilde{h}-\frac{\overline{p}}{\overline{\rho}}+\frac{\tilde{u}_i\tilde{u}_i}{2}, \tag{B.1}$$

$$\left(\tau_{ij}\right)_{\text{eff}}=\mu_{\text{eff}}\left(\frac{\partial\tilde{u}_i}{\partial x_j}+\frac{\partial\tilde{u}_j}{\partial x_i}\right)-\frac{2}{3}\mu_{\text{eff}}\frac{\partial\tilde{u}_k}{\partial x_k}\delta_{ij}, \tag{B.2}$$

$$\mu_t=\frac{\overline{\rho}C_\mu k^2}{\varepsilon},\quad \mu_{\text{eff}}=\mu+\mu_t, \tag{B.3}$$

$$\mu=\mu_0\left(\frac{\tilde{T}}{T_0}\right)^{3/2}\left(\frac{T_0+S_0}{\tilde{T}+S_0}\right), \tag{B.4}$$

$$\mu_0 = 1.716\text{e-}5 \text{ [kg/(m-s)]}, \quad T_0 = 273.11 \text{ [K]}, \quad S_0 = 110.56 \text{ [K]}, \tag{B.5}$$

$$C_\mu = 0.09, \quad \sigma_k = 0.82, \quad \sigma_\varepsilon = 1.0, \quad Pr_t = 0.85. \tag{B.6}$$

For comparison, computations are also performed with the LRR [43] and SSG-S [70,83] models. The coefficients of these models are given in table 2.2. The SSG-S model uses the SSG [83] pressure-strain correlation as well as the two main Sarkar compressibility corrections [70,72]: pressure-dilatation shown in equation (2.71), and compressible dissipation given by

$$\varepsilon_c = \alpha_1 \varepsilon M_t^2. \tag{B.7}$$

In the present notation, the SSG-S pressure-strain correlation model is written as

$$\begin{aligned} \Pi_{ij} = &- \left(C_1\overline{\rho}\varepsilon + C_1^*\overline{\rho}P\right) b_{ij} + C_2\overline{\rho}\varepsilon\left(b_{ik}b_{kj} - \tfrac{1}{3}b_{mn}b_{mn}\delta_{ij}\right) + \left[C_3 - C_3^*\left(b_{ij}b_{ij}\right)^{1/2}\right]\overline{\rho}kS_{ij} \\ &+ C_4\overline{\rho}k\left(b_{ik}S_{jk} + b_{jk}S_{ik} - \tfrac{2}{3}b_{mn}S_{mn}\delta_{ij}\right) + C_5\overline{\rho}k\left(b_{ik}W_{jk} + b_{jk}W_{ik}\right) \\ &+ \left(2\alpha_2\overline{\rho}kM_t\frac{\partial\tilde{u}_m}{\partial x_n}b_{mn} + \alpha_3\overline{\rho}\varepsilon M_t^2\right)\tfrac{2}{3}\delta_{ij}. \end{aligned} \tag{B.8}$$

The LRR model has the same form as equation (2.35), except without the C_P term. It must be noted that the LRR model involves no compressibility correction and its results are given only for comparison purposes.